DEVELOPMENT OF LOW POWER LIGHTWEIGHT SINGLE-INPUT MULTIPLE-OUTPUT SYNTHETIC APERTURE RADAR SYSTEM FOR DRONE PLATFORMS

by

Berk Omuz

B.S., Electronics Engineering, Istanbul Technical University, 2010

M.S., Electrical and Electronics Engineering, Boğaziçi University, 2013

Submitted to the Institute for Graduate Studies in
Science and Engineering in partial fulfillment of
the requirements for the degree of
Doctor of Philosophy

Graduate Program in Electrical and Electronics Engineering

Boğaziçi University

2024

ACKNOWLEDGEMENTS

I would like to express my deepest gratitude to my thesis advisor, Professor Ahmet Öncü, for his invaluable guidance, encouragement, and insight throughout this research journey. His expertise and mentorship have been instrumental in shaping the course of this thesis and in broadening my academic perspective.

I extend my heartfelt thanks to my family for their unwavering support, patience, and belief in me during this challenging and rewarding endeavor. I am especially grateful to my wife for her steadfast encouragement, understanding, and love, which have been a source of strength and motivation throughout this process.

I would like to thank all the members of the jury of my thesis for their valuable time, feedback, and contributions, which have greatly enriched this work.

I am also grateful to my project colleagues Ömer Oğuzhan Başpınar, Sefa Erdoğan, Fikriye Öz, Şener Yılmaz, Mustafa Can Macit, and Ali Umut Kaypak for their collaboration, dedication, and support throughout the project. Working alongside such talented and driven individuals has been an invaluable experience.

I would also like to acknowledge the members of MiRaCL, our research laboratory, for their camaraderie and contributions to the successful completion of this work. Being part of such a dynamic and innovative team has been both inspiring and enriching.

Finally, I am deeply appreciative of everyone who has supported and inspired me during this journey, directly or indirectly. This thesis would not have been possible without the collective encouragement of those around me.

ABSTRACT

DEVELOPMENT OF LOW POWER LIGHTWEIGHT SINGLE-INPUT MULTIPLE-OUTPUT SYNTHETIC APERTURE RADAR SYSTEM FOR DRONE PLATFORMS

Unmanned Aerial Vehicles (UAVs) are essential tools across various fields due to their flexibility, mobility, and cost-effectiveness. Integrating advanced radar systems into UAVs, however, poses challenges in power efficiency, payload weight, and real-time processing. This thesis presents a lightweight, low-power Single Input Multiple Output (SIMO) Frequency-Modulated Continuous Wave (FMCW) radar system tailored for UAVs.

Initially, Stepped Frequency Continuous Wave (SFCW) radar was explored for its high resolution and subsurface sensing capabilities, but its limitations in speed and real-time processing led to the adoption of FMCW radar. The proposed system achieves real-time range and velocity measurements critical for UAV operations. Key features include multiple receiver channels for enhanced resolution and GPU-based computation for efficient SAR imaging. Extensive testing validated the radar's 50 cm range resolution and detection of objects up to 100 meters.

The system's superior power efficiency and adaptability address existing UAV radar limitations, enabling applications such as obstacle detection, terrain mapping, and environmental monitoring. Future directions include algorithmic refinements, hardware miniaturization, and sensor integration.

ÖZET

İNSANSIZ HAVA ARAÇLARI İÇİN DÜŞÜK GÜÇLÜ HAFİF TEK GİRİŞLİ ÇOK ÇIKIŞLI SENTETİK AÇIKLIK RADARI SİSTEMİNİN GELİŞTİRİLMESİ

İnsansız Hava Araçları (İHA), esneklikleri, hareket kabiliyetleri ve maliyet etkinlikleri sayesinde birçok alanda önemli hale gelmiştir. Ancak, gelişmiş radar sistemlerinin İHA platformlarına entegrasyonu güç verimliliği, taşıma ağırlığı ve gerçek zamanlı işleme açısından zorluklar yaratmaktadır. Bu tez, İHA'lar için tasarlanmış hafif, düşük güç tüketimli, Tek Giriş Çoklu Çıkış (SIMO) Frekans Modülasyonlu Sürekli Dalga (FMCW) radar sistemini sunmaktadır.

Başlangıçta Adımlı Frekans Sürekli Dalga (SFCW) radar, yüksek çözünürlük ve yüzey altı algılama kabiliyetleriyle incelenmiş, ancak hız ve gerçek zamanlı işleme kısıtlamaları nedeniyle FMCW radara geçilmiştir. Önerilen sistem, İHA operasyonları için kritik olan gerçek zamanlı mesafe ve hız ölçümleri sağlar. Çoklu alıcı kanallar ve GPU tabanlı hesaplama gibi yenilikçi özellikleriyle sistem, 50 cm menzil çözünürlüğü ve 100 metreye kadar algılama kapasitesi sunar.

Sistemin üstün güç verimliliği ve uyarlanabilirliği, mevcut İHA radarlarının sınırlamalarını aşarak engel algılama, arazi haritalama ve çevresel izleme gibi uygulamalara olanak tanımaktadır. Gelecekte algoritma iyileştirmeleri, donanım küçültme ve sensör entegrasyonu hedeflenmektedir.

TABLE OF CONTENTS

ACKNOWLEDGEMENTS . . . iii
ABSTRACT . . . iv
ÖZET . . . v
LIST OF FIGURES . . . ix
LIST OF TABLES . . . xiv
LIST OF SYMBOLS . . . xv
LIST OF ACRONYMS/ABBREVIATIONS . . . xvii
1. INTRODUCTION . . . 1
2. LITERATURE REVIEW . . . 5
2.1. Introduction . . . 5
2.2. SFCW Radar Systems on Drone Platforms . . . 5
2.3. FMCW Radar Systems on Drone Platforms . . . 7
2.4. Comparison between SFCW and FMCW radar . . . 8
2.5. Conclusion . . . 11
3. DESIGN OF SFCW RADAR SYSTEM . . . 13
3.1. Introduction . . . 13
3.2. SFCW Radar Transmitter Hardware Design . . . 15
3.2.1. Introduction . . . 15
3.2.2. Frequency Synthesizer . . . 17
3.2.3. Directional Bridge Coupler . . . 22
3.2.4. Substrate Modelling . . . 32
3.2.5. Conclusion . . . 36
3.3. SFCW Signal Processing Algorithms . . . 37
3.3.1. Introduction . . . 37
3.3.2. Back Projection . . . 38
3.3.3. Delay and Sum Beamforming . . . 39
3.3.4. Conclusion . . . 40
3.4. Implementation of SFCW Algorithms for GB-SAR Systems . . . 41

3.4.1. Introduction . . . 41
3.4.2. Realization of a Linear Rail System to Acquire Ground-Based SAR Data . . . 41
3.4.3. Experimental Verification of In-door Ground Based SAR Using BS-MUSIC Algorithm . . . 45
3.4.4. Conclusion . . . 49
3.5. Structural Health Monitoring and Change Detection Algorithm . . . 50
3.5.1. Introduction . . . 50
3.5.2. Overview of the Interferometric SAR Algorithm . . . 50
3.5.3. Concrete Block Test . . . 55
3.5.4. Building Monitoring . . . 56
3.5.5. Conclusion . . . 57
3.6. Conclusion . . . 58
4. DESIGN OF FMCW RADAR SYSTEM . . . 61
4.1. Introduction . . . 61
4.2. Frequency Modulated Continuous Wave Radar Theory . . . 62
4.3. FMCW SIMO Radar Hardware Design . . . 65
4.3.1. Introduction . . . 65
4.3.2. Power Design . . . 68
4.3.3. Transmitter Design . . . 71
4.3.4. Receiver Design . . . 73
4.3.5. Antenna Design and Selection . . . 75
4.3.6. Conclusion . . . 77
4.4. FMCW Signal Processing Algorithms . . . 77
4.5. Conclusion . . . 80
5. RESULTS AND DISCUSSION . . . 83
5.1. Introduction . . . 83
5.2. Realization . . . 83
5.3. System Integration . . . 87
5.4. Experiments . . . 88
5.5. Comparative Performance Study . . . 91

5.6. Conclusion 94
6. CONCLUSION AND FUTURE WORKS 96
REFERENCES 99
APPENDIX A: COPYRIGHT FOR REUSE OF THE FIGURES 117

LIST OF FIGURES

Figure 2.1. Number of publication about FMCW and SFCW systems across years. 9

Figure 3.1. SFCW Transmitter Block Diagram. 16

Figure 3.2. First variant of frequency synthesizer. 18

Figure 3.3. Output spectrum of first variant with frequency output set to 4 GHz. 18

Figure 3.4. Second variant of frequency synthesizer. 19

Figure 3.5. Third variant of frequency synthesizer. 20

Figure 3.6. Output Spectrum of PLL when TCXO used as reference. 21

Figure 3.7. Output Spectrum of PLL when Signal Generator used as reference. 22

Figure 3.8. Schematic of the proposed bi-directional bridge. 24

Figure 3.9. Simulation results for bi-directional bridge coupler. 25

Figure 3.10. Directional Bridge Design. 26

Figure 3.11. Input Matching. 26

Figure 3.12. Insertion Loss, Coupling, and Isolation. 27

Figure 3.13. Directional Bridge Directivity. 27

Figure 3.14. Dual Bridge Coupler. 28

Figure 3.15. Input Matching of Dual-Bridge Coupler. 28

Figure 3.16. Insertion Loss, Coupling, and Isolation of Dual-Bridge Coupler. . . 29

Figure 3.17. Directivity of Dual-Bridge Coupler. 29

Figure 3.18. Fabricated coupler. 30

Figure 3.19. Coupler measurement results. 30

Figure 3.20. Directivity of fabricated coupler. 30

Figure 3.21. Coupling values obtained via schematic level simulations, measurement, and 3D-EM simulations. 31

Figure 3.22. Insertion Loss values obtained via schematic level simulations, measurement, and 3D-EM simulations. 32

Figure 3.23. Typical two-port vector network analyzer measurement setup. . . 33

Figure 3.24. Fabricated SOLT calibration kit. 34

Figure 3.25. Line modeling schematic in AWR Microwave Office. 35

Figure 3.26. Angle responses of microstrip lines. 35

Figure 3.27. Linear Rail System. 42

Figure 3.28. Overall system diagram. 43

Figure 3.29. The object to be imaged (left), the linear rail (bottom), and the radar system (right). 44

Figure 3.30. Measurement setup in the faculty meeting room, adding complexity through additional reflective surfaces. 45

Figure 3.31. Measurement environment showing the setup at Boğaziçi University, © 2018 IEEE. 47

Figure 3.32. Reconstructed image using the Delay and Sum beamforming algorithm, © 2018 IEEE. 48

Figure 3.33. Image reconstruction with BS-MUSIC algorithm showing isolated reflectors, © 2018 IEEE. 49

Figure 3.34. Top view of the simplified diagram illustrating the GB-SAR system. 51

Figure 3.35. Top view of the virtually pixelized target area as detected by the ground-based SAR. 52

Figure 3.36. Flowchart of the proposed structural health monitoring and change detection algorithm. 53

Figure 3.37. Side view of the GB-SAR system and concrete blocks. 54

Figure 3.38. Images show (a) initial setup with marked blocks, (b) blocks shifted by 5 mm, and SAR images (c) before and (d) after the shift. . . . 55

Figure 3.39. SAR images showing algorithm performance: initial (top), post-displacement (middle), and detected changes (bottom). 56

Figure 3.40. Photographs of the structural monitoring setup: (a) target view, (b) radar system view. 57

Figure 3.41. SAR images showing structural monitoring: initial (top), post-change (middle), and detected changes (bottom). 58

Figure 4.1. FMCW Radar Board Diagram. 67

Figure 4.2. Designed board. 68

Figure 4.3. RedPitaya Extension connector #2. 69

Figure 4.4. Power Section Schematic. 70

Figure 4.5. Transmitter Schematic. 73

Figure 4.6. Receiver Schematic. 74

Figure 4.7. Input Matching. 76

Figure 4.8. Backprojection flowchart. 79

Figure 5.1. FMCW radar board. 84

Figure 5.2. Transmitter output spectrum. 86

Figure 5.3. The system mounted on a drone. 87

Figure 5.4. Range detection. 89

Figure 5.5. KB parking lot measurements compared on top of Google Earth pictures. 91

LIST OF TABLES

Table 3.1. Measured radar displacement values 59

Table 5.1. Board parameters 85

Table 5.2. Prediction error 90

Table 5.3. Comparative Analysis of UAV-Based Radar Systems 93

LIST OF SYMBOLS

c	Speed of light
f	Frequency
f_1	Minimum frequency component at chirp signal
f_2	Maximum frequency component at chirp signal
f_a	Frequency domain of interferometric SAR algorithm
f_k	Frequency point of back projection algorithm
G	Antenna gain
l_b	Radar's position across linear rail platform
$l_{air \rightarrow wall}$	Distance traveled in air to wall
$l_{wall \rightarrow air}$	Distance traveled beyond the wall
l_{wall}	Distance traveled through wall
L_{sys}	Total electromagnetic path loss of the system
N_f	Number of frequency points
N_l	Number of observation points
N_s	Number of submatrices of covariance matrix
P_s	Transmitted power
P_{min}	Minimum detectable power level
R	Range
R_{pi}	Range from (x, y) to (x_{pi}, y_{pi}, z_{pi}) and back
α	Wall attenuation
η	Power efficiency
λ	Wavelength
μ	Micro
Ω	Ohm
ϕ	x-axis rotation
ψ	z-axis rotation
σ	Radar cross section

σ_{mn}	Reflection coefficient of pixel (x,y)
τ	Time constant
τ_{pi}	Propagation delay from (x, y) to (x_{pi}, y_{pi}, z_{pi}) and back
Θ	y-axis rotation

LIST OF ACRONYMS/ABBREVIATIONS

2D	Two Dimensional
3D	Three Dimensional
ADC	Analog to Digital Converter
BS-MUSIC	Beamspace Multiple Signal Classification
CMOS	Complementary Metal-Oxide-Semiconductor
CUDA	Compute Unified Device Architecture
DC	Direct Current
DPP	Difference Pattern Processing
EM	Electromagnetic
FFT	Fast Fourier Transform
FMCW	Frequency Modulated Continuous Wave
FPGA	Field Programmable Gate Array
GB-SAR	Ground-based Synthetic Aperture Radar
GNSS	Global Navigation Satellite System
GPR	Ground-penetrating Radar
GPS	Global Positioning System
GPU	Graphics Processing Unit
IDC	Insulation Displacement Connection
LDO	Low Dropout Regulator
LIDAR	Light Detection and Ranging
LNA	Low Noise Amplifier
MSPS	Mega Samples Per Second
MUSIC	Multiple Signal Classification
NDT	Non-destructive Testing
PFD	Phase-Frequency Detector
PLL	Phase-Locked Loop
PSRR	Power Supply Rejection Ratio
RCS	Radar Cross Section

RF	Radio Frequency
RTK	Real-Time Kinematic
RX	Receiver
SAR	Synthetic Aperture Radar
SIMO	Single Input Multiple Output
SFCW	Stepped Frequency Continuous Wave
SFDR	Spurious Free Dynamic Range
SNR	Signal-to-noise Ratio
SOLT	Short-Open-Load-Thru
SPI	Serial Peripheral Interface
STW	See-Through-Wall
TCXO	Temperature-Compensated Crystal Oscillator
TX	Transmitter
UAV	Unmanned Aerial Vehicle
USB	Universal Serial Bus
VCO	Voltage-Controlled Oscillator
VNA	Vector Network Analyzer
VSWR	Voltage Standing Wave Ratio

1. INTRODUCTION

Unmanned Aerial Vehicles (UAVs) have revolutionized numerous fields over the last decade due to their flexibility, mobility, and cost-effectiveness. UAVs can access remote or otherwise inaccessible areas, making them ideal for tasks that are risky or repetitive for humans. Their ability to be customized for specific applications further enhances their utility [1,2]. Key application areas include logistics, surveillance, object tracking, ground observation and mapping, urban traffic analysis, precision agriculture, remote sensing, search and rescue, non-destructive testing (NDT), civil infrastructure and building inspection, archaeology, glaciology, military applications, radar imaging, and antenna measurements [1–14].

Radar technology is critical for subsurface sensing applications because it can extract surface information remotely without being affected by environmental factors such as illumination and weather conditions. This makes radar particularly useful for UAVs, which often need to gather data over different and possibly difficult-to-access terrains regardless of visibility conditions.

In recent years, there has been a surge in research and development of UAV and drone systems, leading to special interest sections in many journals. Recognizing the growing importance of this field, we initiated our research to develop a novel UAV-based radar system. This thesis will present the design, implementation, and testing of a Frequency Modulated Continuous Wave (FMCW) Single Input Multiple Output (SIMO) radar system specifically tailored for UAV platforms.

UAV systems are equipped with a number of sensors with different capabilities such as cameras, hyperspectral imaging systems, lidars, and radars. Cameras use the visible spectrum of light and can be used to detect and monitor targets, but their operation depends on the presence of light, they cannot detect transparent objects, and they can be easily blocked by obstacles [15]. Hyperspectral cameras differ from

ordinary cameras by using a vast portion of the electromagnetic spectrum, allowing them to collect data of greater detail, but their complexity and cost are greater as well, along with the fact that they still have the disadvantages of ordinary cameras. Lidars use lasers to detect range, offering excellent resolution and range accuracy; however, they are affected by transparency and by weather conditions such as heavy rain and fog due to refraction. Radars use radio waves for range detection instead of light, allowing them to penetrate through obstacles and making them less affected by weather. They are very sensitive to small movements and can create images using synthetic aperture radar (SAR) techniques. SAR images find extensive applications in remote sensing and mapping various surfaces, including topography, oceanography, glaciology, and geology. Applications extend to environmental monitoring in areas like oil spills, flooding, urban growth, coastline detection, and agriculture [16–21]. Despite advances, existing radar systems for UAVs often struggle with high-power demands, limited range resolution, and cumbersome weight, making them less suitable for agile and extended missions.

Initially, this research focused on the development of a stepped frequency continuous wave (SFCW) radar system. SFCW radar is particularly well-suited for applications requiring detailed range profiling due to its ability to sweep through discrete frequency steps, yielding high signal-to-noise ratio (SNR) and precise measurements. Its versatility in ground-penetrating radar (GPR) and subsurface sensing applications demonstrated its potential in UAV-based operations. However, during the prototyping phase, challenges arose related to the system's slower data acquisition rates and the complexity of its signal processing requirements. These issues significantly limited its real-time performance, especially for dynamic UAV applications. Consequently, a transition was made to the FMCW radar, which offered real-time processing capabilities and greater adaptability to UAV environments.

FMCW radar was chosen as the alternative approach due to its continuous frequency modulation, which provides real-time range and velocity measurements crucial for dynamic UAV operations. FMCW systems are widely used in automotive radar and remote sensing due to their relatively simple structure and cost-effectiveness while

providing high-resolution SAR images [22]. They can simultaneously provide range and velocity information, an advantage for UAV applications involving obstacle detection, terrain mapping, and surveillance. FMCW radar systems are also effective for GPR [12–14, 23] and see-through-wall (STW) radar [24, 25] due to the microwave penetration properties. These advantages, combined with FMCW's adaptability to UAV constraints such as weight and power efficiency, position it as an ideal solution for modern aerial radar systems.

The design and implementation of a UAV-based radar system presented several technical challenges, particularly in optimizing power consumption, payload weight, and range resolution. Balancing these constraints while achieving robust performance required innovative solutions. For instance, the use of multiple receiver channels in the FMCW design enhanced spatial resolution and reduced noise, while the incorporation of graphics processing unit (GPU)-based computation enabled near-real-time processing of radar data. Additionally, a modular approach to hardware design ensured compatibility with lightweight UAV platforms, while carefully selected components minimized power demands. These innovations collectively addressed the limitations of existing UAV radar systems, positioning the developed system as a viable solution for short-range, high-accuracy applications.

The successful integration of the radar system with UAV hardware was a pivotal aspect of this research. Combining the radar transceiver, antennas, data acquisition module, and NVIDIA Jetson Xavier platform required meticulous design and testing to ensure compatibility and efficiency. Key considerations included reducing the system's overall weight and ensuring stability during UAV flight. By leveraging the Jetson Xavier's GPU capabilities, the radar system was able to process data-intensive algorithms, such as backprojection, in near-real-time. This integration not only enhanced the system's operational efficiency but also enabled a broader range of applications, including SAR imaging and obstacle detection.

This research achieves a significant milestone in the development of UAV radar technology by introducing a lightweight, low-power FMCW radar system with enhanced spatial resolution and real-time processing capabilities. The system successfully overcomes the limitations of traditional radar designs, offering high-resolution imaging and target detection at ranges of up to 100 meters. These advancements pave the way for practical applications in diverse fields, from environmental monitoring to UAV navigation, while establishing a strong foundation for future improvements and research directions.

The thesis is organized as follows: Chapter 2 reviews current radar technologies and their applications on UAVs, highlighting the advantages and limitations of different approaches. Chapter 3 details the design and development of the SFCW radar system, exploring initial technical challenges. Chapter 4 presents the proposed FMCW radar solution, covering hardware architecture and signal processing strategies. Chapter 5 discusses experimental results, validating the system's performance, and Chapter 6 concludes with recommendations for future research directions.

2. LITERATURE REVIEW

2.1. Introduction

The integration of radar systems on UAV platforms has gained significant traction over the past decade, with notable progress made in developing both SFCW and FMCW radars. This literature review explores these advancements, examining the respective strengths and limitations of SFCW and FMCW radar systems and their applications on UAV platforms. Furthermore, this section identifies gaps in the existing research and outlines how the proposed SIMO FMCW radar system addresses these limitations.

2.2. SFCW Radar Systems on Drone Platforms

SFCW radar systems have been increasingly utilized for various applications on UAV platforms. These systems are known for their high SNR and ability to obtain detailed range profiles, making them suitable for short-range detection and subsurface sensing.

One notable application of SFCW radar is in the detection of small UAVs. A study by Miccinesi et al. explores the use of SFCW radar for detecting small UAVs at short ranges (less than 1–2 km), utilizing Doppler compensation methods to improve range accuracy, especially in real-world field applications [26]. This highlights the adaptability of SFCW radar for dynamic target detection, although its real-time processing capability is limited compared to FMCW systems.

In GPR applications, Šipoš and Gleich developed a lightweight and low-power GPR system based on SFCW radar principles for UAV deployment. This system combines analog and digital processing for enhanced sensitivity, demonstrating the potential of SFCW radar for landmine detection. The system's ability to detect both

metallic and plastic targets, however, comes at the cost of scanning speed, illustrating a limitation in dynamic or time-sensitive applications [27].

Another SFCW radar system, using a dual-channel setup with LabVIEW and NI USRP N210, demonstrated high-resolution subsurface imaging capabilities. This system's accuracy in soil moisture estimation and environmental monitoring highlights the versatility of SFCW radar for subsurface sensing, though the trade-off is often in the speed of data acquisition. These applications show the potential of SFCW radar systems, but their reliance on post-processing limits their real-time performance on UAV platforms [28].

An experimental analysis of an SFCW software-defined radar system utilizing a USRP N210 with a WBX daughterboard, standard gain horn antenna, and waveguide antenna evaluated the system's performance through controlled experiments. The results reveal detailed range profiles and accurate subsurface imaging, underscoring the system's effectiveness for various sensing applications [29].

For long-range applications, researchers introduced a highly sparse array based on combining multiplicative processing and Difference Pattern Processing (DPP) for SFCW radar. This system achieves high resolution with a thinning rate of more than 80% , suitable for long-range applications. The proposed array configuration enhances the radar's resolution and reduces spurious signals, making it suitable for high-precision remote sensing [30].

In surveillance applications, an adaptive SFCW radar system for UAV-based surveillance focuses on real-time target detection and tracking. Utilizing advanced signal processing techniques, the system enhances detection capabilities in cluttered environments. This adaptability ensures robust performance in challenging conditions, making it ideal for security and surveillance operations [31].

Lastly, UAV-mounted SFCW radar has been investigated for soil moisture estimation. Operating over a wide frequency range, the radar system provides detailed soil moisture profiles by analyzing reflected signals. The high accuracy in soil moisture estimation makes it a valuable tool for agricultural and environmental monitoring [32].

Despite these achievements, the slower data acquisition rates and complex signal processing requirements of SFCW systems can hinder their use in fast-changing environments or dynamic applications where real-time performance is necessary. This limitation makes them less suitable for UAV-based applications requiring immediate feedback, leading to increased interest in the development of FMCW radar systems, which are better suited for real-time tasks.

2.3. FMCW Radar Systems on Drone Platforms

FMCW radar systems have emerged as a more practical solution for UAV platforms that require real-time data processing, high mobility, and lower hardware complexity. FMCW radars provide continuous range and velocity measurements, which are critical for UAV operations involving obstacle detection, collision avoidance, and navigation in low-visibility environments [12, 13].

Recent studies have demonstrated how FMCW radar systems, when combined with high-precision positioning systems such as RTK-GPS and GNSS, can achieve high-resolution imaging comparable to more complex radar systems. For instance, work by Fernández et al. [13] demonstrated an FMCW radar integrated with an RTK system, achieving precise UAV-based SAR imaging for surveillance and environmental monitoring tasks. FMCW radar systems require relatively lightweight hardware, making them suitable for deployment on multi-rotor UAVs or mini-UAV platforms where weight is a critical factor.

The ability of FMCW radar to provide continuous real-time data is especially beneficial for UAV-based operations in GPS-denied or cluttered environments, where

other sensors, such as cameras, may fail. This capability has been explored in surveillance and navigation tasks where FMCW radar acts as a supplementary sensor for data fusion [33]. However, FMCW systems may be susceptible to RF interference, which is an area that requires ongoing research to ensure reliability in crowded RF environments [34].

FMCW systems are also used in UAV applications for environmental monitoring, including soil moisture estimation and vegetation mapping. Their real-time processing capabilities allow UAVs to cover large areas quickly, making them ideal for dynamic surveying tasks in agriculture and forestry [14].

2.4. Comparison between SFCW and FMCW radar

SFCW and FMCW radars are two prevalent types of radar systems used in various applications, including UAV platforms. Each has unique advantages and disadvantages, influencing their suitability for different scenarios. This section provides a comparative analysis of these radar systems based on existing literature and highlights the research trends across these technologies.

Research on FMCW and SFCW radar systems has been extensive. A review of academic publications indicates that both technologies have been widely studied and applied across fields. FMCW radar systems, known for their real-time processing capabilities and high-resolution imaging, have seen a significant increase in research and applications, especially in automotive, aerospace, and UAV platforms. In contrast, SFCW radar systems have been prominently utilized in subsurface sensing and GPR applications, leveraging their high SNR and detailed range profiling.

A search in the IEEE Xplore digital library shows that there have been over 2,000 publications related to FMCW radar in the past decade, with a notable increase over time, as shown in Figure 2.1, partly due to advancements in autonomous vehicles and UAV technology. On the other hand, SFCW radar has about 200 publications in the

same period, reflecting its specialized application areas such as geophysical surveys and landmine detection.

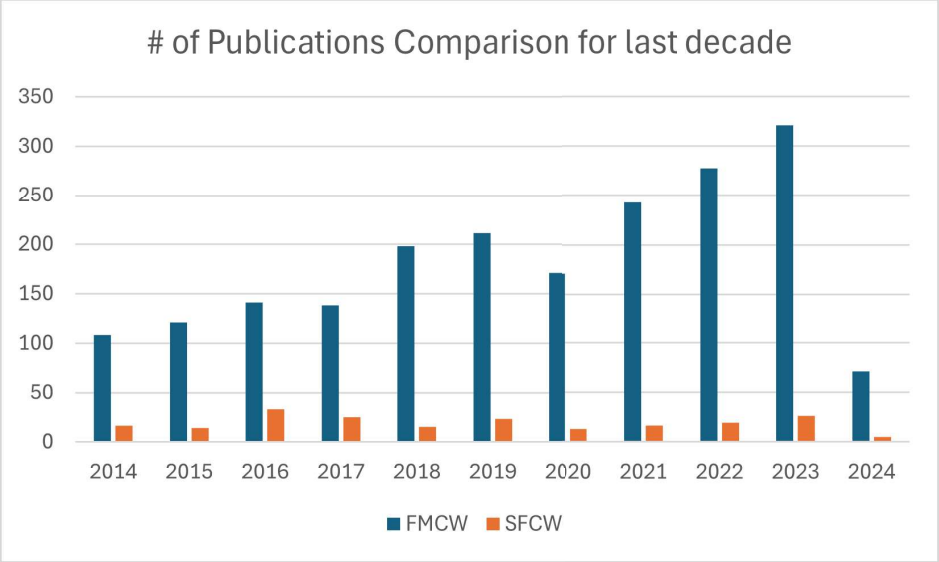


Figure 2.1. Number of publication about FMCW and SFCW systems across years.

FMCW radar systems offer several advantages. They provide near-instantaneous range and velocity information, making them highly suitable for applications requiring real-time data processing, such as automotive radar systems and UAV-based collision avoidance [35]. Due to their continuous frequency modulation, FMCW radars can achieve high range resolution, which is beneficial for detailed imaging and target discrimination. Additionally, FMCW systems often have simpler hardware requirements compared to pulsed radars, reducing system complexity and cost. They can operate continuously, providing uninterrupted data, which is essential for applications like continuous monitoring and surveillance. FMCW radars also handle multipath interference better than pulse radars, enhancing their reliability in cluttered environments.

Despite these advantages, FMCW radars have some drawbacks. They can be more susceptible to interference from other RF sources, which can affect their performance in densely populated RF environments. While they provide high resolution, FMCW radars generally have a shorter range than pulsed radars, limiting their use

in long-distance applications. Additionally, FMCW radars can be affected by phase noise, which might degrade performance in some high-precision applications.

SFCW radar systems also have distinct advantages. They benefit from high SNR due to their stepped frequency approach, which allows for better signal processing and target detection in noisy environments. By stepping through a range of frequencies, SFCW radars can produce highly detailed range profiles, making them ideal for subsurface sensing and GPR applications. SFCW radars allow for flexible frequency selection, which can be tailored to specific applications and environments to optimize performance. Typically, SFCW radars require less power than FMCW systems, making them suitable for battery-operated devices, such as UAVs, where power consumption is critical. Furthermore, SFCW radars can achieve better range resolution at lower frequencies, useful for applications like underground imaging.

One limitation of SFCW radar systems is the increased complexity of signal processing due to the need for detailed post-processing of stepped frequency data, which requires more computational resources. The time taken to sweep through the frequencies can reduce temporal resolution, making SFCW radars less suitable for real-time applications. Additionally, moving targets can create artifacts in the range profiles, complicating data interpretation in dynamic environments. The sequential nature of frequency stepping also results in slower data acquisition rates, which can be a drawback in rapidly changing environments.

FMCW radar systems are widely preferred in applications that demand real-time processing and high-resolution imaging, such as automotive safety systems, UAV collision avoidance, and short-range surveillance. Their continuous operation and simplicity in implementation make them cost-effective and efficient for many practical applications. In contrast, SFCW radar systems excel in scenarios where high SNR and detailed range profiles are paramount. They are particularly effective in subsurface sensing applications, such as GPR, where the ability to detect and profile buried ob-

jects is critical. The flexibility in frequency selection and lower power requirements further enhance their suitability for specialized applications.

The choice between FMCW and SFCW radar systems depends largely on the specific requirements of the application. FMCW radars offer advantages in real-time processing and high-resolution imaging, making them ideal for dynamic environments and continuous monitoring. Conversely, SFCW radars provide superior SNR and detailed range profiling, which are essential for subsurface and detailed static sensing applications. Understanding these trade-offs is crucial for selecting the appropriate radar technology for specific UAV applications.

2.5. Conclusion

The problem addressed in this study is the lack of radar systems specifically designed for small consumer drones. The purpose of the study is to design a low-power, lightweight SIMO SAR system for drone platforms. This study underscores the significance of radar systems in UAV applications, highlighting their importance for various tasks such as remote sensing, surveillance, and obstacle detection.

The contribution of this thesis is the development of a novel FMCW SIMO radar system that strikes a balance between power consumption, weight, and RF transmit power, making it suitable for UAV platforms. Unlike previous work, the proposed system leverages multiple receiving channels, which enhances accuracy and spatial resolution in imaging and target tracking. This multi-channel approach helps mitigate noise, interference, and multipath effects, thereby reducing ambiguity in radar data [36–39].

The design goal was to create a compact and lightweight solution for drone-based remote sensing applications. The radar system is implemented on a 94mm x 83mm board, weighing less than 100 grams, and includes a battery-powered transceiver module with one transmitter (Tx) and two receiver (Rx) channels. To enhance processing

capability for SAR applications, GPU-based computation is utilized with a Jetson Xavier development module to obtain range profiles. Additionally, algorithms have been developed to generate SAR images in near-real-time while the UAV is in motion. This capability will enable UAVs to extract additional environmental features and use this information to improve navigation and operational efficiency.

3. DESIGN OF SFCW RADAR SYSTEM

3.1. Introduction

This chapter delves into the development of a SFCW radar system, examining the technical intricacies involved in creating a versatile and high-resolution radar suitable for UAV and ground-based applications. SFCW radar, with its capability of generating detailed range and spatial information, provides a promising solution for applications such as structural monitoring, environmental sensing, and target detection, which require high precision and adaptability.

SFCW radar systems transmit electromagnetic waves in a series of discrete frequency steps rather than a continuous waveform. This stepped frequency approach enhances resolution and accuracy, making it possible to achieve precise target localization and material characterization. However, realizing the full potential of SFCW radar requires careful design and calibration, especially for applications where power efficiency, portability, and operational flexibility are critical. This chapter is structured to address the major design aspects and challenges encountered in the development of an SFCW radar system, covering transmitter hardware, directional couplers, substrate modeling, and advanced signal processing algorithms.

The chapter begins with the design and development of the SFCW radar transmitter hardware, which includes a frequency synthesizer as the core component. The transmitter's design utilizes the ADF4355-3 frequency synthesizer, chosen for its wide frequency range and fractional-N phase-locked loop (PLL) capability. The transmitter section describes the integration of voltage-controlled oscillators (VCOs), PLLs, and digital step attenuators to achieve a stable and flexible frequency output. Special emphasis is placed on minimizing power consumption and ensuring phase coherence across frequency steps, both crucial for portable UAV-based applications.

Following the transmitter design, the chapter introduces the directional bridge coupler, a critical element in measuring S-parameters by differentiating between incident and reflected signals. Building on the work by Drobotun and Mikheev, this section discusses the adaptation of directional bridges into a bi-directional bridge suitable for UAV platforms, balancing performance with reduced weight. The coupler's design, fabrication, and optimization process are detailed, with simulation results provided to demonstrate the design's reliability and effectiveness.

Substrate modeling, an essential part of ensuring accurate signal propagation, is the focus of the next section. The high-performance laminates used in the project require precise modeling of the substrate to compensate for variations in dielectric properties. Through detailed calibration and differential phase length methods, this section explores the challenges of obtaining reliable substrate parameters for consistent signal transmission, a process critical to achieving high accuracy in radar measurements.

The chapter then turns to the signal processing algorithms essential for generating high-resolution radar images. Two primary imaging algorithms, which are backprojection, delay and sum beamforming, are examined in detail. Each algorithm's mathematical foundation and implementation steps are discussed, highlighting their suitability for specific applications within SFCW radar systems. The backprojection algorithm is used to construct images by correlating spatial positions with range profiles, while the delay and sum method provides enhanced focus by adjusting for propagation delays. The frequency-wavenumber imaging technique, optimized for faster computation, offers an efficient alternative for producing radar images in real-time or near-real-time applications.

Finally, the chapter presents the practical realization of the SFCW radar system in a Ground-based Synthetic Aperture Radar (GB-SAR) application. Here, a linear rail system, complete with a Vector Network Analyzer (VNA), antenna, servo motor, and controller, is used to capture radar data from stationary and dynamic targets. The experimental setup, which includes data acquisition at multiple frequencies and spatial

positions, demonstrates the system's ability to perform high-resolution SAR imaging in real-world environments. Additionally, the application of advanced algorithms such as the Beamspace multiple signal classification (BS-MUSIC) algorithm for improved target localization illustrates the system's potential for high-resolution imaging in cluttered environments.

Through this exploration of transmitter design, coupler optimization, substrate modeling, and advanced signal processing, this chapter provides a comprehensive overview of the technical innovations and challenges involved in developing an SFCW radar system. Each subsection builds upon the last, contributing to an integrated radar solution designed for precision, adaptability, and efficiency which are essential attributes for UAV-based and ground-based radar applications.

3.2. SFCW Radar Transmitter Hardware Design

3.2.1. Introduction

The SFCW Radar Transmitter Hardware is crafted with a modular approach, dividing the system into a frequency synthesizer and a power-level regulation circuit. This design strategy simplifies prototyping and enables independent testing and refinement of each component. The frequency synthesizer serves as the primary signal source, generating a continuous wave signal across a range of frequencies, while the secondary circuit adjusts the signal power using a digital step-attenuator, gain block, and power detector as shown in Figure 3.1. This modular arrangement allows flexibility in tuning the radar's output to specific performance requirements.

The frequency synthesizer, a critical component in the radar's operation, leverages the ADF4355-3 for its extensive frequency range and fractional-N PLL capability, enabling both low- and high-frequency operations between 51.5625 MHz and 6600 MHz. This broad range and high frequency resolution provide the flexibility needed for a wide range of applications, including GPR and subsurface sensing, where

deeper penetration is achieved at lower frequencies. The synthesizer's integration with a VCO, phase-frequency detector (PFD), and programmable frequency dividers further enhances signal integrity while simplifying the overall design.

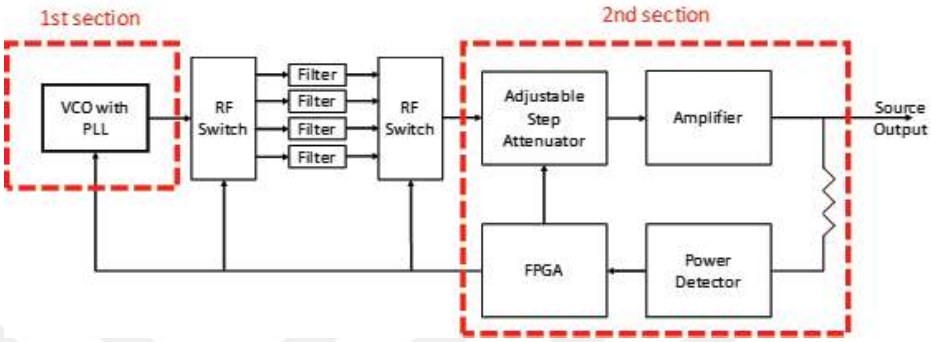


Figure 3.1. SFCW Transmitter Block Diagram.

To support accurate signal separation and measurement, the Directional Bridge Coupler is implemented for isolating incident and reflected waves, ensuring consistent coupling over a wide frequency range. Based on the design by Drobotun and Mikheev, this component has undergone several iterations to optimize coupling values and minimize insertion loss. By transforming the original design into a bi-directional bridge, the transmitter achieves improved performance and compactness which is ideal for UAV applications where weight and space are critical. The resulting bi-directional coupler enhances both forward and backward measurements, meeting the high precision requirements for SFCW radar.

The final element, Substrate Modeling, plays a crucial role in sustaining reliable signal propagation by addressing the transmission characteristics of the PCB material. Through extensive modeling and testing, the substrate was refined to reduce phase distortion and insertion loss, supporting performance across the intended frequency range. Accurate modeling of the substrate was essential to maintain signal quality at GHz frequencies, particularly when designing for outdoor UAV applications where environmental conditions can impact dielectric properties. This modeling process included

the use of specialized high-frequency laminates and meticulous parameter calibration to ensure minimal signal degradation.

Each of these hardware components, the frequency synthesizer, directional bridge coupler, and substrate, has been developed through an iterative process, with refinements at every stage aimed at achieving a balance of flexibility, precision, and durability. This chapter provides an in-depth examination of each subsystem's design and the technical decisions driving its optimization, illustrating how these foundational components support the overall performance of the SFCW Radar Transmitter Hardware.

3.2.2. Frequency Synthesizer

The frequency synthesizer is a critical component in every microwave radar system. Over the last decade, voltage-controlled oscillators with integrated PLLs have been developed, covering several GHz bandwidths. In this project, the Analog Devices ADF4355-3 was chosen for its versatility and performance, particularly its ability to generate frequencies from 51.5625 MHz to 6600 MHz.

During the semester, several different variants of frequency synthesizers were designed, produced, and measured. The first variant, which was successfully implemented, was programmable with both Arduino and FPGA due to its simple 3-wire communication. The reference signal was applied from headers on the left-hand side, utilizing the FPGA's clock output. The output of the PLL was further amplified using the ADL5542 gain block. The first frequency synthesizer board can be seen in Figure 3.2.

While the first variant was successful, the output spectrum exhibited some undesired spurs, as shown in Figure 3.3. The reference frequency applied from a signal generator had a similar spectrum, centered at 10 MHz and these spurs were shifted to higher frequencies by the PLL.

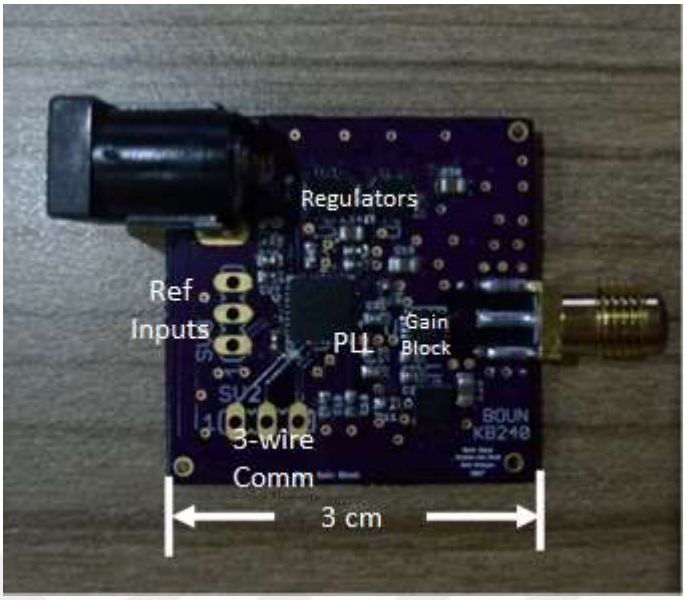


Figure 3.2. First variant of frequency synthesizer.

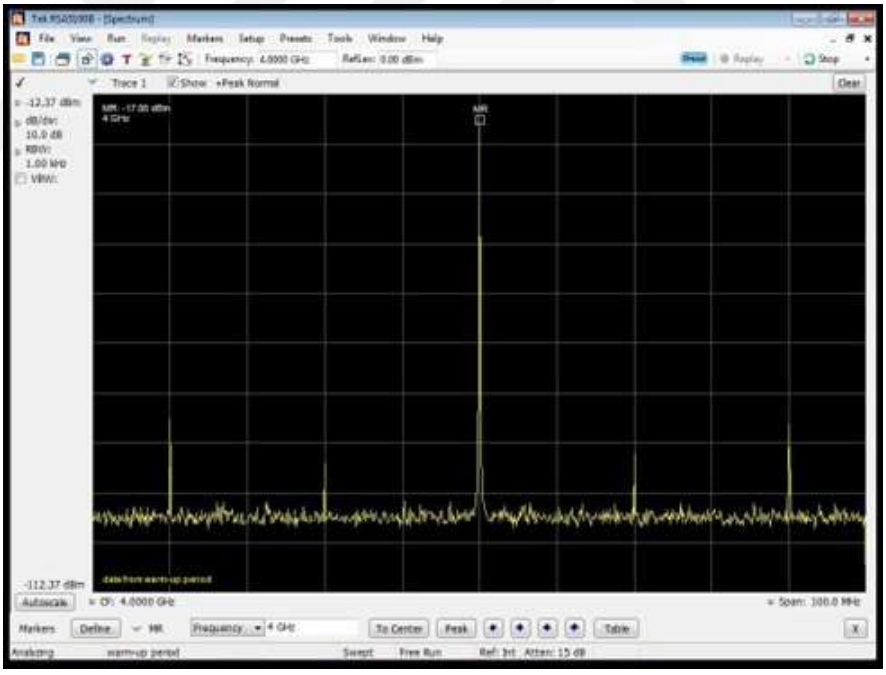


Figure 3.3. Output spectrum of first variant with frequency output set to 4 GHz.

For the second variant, the board's complexity was increased to further progress and eliminate these spurs. Adding a temperature-compensated crystal oscillator (TCXO) was a key improvement due to its precision and reduced temperature sensitivity. Since the project involved a drone platform that operates outdoors, minimizing temperature-induced frequency variations was crucial. Additionally, the ADL5542 gain block was

removed to accommodate a digital step attenuator between the PLL output and the gain block. Designing a separate board for power level feedback was logical, as these could be easily connected via an SMA cable, saving time and costs.

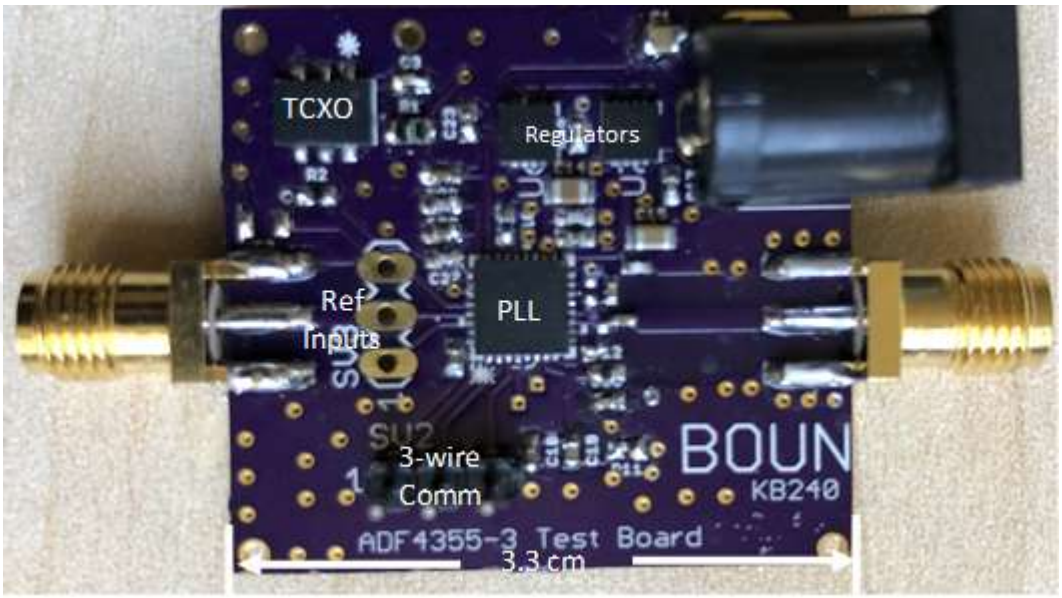


Figure 3.4. Second variant of frequency synthesizer.

In case of a TCXO failure or to explore better reference frequency generation methods with FPGA, reference inputs remained available from headers and an SMA input on the left-hand side board. Disabling the TCXO was straightforward, requiring desoldering the R1 resistor. To use a single-ended reference input, C2 had to be soldered to eliminate noise on the negative frequency reference input pin. The RF coils at the output driver, which were omitted in the first variant to reduce cost, were added as suggested in the ADF4355-3 datasheet.

Unfortunately, during the initial testing stages, a misrouted level shifter on the 3-wire communication line caused 5V to be applied to the PLL, damaging its register bank. As a result, the second variant could not be programmed, and measurement results were unavailable.

For the next variant, minor changes to the stencil were necessary as exposed pads caused issues during the reflow process. Reducing the size of solder paste gaps might

help. Moreover, soldering and desoldering the 0 Ω resistor to enable/disable the TCXO was primitive and was replaced by a 3-pin jumper. Additional information about the jumper position and TCXO ON/OFF status was added to the silk layer to make the board more user-friendly, as seen in Figure 3.5.

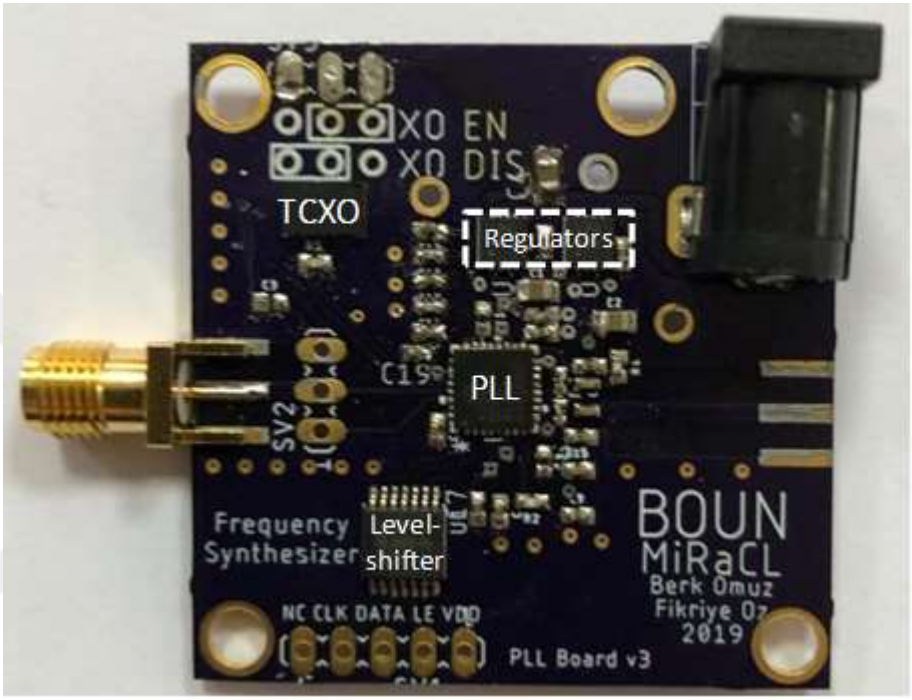


Figure 3.5. Third variant of frequency synthesizer.

In this third variant, an added level-shifter IC prevented damage to the PLL's register bank, which uses 3.3V logic. SPI communication with the PLL was done using commercially available development boards, some of which only provided 5V output. The TCXO's enable/disable function was managed using a simple jumper, providing flexibility for further experiments.

The PLL output was set to 5 GHz, with the power level adjusted to -1 dBm to inspect the output spectrum. Given that one of the differential outputs of the PLL was grounded, the expected output level was 3 dB lower.

The output was measured to be -6 dBm, indicating a 2 dB loss from the microstrip line and the cable used to connect the PLL output to the spectrum analyzer. The

negative bleed charge pump current of the PLL was then tuned to reduce the spurs further, achieving an spurious free dynamic range (SFDR) level of 55 dB. The system was then tested again by disabling the TCXO and applying 25 MHz from a signal generator to determine if the spurs were caused by the reference signal itself.

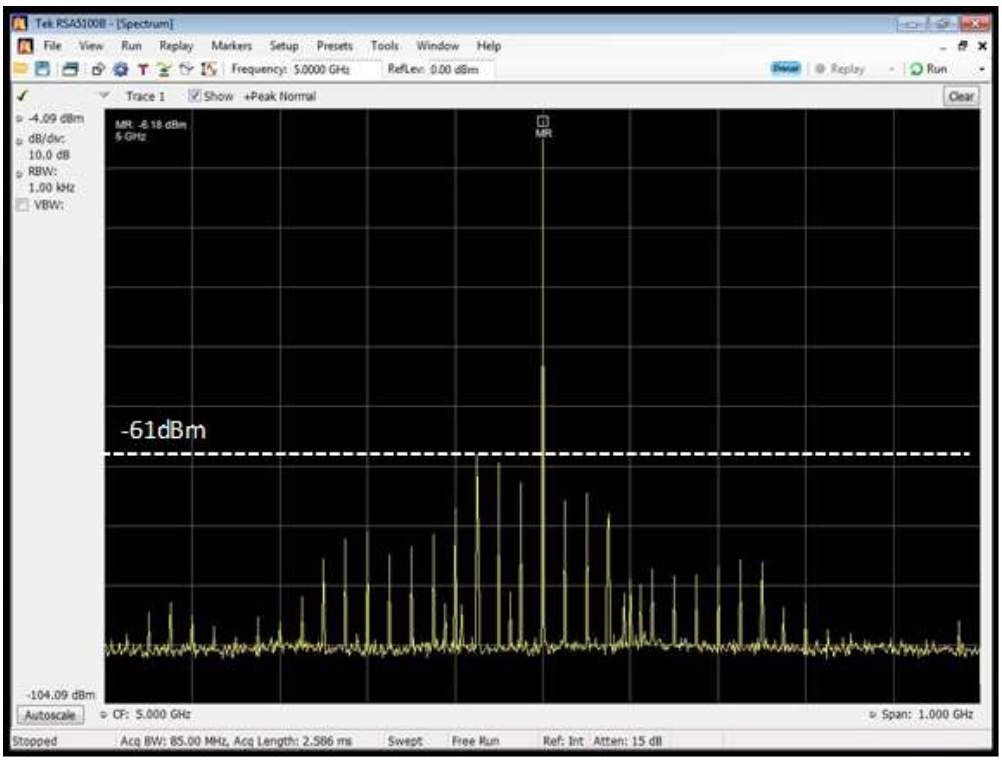


Figure 3.6. Output Spectrum of PLL when TCXO used as reference.

The SFDR of the PLL did not change, although the output spectrum was less spurious when the TCXO was used as the reference signal, indicating the TCXO's effectiveness.

An output balun was required to convert the differential signal to single-ended to eliminate odd-order harmonics and increase power levels. Even-order harmonics generated by the PLL needed to be filtered out using switches and RF filters, enhancing performance. As the local oscillator on the receiver side was also based on this frequency synthesizer design, routing complexity increased, necessitating a 4-layer process. Using manufacturers such as OSHPark, which offer FR408 laminate with an almost constant dielectric constant up to 10 GHz, met the project's needs. The process offered a 4-layer

stack-up with a 6.7 mil dielectric layer between the top two copper layers, resulting in relatively thin transmission lines around 0.345 mm. These lines provided excellent interfaces with QFN32 packages, commonly used for MMICs with pin widths of 0.3 mm. The clearance offered by OSHPark allowed two transmission lines in parallel to side-by-side pins; otherwise, the process wouldn't allow wiring double balanced mixer input-output. A 4-layer process facilitated the distribution of power lines and digital signals on the board, along with RF paths.

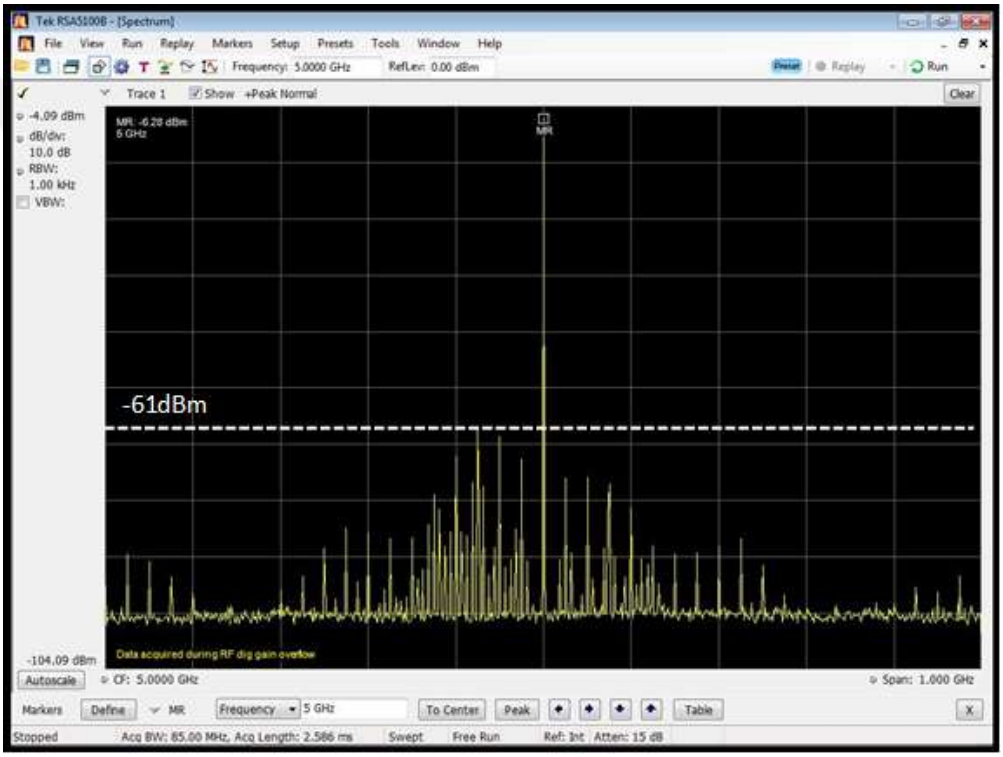


Figure 3.7. Output Spectrum of PLL when Signal Generator used as reference.

3.2.3. Directional Bridge Coupler

A directional coupler is a crucial component of any s-parameter measurement system, as it is required to distinguish between incident and reflected waves. Although several methods, including microstrip and waveguide-based directional coupler designs, are available in textbooks, both suffer from frequency dependence. While it is possible to increase the bandwidth of these designs, maintaining a constant coupling value over a wide range of frequencies is challenging. Therefore, directional bridges are more

commonly used in vector network analyzers due to their ability to operate from several MHz to the GHz range while maintaining an almost constant coupling value across their working frequency.

The most recent advancements in wideband directional bridges are presented in the work by Drobotun and Mikheev [40]. Their research offers a detailed analysis and design of a directional bridge operating in the 300 kHz to 13.5 GHz range. Although their paper contains some inconsistencies in port numbering and lacks clarity in certain descriptions, it was instrumental in understanding the fundamental principles and practical aspects of directional bridge design. Their schematic and 3D-EM model provided valuable insights into the design process, and interested readers may consult their publication for additional details on the original design and its implementation. By building upon their work, we were able to modify and optimize the directional bridge to better suit our specific requirements, leading to improved performance and reliability in our s-parameter measurement system.

Based on the work by Drobotun and Mikheev, we were able to convert their directional bridge circuitry into a bi-directional bridge by adding another resistive bridge to the other port. This modification allowed us to capture a portion of both incident and reflected waves, effectively doubling the measurement capability. Additionally, this bi-directional design significantly reduced the overall weight of the system, which is critical for drone applications. The added resistive bridge ensured that the device could maintain its performance while operating efficiently in a more compact form factor. The schematic of the proposed bi-directional bridge, as shown in Figure 3.8, illustrates the implementation of these changes. By leveraging this design, we optimized the system to better meet the stringent weight and performance requirements of our application.

By converting the directional bridge into a conventional four-port directional coupler, it was also possible to use port names input, thru, isolation, and coupled,

respectively. By studying the circuit, the s-parameters were derived as,

$$S_{12} = S_{21} = \frac{Z_2}{Z_0 + Z_2},\ S_{41} = S_{32} = \frac{Z_2}{Z_1 + Z_2}\ where\ {Z_2}^2 = Z_1 Z_0. \tag{3.1}$$

While satisfying the bridge condition, it was also necessary that all ports be matched to 50 Ω. Z2 is equal to 50 Ω, whereas Z1 and Z0 are 270 Ω and 9.25 Ω, respectively. In the studied work, Z0 was selected slightly higher due to the influence of the balancing transformer, which is expected to be due to the tolerances of resistor values. In order to use high-precision components, the E12 series was chosen. Z2 was realized with two 100 Ω resistors in parallel, and 270 Ω is already available in the E12 series. Z0 was selected to be 9.1 Ω as it is the closest value to 9.25 Ω. When these values were plugged into the equations, they resulted in 16 dB coupling and 1.6 dB insertion loss.

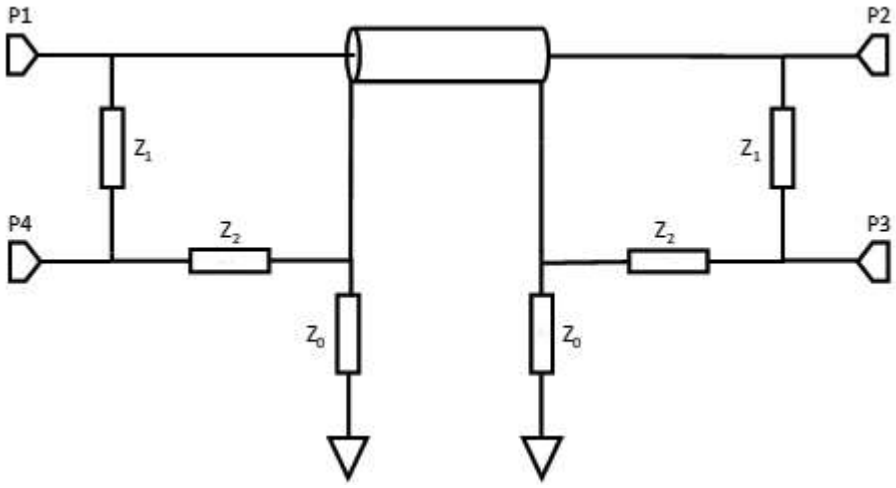


Figure 3.8. Schematic of the proposed bi-directional bridge.

Subsequently, the circuit was analyzed in AWR Microwave Office to verify its behavior. The circuit showed almost constant performance over a wide frequency range, as shown in Figure 3.9. This consistency is mostly due to ignoring the parasitic capacitors and added transmission line effects between resistors. Moreover, using the FR4 substrate would reduce the operating frequency to several GHz because of its relative dielectric constant variation and increased losses. As a result, it was necessary to use high-performance laminates for such circuitry.

The bridge coupler was studied further until its performance was satisfactory for directional operation. By optimizing the bridge, the overall dimensions of the system were reduced, which in turn decreased the number of meshes and thus the simulation time. Several optimization parameters were added, and the entire structure was built using parametric cells to simplify the redesign process. Multiple parametric sweeps were conducted to find the optimal solutions for the widths and lengths of the cutouts and the ground plate of port 3. The finalized design, along with its s-parameter results and directivity, is shown in Figures 3.10 and 3.13.

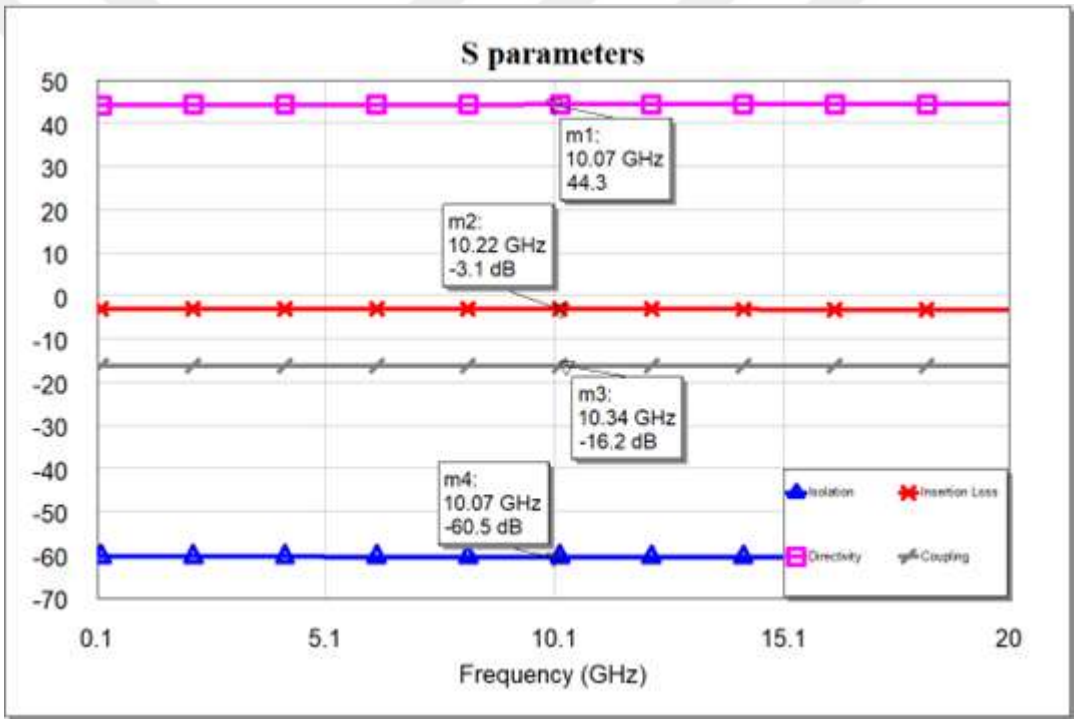


Figure 3.9. Simulation results for bi-directional bridge coupler.

The coupler was well-matched, and the directivity was above 16 dB up to 6 GHz, which is the maximum frequency of the proposed system. The coupling value varied between 16 dB ±2 dB over the entire frequency span, as shown in Figures 3.11 and 3.12. This level of performance indicates that the coupler is highly effective in distinguishing between incident and reflected waves across a wide frequency range. The stability of the coupling value ensures reliable measurements, which is crucial for precise s-parameter analysis. Furthermore, the high directivity minimizes the interference from reflected signals, thereby enhancing the accuracy of the measurements. The

optimization of the coupler's design, including careful selection of component values and geometries, contributed significantly to achieving these performance metrics. This makes the coupler a robust component for advanced measurement systems operating in the GHz range.

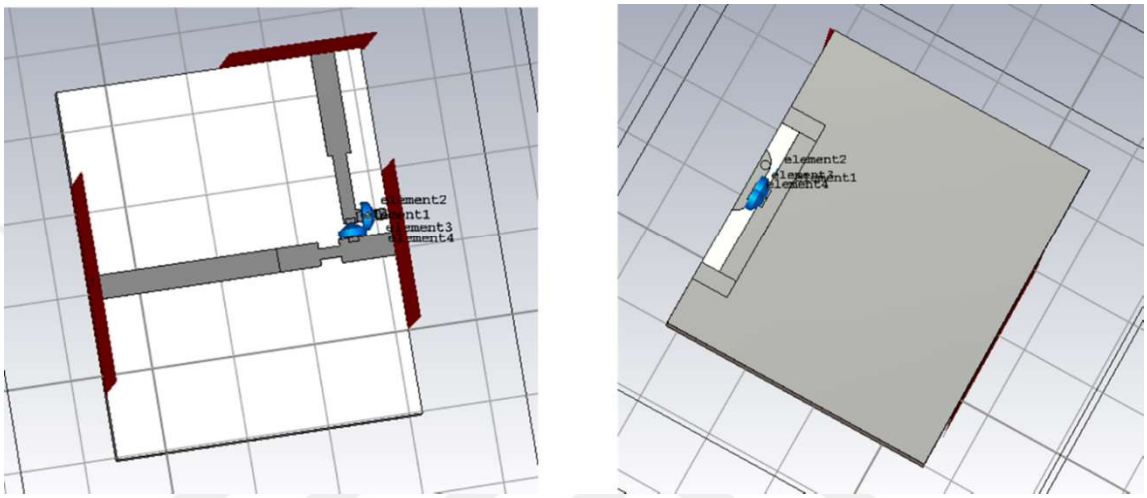


Figure 3.10. Directional Bridge Design.

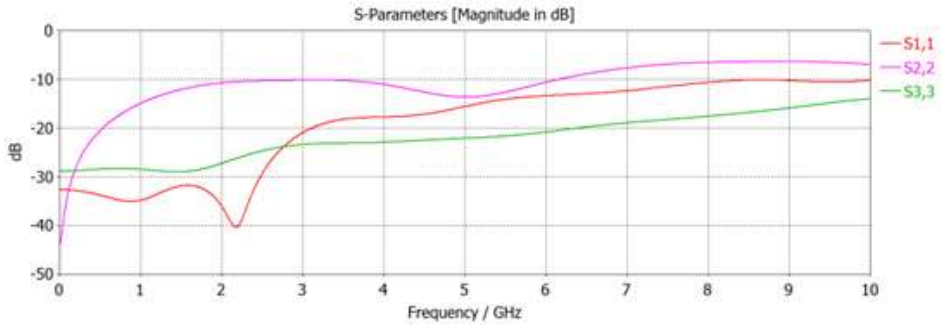


Figure 3.11. Input Matching.

In order to obtain a dual-bridge coupler, the bridge itself was copied and mirrored while adding a transmission line between the bridge sections. This approach maintained the fully parametric nature of the structure, as it replicated the original bridge design. The length of the transmission line became another crucial design parameter that needed careful optimization. Originally, the ground plane of the output port of the directional bridge was minimal, which was not suitable for a board-edge RF connector. However, by implementing a dual-bridge configuration, it became possible to use SMA

connectors on all four ports, enhancing connectivity and integration capabilities. This modification is illustrated in Figure 3.14, which shows the dual-bridge coupler design.

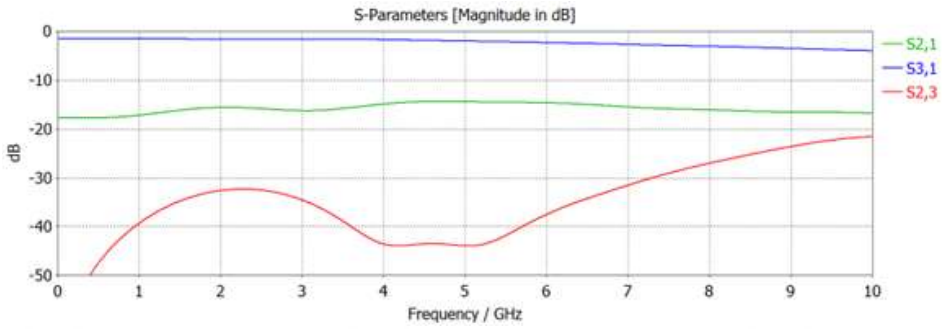


Figure 3.12. Insertion Loss, Coupling, and Isolation.

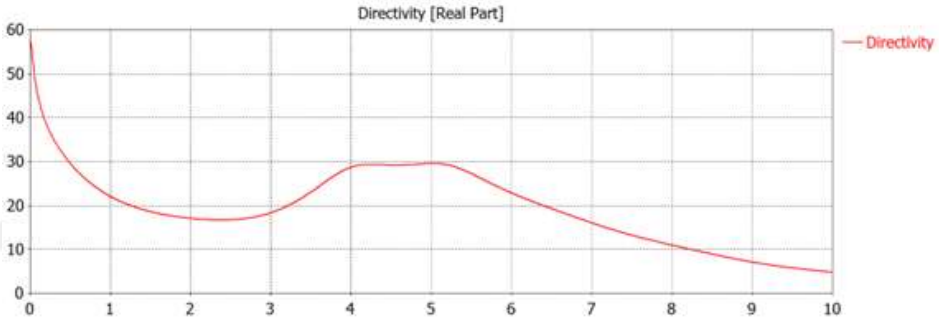


Figure 3.13. Directional Bridge Directivity.

The use of SMA connectors improved the mechanical stability and ease of connection, making the system more robust for practical applications. Furthermore, the dual-bridge design allowed for better impedance matching and reduced signal loss, contributing to the overall performance and reliability of the measurement system.

As can be seen from the graph, the inputs were well-matched up to 6 GHz, similar to the directional bridge coupler. However, isolation and directivity were highly dependent on the transmission line length. The resonant behaviors occurring in the isolation s-parameters prevented the directivity from reaching low levels, making it difficult to achieve optimal performance. The required length of the transmission line tended to be impractical, reaching up to 80 cm in some cases. Considering that the project is intended to be mounted on a drone platform, it is impractical to incorporate a meter-long coupler into the system. This limitation is illustrated in Figures 3.16

and 3.17, which show the insertion loss, coupling, isolation, and directivity of the dual-bridge coupler. The impracticality of such a long transmission line highlights the need for further optimization and alternative design approaches to achieve the desired performance within the constraints of the drone platform.

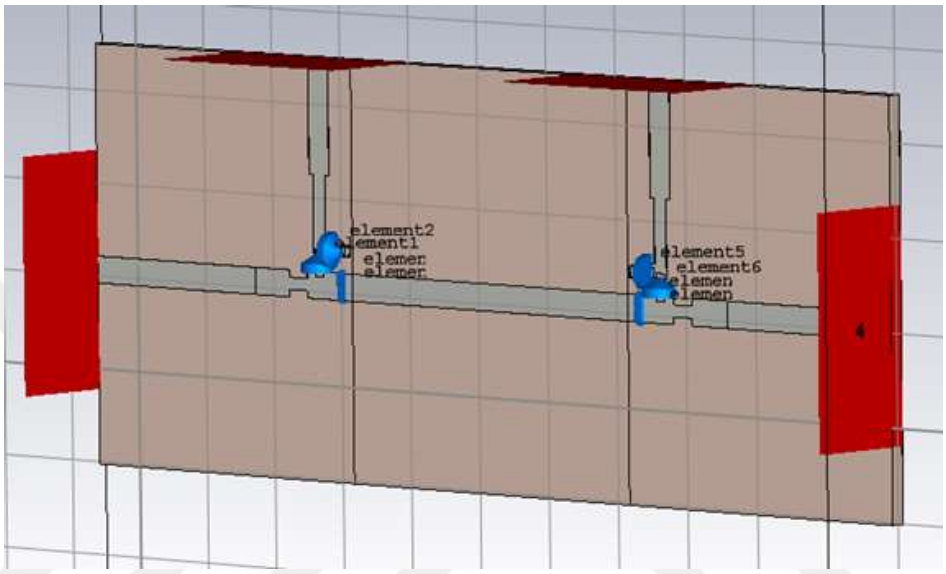


Figure 3.14. Dual Bridge Coupler.

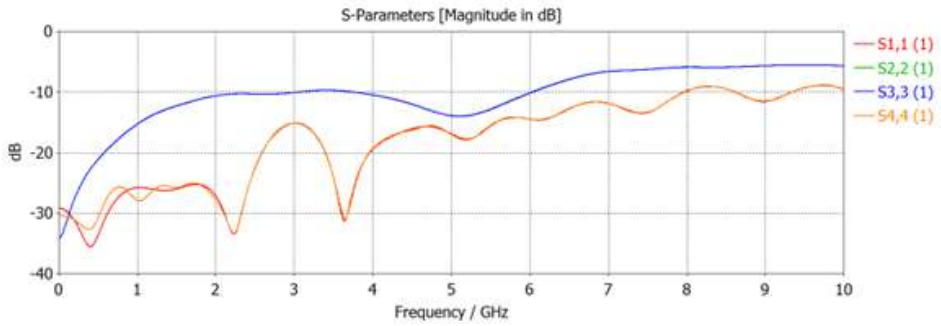


Figure 3.15. Input Matching of Dual-Bridge Coupler.

Given these constraints, several commercially available directional bridges were studied, some of which exhibited similar resonant-like behavior with their directivity. This comparison provided valuable insights into the performance characteristics of various designs. The reason that our coupler needed to be much longer might be due to the lower effective permeability of microstrip transmission lines compared to coaxial lines, as noted in the work by Drobotun and Mikheev [40]. This difference in effective permeability can significantly impact the impedance matching and overall performance

of the coupler. By understanding these limitations, we were able to identify potential areas for further optimization and improvement in our design.

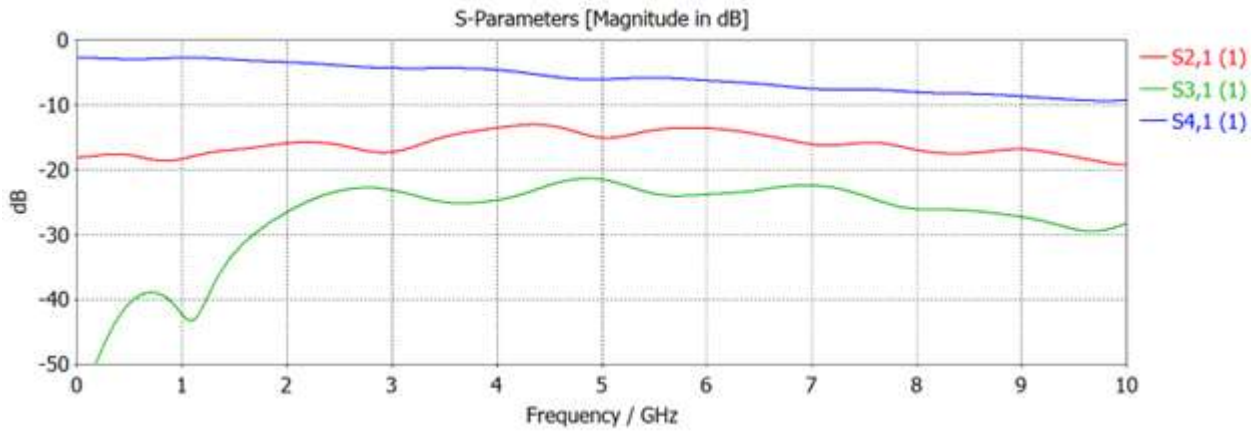


Figure 3.16. Insertion Loss, Coupling, and Isolation of Dual-Bridge Coupler.

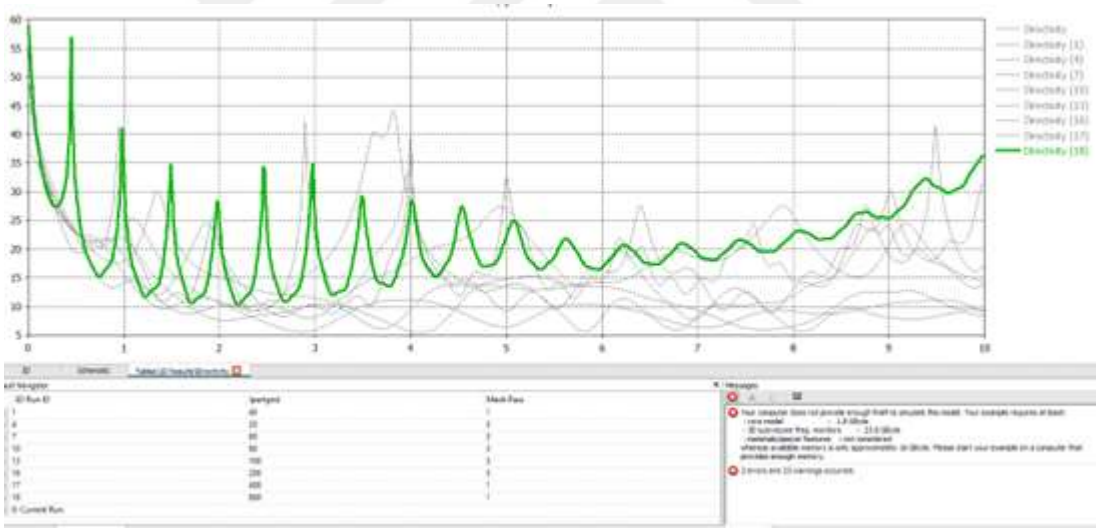


Figure 3.17. Directivity of Dual-Bridge Coupler.

To begin with, schematic-level designs were created to analyze the characteristic impedance of each line, which provided the following insights: The line between the coupling port and port 1 should have a high impedance of around 320 Ω, and its electrical length should match the line connecting Z2 to Z0. These lines are indicated in the fabricated coupler as l1 and l2, as shown in Figure 3.18. This analysis was crucial in ensuring proper impedance matching and minimizing signal reflections within the coupler. By carefully designing these lines, we aimed to achieve optimal perfor-

mance across the intended frequency range, thereby enhancing the overall reliability and accuracy of the measurement system.

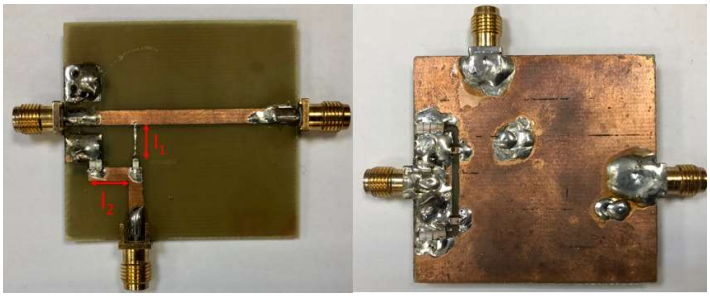


Figure 3.18. Fabricated coupler.

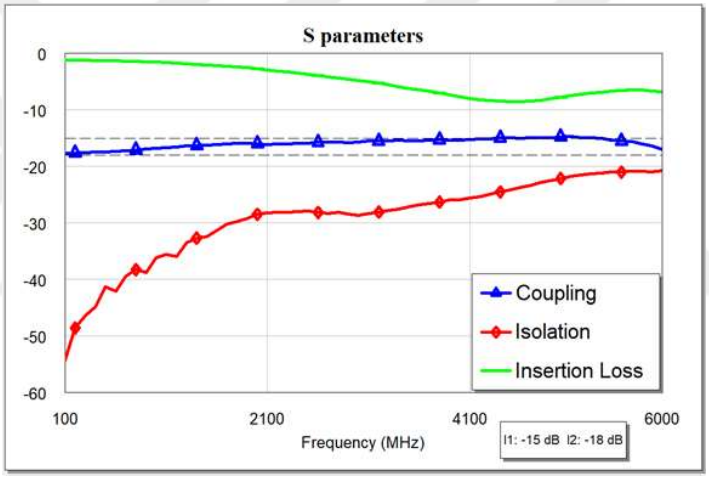


Figure 3.19. Coupler measurement results.

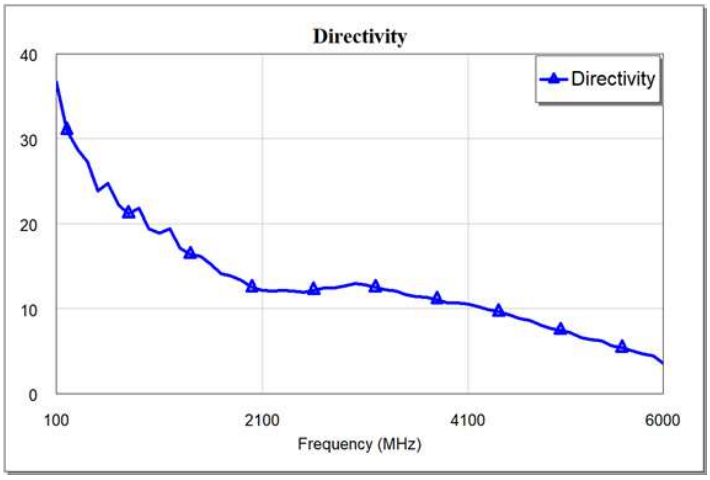


Figure 3.20. Directivity of fabricated coupler.

Another critical point in the design is that the termination of Z0 must be made with a low impedance line. However, using a single resistor at the end of a low impedance line is impractical, as the line would be much wider than the resistor. Therefore, ten parallel 75 Ω resistors were used to replace a single 7.5 Ω resistor. Despite these efforts, the performance of the fabricated coupler degraded rapidly over 2 GHz. This degradation indicates that the design needs further optimization to maintain performance at higher frequencies. The measured s-parameters and calculated directivity, as shown in Figures 3.21 and 3.22, highlight these performance issues. These results underline the necessity for further refinement to achieve stable and reliable performance across the desired frequency range.

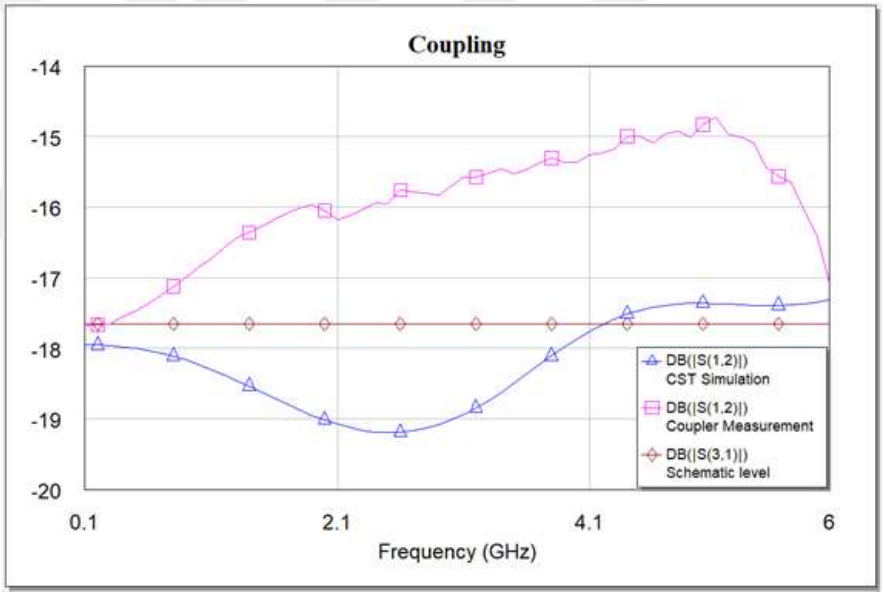


Figure 3.21. Coupling values obtained via schematic level simulations, measurement, and 3D-EM simulations.

Despite the differences observed at low frequencies, the 3D-EM simulations show a good correlation with the measured results for input matching and insertion loss, as illustrated in Figure 3.22. If the issues at lower frequencies are resolved, it is likely that the outputs will be even more closely aligned. The discrepancies are probably caused by the transmission lines with different characteristic impedances and the connections between elements, which introduce additional transmission line effects and phase shifts. As the frequency increases, these effects become more pronounced, leading to degraded

performance. Therefore, it is essential to minimize all interconnects to enhance the operating bandwidth and achieve more reliable results.

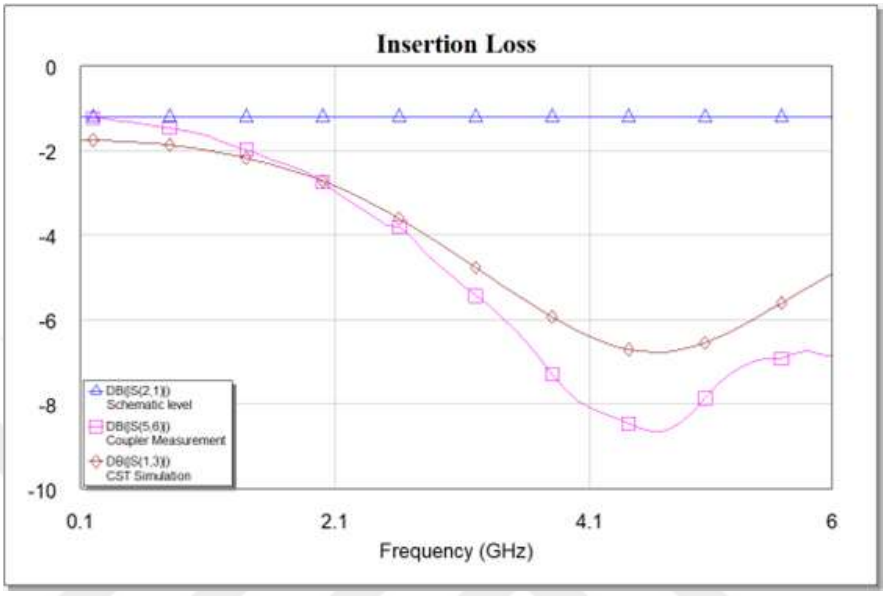


Figure 3.22. Insertion Loss values obtained via schematic level simulations, measurement, and 3D-EM simulations.

3.2.4. Substrate Modelling

Given the need for a high-performance laminate throughout the project, it is essential to accurately model the substrate to be used. However, extracting the substrate parameters is a complex process that heavily depends on the measurement system and its calibration setup. Since s-parameters relate amplitudes, such as the magnitude and phase of traveling waves, with respect to a reference plane, it is crucial to understand how this shift operates both in theory and in practice [41].

When a two-port VNA is calibrated correctly, connecting its two ports with an infinitesimally small transmission line would effectively place both reference planes on top of each other. Consequently, there would be no phase shift in S12 or S21 over the calibrated frequency range, and both S11 and S22 would show perfect matching. However, when producing our test boards, SMA connectors are required to interface with coaxial cables. This means that our measurements will include the effects of both

the SMA connectors and the transmission line, which must be accounted for to ensure accurate results.

One of the most commonly used methods to obtain substrate parameters is the differential phase length method. This technique involves measuring two pieces of transmission lines on the same substrate but with different lengths. By comparing the phase difference between these lines and relating it to the difference in their lengths, the substrate parameters can be determined. This method requires perfect matching between the connectors used, as it involves two pairs of connectors whose phase characteristics must match each other precisely. The method effectively shifts the reference plane to a small piece of line equal to the difference in length between the two lines.

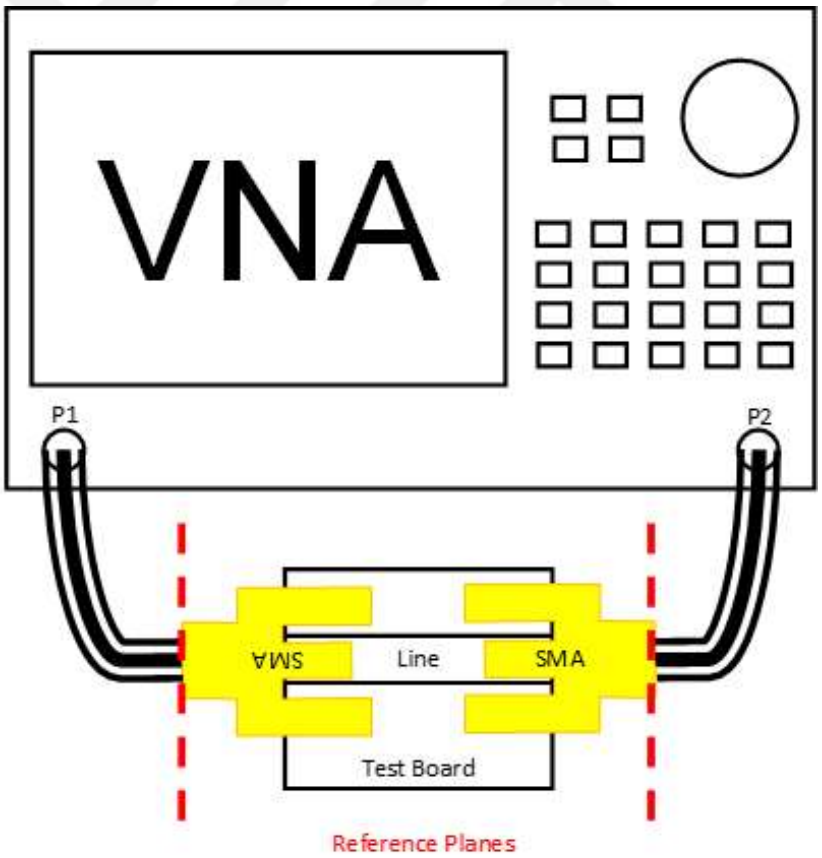


Figure 3.23. Typical two-port vector network analyzer measurement setup.

To illustrate, if it were possible to calibrate the VNA using the shorter line, measuring the longer line would yield results corresponding only to the microstrip line

segment equal to the length difference between the two lines. To test this theory, a Short-Open-Load-Thru (SOLT) calibration kit was produced, and measurements were conducted using different calibration options. This approach ensures that the reference plane shift is accurately accounted for, allowing precise determination of the substrate parameters.

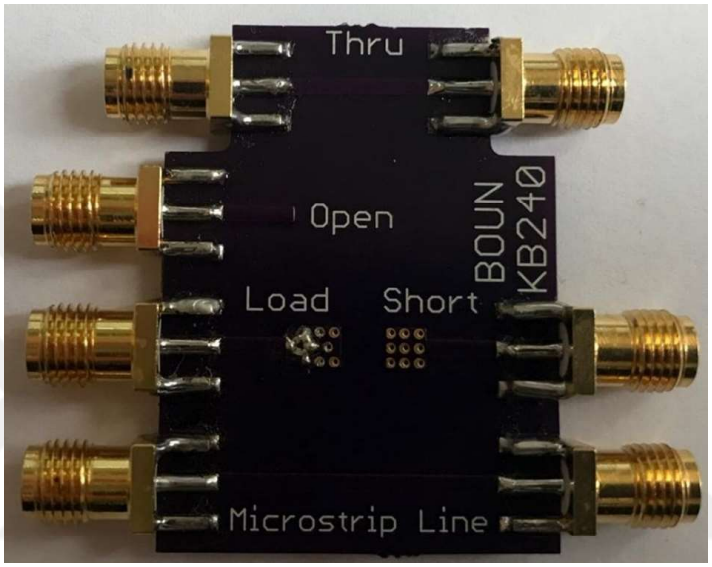


Figure 3.24. Fabricated SOLT calibration kit.

The calibration kit allows for the measurement of two different microstrip lines with lengths of 20 mm and 30 mm. Additionally, it provides load, short, and open standards with 10 mm lines, enabling the reference plane to be shifted 10 mm inside the board from the edge. With this setup, it should be possible to determine both the relative dielectric constant and the loss tangent of the board using the S21 or S12 parameters. This method enhances the accuracy of substrate parameter extraction by precisely accounting for the reference plane shift and ensuring reliable measurements of the board's electrical properties.

To begin with, the network analyzer was calibrated using its own calibration kit from 500 MHz to 13.5 GHz. The 20 mm and 30 mm microstrip lines were measured and their data exported in Touchstone format. Following this, the VNA was calibrated within the same frequency range using the custom calibration kit, and the 30 mm line was measured and again exported in Touchstone format. Ideally, the phase response

of the 30 mm line should match the measurement of the 20 mm line followed by the addition of a 10 mm microstrip line in the simulation. Furthermore, the measured data for the 30 mm line after calibration should ideally correspond to a 10 mm line in the simulation environment. This approach helps ensure the accuracy of phase measurements and validates the calibration process.

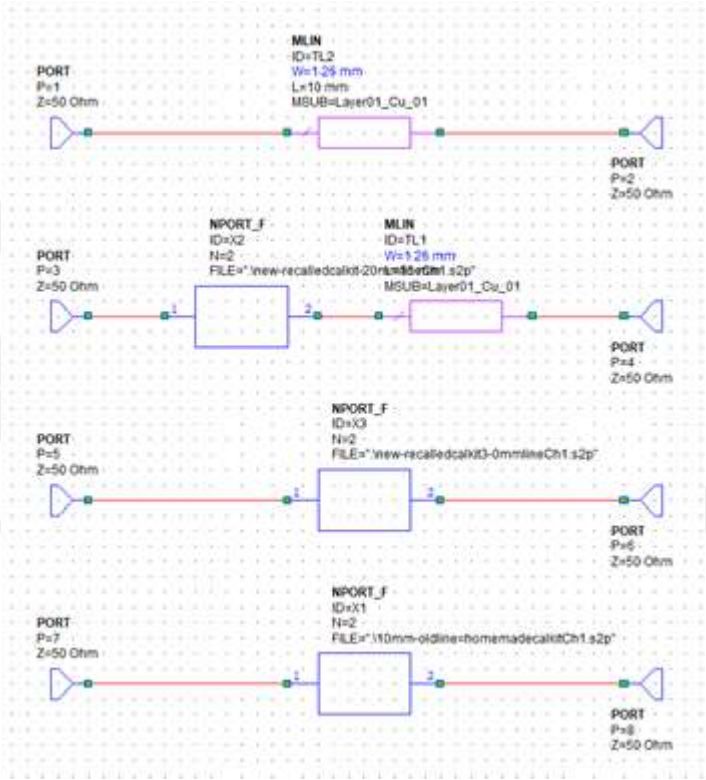


Figure 3.25. Line modeling schematic in AWR Microwave Office.

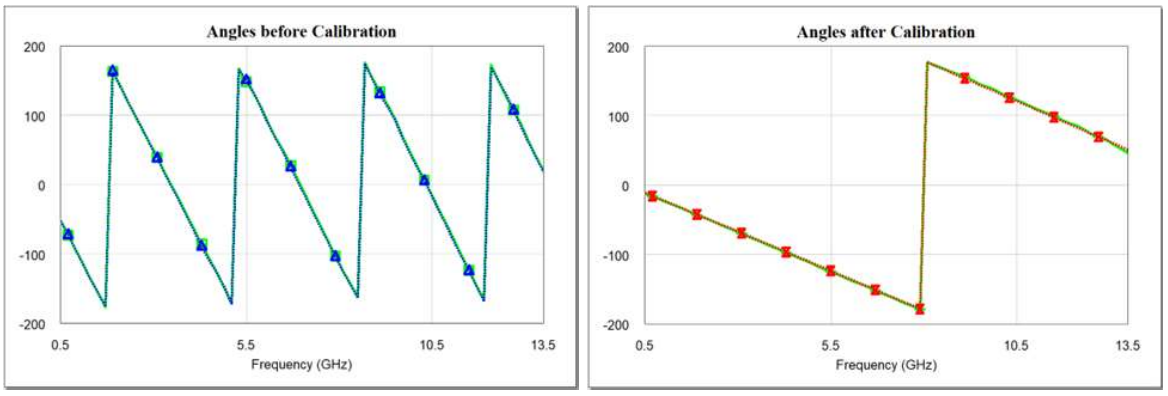


Figure 3.26. Angle responses of microstrip lines.

As can be seen from the figure 3.26, the simulation and measurement results are in agreement. Using the magnitude of S12, it is also possible to calculate the loss tangent. However, the insertion loss of a microstrip line in the simulation appears as a perfect line, making it difficult to align with the measurement results. Additionally, it is possible that the phase response of the connectors is better matched than their magnitude responses. This discrepancy can lead to observed gains in the microstrip lines after calibration, which is not physically possible. Such gains indicate inaccuracies in the calibration or measurement process that need to be addressed.

3.2.5. Conclusion

The SFCW Radar Transmitter Hardware was developed through an iterative design approach, resulting in a transmitter system that meets high standards of precision, stability, and adaptability across a broad frequency range. Key accomplishments include the successful integration of a wideband frequency synthesizer with advanced PLL capabilities, enabling efficient frequency stepping and robust signal resolution critical for high-performance radar applications.

In the Directional Bridge Coupler, design optimization led to a compact, bidirectional bridge structure that consistently maintains a stable coupling value across GHz frequencies. This configuration allows for efficient separation of incident and reflected signals, which enhances measurement reliability. Further refinement of coupling values and reduction of insertion loss have made this component particularly suited for applications where high precision and lightweight design are crucial.

The Substrate Modeling process was instrumental in minimizing signal degradation over the operating frequency range. By carefully selecting high-performance PCB laminates and conducting parameter calibrations, the substrate design supports reliable signal propagation, even under varying environmental conditions. This ensures that signal quality is preserved, enhancing the radar's overall accuracy and efficiency in real-world applications.

Looking ahead, there are several avenues for further development. The frequency synthesizer could benefit from advanced frequency tuning techniques to extend its range and support even more specialized applications. Improvements to the directional bridge coupler, such as incorporating new materials or hybrid integration, may further reduce size and weight, making it more versatile for UAV-based applications. Additionally, enhancing substrate modeling techniques to account for a broader range of environmental factors could support operation in more challenging conditions. These future directions underscore the potential of this transmitter hardware to evolve, meeting the needs of increasingly complex radar applications and broader operational contexts.

3.3. SFCW Signal Processing Algorithms

3.3.1. Introduction

Imaging algorithms play a critical role in shaping and sizing target representations, particularly in radar applications that demand high-resolution imagery. This study examines two primary techniques, which are backprojection and delay and sum beamforming, within the context of SFCW radar, a system well-suited for precise spatial mapping tasks. The backprojection algorithm, a traditional time-domain approach, is widely used in applications such as through-wall imaging (TWI) and GPR [42–44]. By applying an inverse Fourier transform to the received data at each scan point, this method reconstructs images with detailed spatial accuracy, mapping each scan position to its corresponding range profile through round-trip delay calculations. The delay and sum beamforming algorithm, a frequency-domain technique originating from beamforming, offers another approach frequently implemented in TWI, especially when frequency steps are uneven [42, 45].

Each of these methods provides unique benefits for target imaging: backprojection achieves high spatial precision, while delay and sum beamforming enables efficient data processing in environments with variable frequency steps. This section explores the implementation details and practical implications of these algorithms, highlight-

ing how they enable effective radar imaging within the constraints and capabilities of SFCW systems.

3.3.2. Back Projection

In a monostatic SFCW radar system, the signal received at a scan point (x, y) from multiple target points (x_{pi}, y_{pi}, z_{pi}) can be expressed as

$$S(x, y, f_k) = \sum_{i=1}^{P} a(x_{pi}, y_{pi}, z_{pi}) \exp(-\alpha(j2\pi f_k \tau_{pi})), \tag{3.2}$$

where f_k is the frequency point; τ_{pi} is the propagation delay from (x, y) to (x_{pi}, y_{pi}, z_{pi}) and back; $a(x_{pi}, y_{pi}, z_{pi})$ denotes the target reflectivity; and α represents wall attenuation [42]. Backprojection reconstructs the image by applying inverse Fourier transforms to frequency-domain data at each scan point, yielding range-domain data

$$S(x, y, z) = \sum_{k=1}^{L} S(x, y, f_k) \exp(j2\pi f_k (2z/c)), \tag{3.3}$$

where L is the number of frequency points, and R_{pi} is the travel distance from (x, y) to (x_{pi}, y_{pi}, z_{pi}) [46]. For each image pixel, the propagation range R_{pi}, the total travel distance from (x, y) to (x_{pi}, y_{pi}, z_{pi}) and back, is calculated as

$$R_{pi} = 2l_{air \to wall} + 2\sqrt{\epsilon} l_{wall} + 2l_{wall \to air}, \tag{3.4}$$

where $l_{air \to wall}$, l_{wall}, and $l_{wall \to air}$ represent the distances traveled in air, through the wall, and beyond the wall, respectively. Detailed calculations of propagation range are available in [45].

This range is used to locate the range cell in the profile, obtaining the in-phase and quadrature components for all scan points. Summing these values for all scan

points yields pixel values, expressed as

$$I(x_{pi}, y_{pi}, z_{pi}) = \sum_{x=1}^{M} \sum_{y=1}^{N} S(x, y, z = R_{pi}), \tag{3.5}$$

which provides the necessary data for reconstruction of the image [46]. The implementation steps for the backprojection imaging algorithm are as follows:

(i) Collect C-scan data representing the back-scattered electric field $S(x, y, f_k)$ in the frequency domain.
(ii) Perform an inverse Fourier transform on data at each scan point to obtain a range profile $S(x, y, z)$.
(iii) Divide the image map into small pixels.
(iv) Calculate the propagation range from each scan point to every pixel and back.
(v) Use the calculated range to select the range bin in the profile.
(vi) Record the amplitude of the scattered field for each selected range bin.
(vii) Repeat steps (i)-(vi) for all scan points.
(viii) Sum the recorded amplitude values for each pixel.

3.3.3. Delay and Sum Beamforming

The delay and sum beamforming algorithm is a frequency-domain method for image reconstruction [45]. For an SFCW radar system, the signal received at (x, y) from point targets (x_{pi}, y_{pi}, z_{pi}) is given as

$$S(x, y, f_k) = \sum_{i=1}^{P} a(x_{pi}, y_{pi}, z_{pi}) \exp(-\alpha(j2\pi f \tau_{pi})) \tag{3.6}$$

where $a(x_{pi}, y_{pi}, z_{pi})$ represents the amplitude of the reflected signal from the i-th point target, and τ_{pi} is the round-trip delay for the signal [42]. The propagation delay from

(x, y) to (x_{pi}, y_{pi}, z_{pi}) and back is calculated as

$$\tau_{pi} = \frac{2l_{air \to wall}}{c} + \frac{2l_{wall}}{v} + \frac{2l_{wall \to air}}{c}, \tag{3.7}$$

where c and v are the signal velocities in air and through the wall. The distances $l_{air \to wall}$, l_{wall}, and $l_{wall \to air}$ define the signal's path from (x, y) to (x_{pi}, y_{pi}, z_{pi}). Detailed calculations are provided in [45].

3.3.4. Conclusion

The exploration of backprojection and delay and sum beamforming algorithms demonstrates the unique strengths each brings to SFCW radar imaging. Backprojection, with its precise spatial mapping, is particularly valuable for applications requiring detailed target profiles, such as TWI and GPR, where the ability to correlate each scan point with spatial range is crucial. Delay and sum beamforming, on the other hand, offers an efficient approach for scenarios where uneven frequency steps necessitate phase-adjusted imaging, maintaining coherence across complex environments.

Both algorithms address distinct aspects of radar imaging, showing that SFCW radar's flexibility extends beyond hardware configurations to encompass algorithmic adaptability. The implementation insights provided here serve as a foundation for future refinements, such as integrating real-time processing enhancements or adapting these techniques to multi-target scenarios. Together, these imaging algorithms not only enhance the accuracy of SFCW radar systems but also expand their potential in diverse radar applications.

3.4. Implementation of SFCW Algorithms for GB-SAR Systems

3.4.1. Introduction

This section presents the development and implementation of a data acquisition platform tailored to support SFCW radar algorithms for GB-SAR systems. To enable real-world testing and validation of these algorithms, a highly synchronized hardware setup was designed, incorporating a VNA, linear rail system, Arduino controller, and PC interface. This setup allows for controlled, high-resolution data collection across multiple environments, leveraging a linear rail system to precisely synchronize radar signal acquisition with spatial positioning. The chapter also explores advanced signal processing with the BS-MUSIC algorithm, an approach well-suited to indoor applications with complex, reflective environments. By combining hardware innovations with robust signal processing techniques, this study underscores the GB-SAR platform's effectiveness in capturing and analyzing radar data for target localization, ultimately setting a foundation for advanced structural health monitoring and indoor object detection applications.

3.4.2. Realization of a Linear Rail System to Acquire Ground-Based SAR Data

The linear rail system developed in this study is designed for acquiring GB-SAR data. The system comprises a VNA, an antenna, a linear rail, an Arduino microcontroller, and a computer. Each component plays a critical role in enabling precise data acquisition, which is synchronized with the movement of the linear rail.

Vector Network Analyzer: The VNA is a radio frequency test instrument that characterizes the response of a network by sending a stimulus signal to the device under test and measuring the received signal. This allows for measurements of parameters such as gain (magnitude and phase), insertion loss, group delay, and time-domain reflectometry [47]. The PicoVNA 106 is used in this work due to its compact size,

high measurement speed, and exceptional accuracy, making it ideal for portable SAR applications.

Linear Rail System: The linear rail, which spans a length of 2 meters, is actuated by a servo motor chosen for its precise position control capabilities, enabled by an integrated encoder. Proximity sensors are installed at both ends of the rail to prevent the SAR system from colliding with the rail edges. The servo motor is connected to a motor driver, which is controlled by an Arduino microcontroller. An emergency stop button, directly linked to the motor driver, adds an additional layer of safety to the system.

Overall Radar System: The radar setup includes a 0.8-8 GHz broadband ridged horn antenna mounted on a metal carriage that moves along the linear rail. Within this carriage, the vector network analyzer, Arduino, and computer are securely housed. A power amplifier is placed on the transmission side of the VNA, while a low-noise amplifier (LNA) is positioned on the receiver side to improve signal clarity. The complete linear rail system is shown in Figure 3.27.



Figure 3.27. Linear Rail System.

The system is configured to acquire SFCW radar data [48]. Data acquisition is coordinated through a Python script running on a Windows-based computer, which synchronizes the VNA and servo motor to ensure efficient and precise data collection. Initially, the Python code communicates with the VNA to obtain S21 parameters at specific locations across a predefined frequency range. Upon completion, the code

signals the Arduino, which in turn directs the motor driver to move the rail to the next position. This sequence of steps continues until the specified number of points is acquired. The data acquisition scheme is illustrated in Figure 3.27.

Data Acquisition Setup: The data acquisition process was conducted on a set of stairs located near the Electrical & Electronics Engineering Department at Boğaziçi University. The linear rail was mounted on a wheeled table, with two metal reflectors positioned along the stairs to serve as target objects. Reflections from the stairs introduced multipath effects, challenging the SAR system's signal processing capabilities. The setup was configured so that the center of the stairs was aligned with the center of the linear rail, which moves along a 2-meter range ([-1,1]). The rail was positioned 4.7 meters from the stairs and the reflectors. A frequency range of 2 GHz to 6 GHz was swept across 201 frequency points, with a rail step size of 2 cm, yielding a total of 101 observation points. The GB-SAR system setup and target environment are depicted in Figure 3.29.

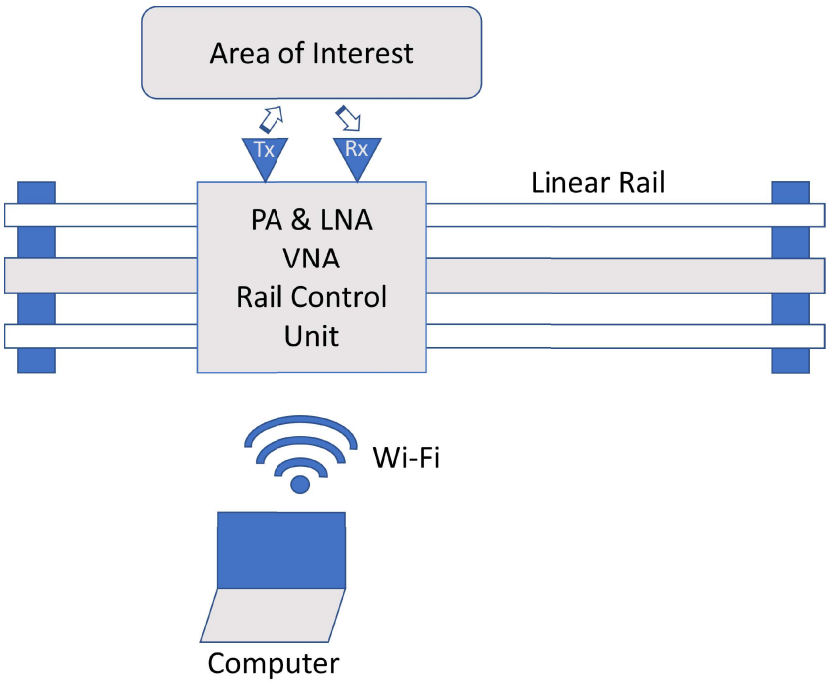


Figure 3.28. Overall system diagram.

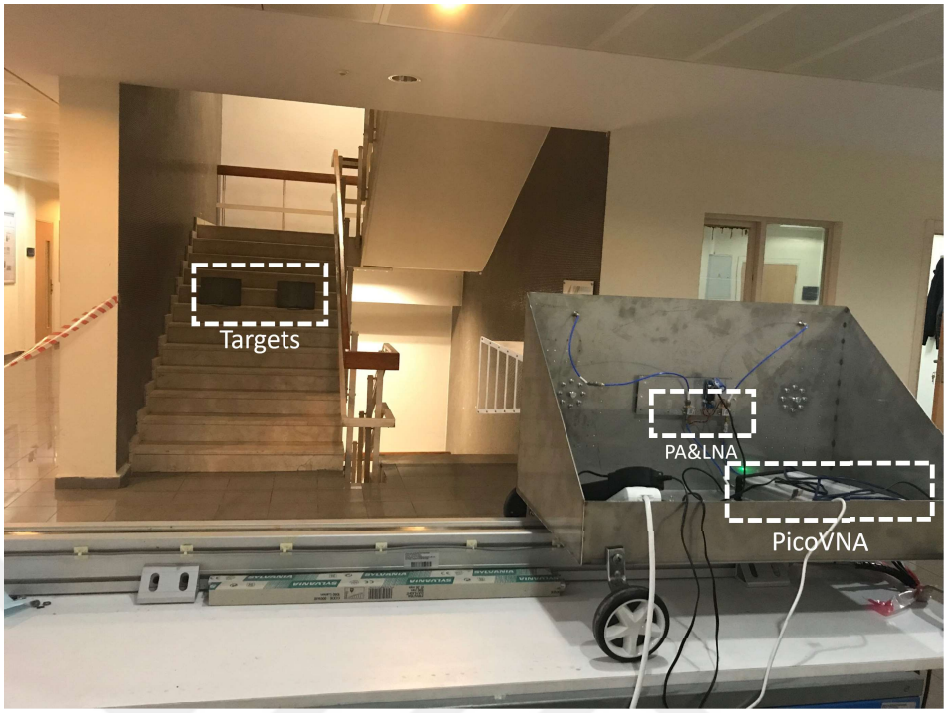


Figure 3.29. The object to be imaged (left), the linear rail (bottom), and the radar system (right).

Following data acquisition in the initial environment shown in Figure 3.29, the setup was moved to a more complex environment, shown in Figure 3.30. Here, the addition of chairs in the surroundings introduced further signal processing challenges by increasing background noise and potential reflections.

This linear rail-based GB-SAR system offers a fully remote-controlled setup for SAR data acquisition. The system was developed by integrating a servo motor and proximity sensors into a linear rail and mounting broadband ridged horn antennas, a VNA, and amplifiers onto a mobile metal carriage. Remotely operated through a computer, this system successfully acquired S-parameters in multiple environments. The remote operability and ease of use of this SFCW radar setup make it an invaluable tool for future signal processing projects, especially those requiring extended measurement durations or operation in remote locations.



Figure 3.30. Measurement setup in the faculty meeting room, adding complexity through additional reflective surfaces.

3.4.3. Experimental Verification of In-door Ground Based SAR Using BS-MUSIC Algorithm

The multiple signal classification (MUSIC) algorithm is an advanced technique in radar imaging that enables high-resolution image formation by dividing the measured data into distinct signal and noise subspaces. It identifies target positions by projecting the steering vector of each point within the search area onto the noise subspace, where peaks in the MUSIC spectrum indicate target locations [48].

A significant challenge in applying the MUSIC algorithm to bistatic systems is obtaining the covariance matrix from a single measurement vector, or snapshot. To overcome this, virtual snapshots are created from uniformly sampled data in k-space, typically requiring an interpolation process. The Beamspace MUSIC (BS-MUSIC) algorithm bypasses this interpolation by processing beamspace data directly instead of raw data [49–51].

In BS-MUSIC, an initial target reconstruction is performed using beamforming, followed by a 2D Discrete Fourier Transform (DFT) to convert the data into uniformly spaced k-space data without needing interpolation [49]. The covariance matrix is then estimated from these virtual snapshots, where data is split into submatrices of dimension $K \times L$, and the covariance matrix is calculated as

$$\mathbf{R} = \frac{1}{N_s} \sum_{n=1}^{N_s} \mathbf{Z}_n \mathbf{Z}_n^H, \tag{3.8}$$

where $\mathbf{Z}_n$ represents each submatrix as a column-ordered vector, N_s is the number of submatrices, and $\mathbf{J}$ is the exchange matrix. By performing eigenvalue decomposition, the covariance matrix is divided into orthogonal subspaces. The basis vectors of the noise subspace are stored in matrix $\mathbf{W}$, allowing the MUSIC estimator to be expressed as

$$P(x, y) = \frac{1}{\mathbf{a}^H(x, y)\mathbf{W}\mathbf{W}^H\mathbf{a}(x, y)}, \tag{3.9}$$

where $\mathbf{a}(x, y)$ is the virtual array steering vector derived from the dimensions of each submatrix.

Measurements were conducted in a test environment at Boğaziçi University, where two reference reflectors were positioned on a staircase to serve as targets, while reflections and multipaths created additional complexity in signal processing. The setup, shown in Figure 3.31, aligns the center of the stairs with the midpoint of the linear rail. Frequencies were swept from 2 GHz to 6 GHz across 401 points, with the rail advancing in 2 cm steps, resulting in 101 observation points.

In this bistatic configuration, both transmitter and receiver were mounted on a 2-meter rail, progressing linearly in 2 cm increments. At each position, the transmitter emits a sinusoidal RF wave,

$$\mathrm{TX} = A \exp(j2\pi f t), \tag{3.10}$$

where f was varied from $f_{\min}$ to $f_{\max}$ in steps of Δf. The receiver detected the reflected signal

$$\mathrm{RX} = A\sigma \exp(j2\pi f(t-\tau)), \tag{3.11}$$

where σ characterizes the scatterer, and τ is the time delay associated with the distance R between the transceiver and scatterer, calculated as $\tau = 2R/c$, with c representing the speed of light. The RF receiver measured the amplitude and phase shift between transmitted and received signals.

To create a SAR image, a $4\,\mathrm{m} \times 4\,\mathrm{m}$ square grid was set up in the area covered by the antennas, with scatterers positioned at the center of each square. The Delay and Sum beamforming algorithm was initially applied to generate a coarse image, shown in Figure 3.32, which aligns well with the physical environment and highlights the stairs and corner reflectors. The BS-MUSIC algorithm was subsequently applied to improve the image resolution, focusing specifically on isolating the reflectors.

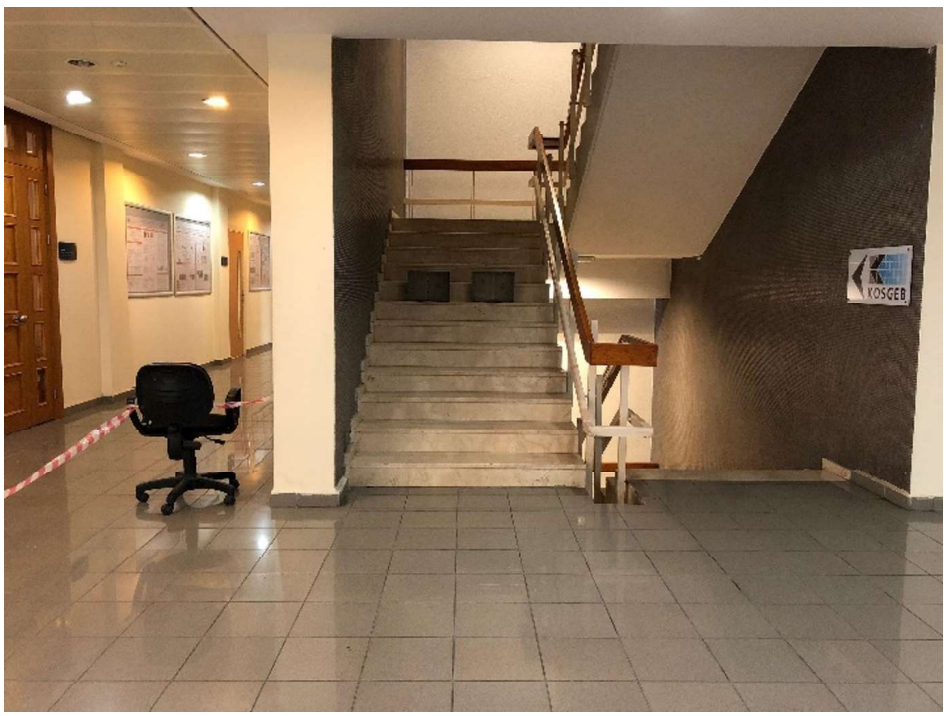


Figure 3.31. Measurement environment showing the setup at Boğaziçi University, © 2018 IEEE.

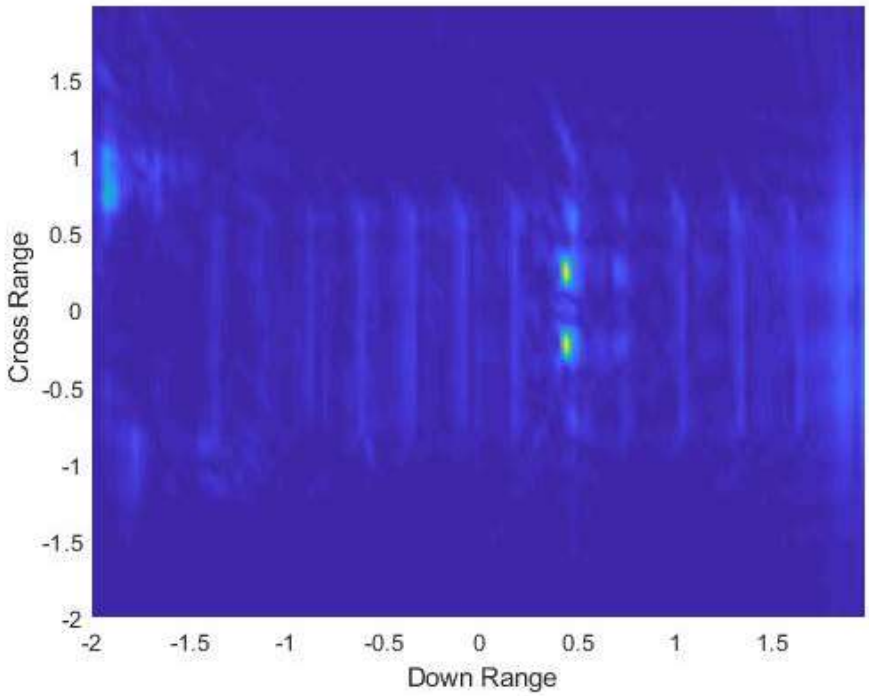


Figure 3.32. Reconstructed image using the Delay and Sum beamforming algorithm, © 2018 IEEE.

As depicted in Figure 3.33, the BS-MUSIC algorithm effectively filters out lower RCS (Radar Cross Section) reflections from the stairs and walls, thereby isolating the reflectors as primary targets.

This study presents a remote-controlled SAR measurement system designed for indoor applications, specifically for reconstructing conductor targets. The system gathered indoor S-parameter measurements within a controlled environment, applying the BS-MUSIC algorithm to identify target locations. Initially, the Delay and Sum beamforming approach was used to generate a basic image, which was then transformed into beamspace data. The BS-MUSIC algorithm further enhanced the image by assigning a steering vector to each cell in the reconstruction area and calculating its projection onto the noise space of the beamspace data. Comparisons with traditional beamforming methods reveal that the BS-MUSIC algorithm effectively reduces the impact of non-target reflections and improves image resolution.

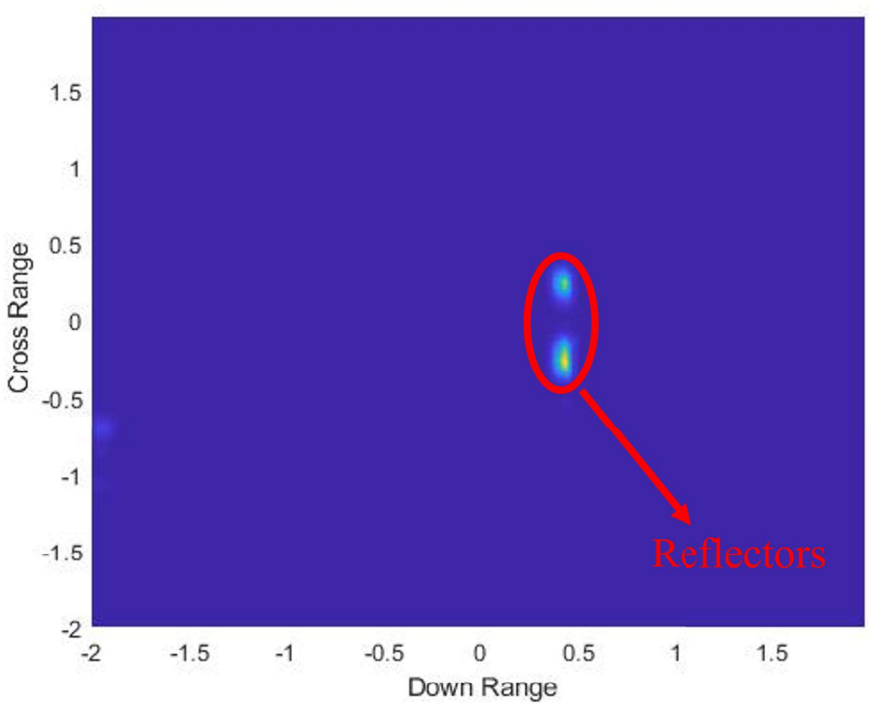


Figure 3.33. Image reconstruction with BS-MUSIC algorithm showing isolated reflectors, © 2018 IEEE.

3.4.4. Conclusion

The successful realization of a remote-controlled, linear rail-based GB-SAR system marks a significant step toward high-precision indoor radar applications. Through an innovative integration of synchronized data acquisition, advanced signal processing, and adaptable hardware, the GB-SAR system demonstrated reliable data capture across varied environments. The application of the BS-MUSIC algorithm further enhanced the radar's ability to isolate and resolve targets within reflective environments, a capability essential for applications requiring precise localization and noise suppression. Moving forward, this system's design offers a versatile platform for further exploration, paving the way for future advancements in SAR-based structural health monitoring, remote detection, and other indoor radar applications where high resolution and adaptability are essential.

3.5. Structural Health Monitoring and Change Detection Algorithm

3.5.1. Introduction

This section introduces a GB-SAR system designed specifically for structural health monitoring and precise change detection. Employing an interferometric SAR algorithm, this system leverages two sequential SAR images to achieve sub-centimeter displacement accuracy. By sweeping the frequency and moving the radar system along a linear actuator, the radar captures a dataset representing both spatial and frequency diversity. This data collection process enables the generation of high-resolution images of the target area, with the target area further divided into virtual pixels for refined image resolution and accurate displacement mapping. The system also incorporates a phase interferometry technique that can detect millimeter-level structural displacements, a critical feature for early detection of potential issues in infrastructure. Through experimental validation, the system demonstrates its effectiveness for both indoor and outdoor monitoring, showcasing its capability to capture, process, and analyze complex structural changes in real time.

3.5.2. Overview of the Interferometric SAR Algorithm

The core of the structural monitoring approach is an interferometric SAR algorithm that relies on two consecutive SAR images to detect changes over time [52]. Each SAR image is acquired by combining frequency diversity with spatial positioning, achieved by moving the radar system along a linear actuator and sweeping through a defined frequency range. The radar system, illustrated in Figure 3.34, illuminates the target area while the transmitter emits continuous electromagnetic signals in frequency steps of Δf. The receiver collects reflections, resulting in a comprehensive dataset of raw radar signals, $S_r(l_b, f_a)$, recorded across the radar's position (l_b) and frequency (f_a) domains, forming a dataset of $N_f \times N_l$.

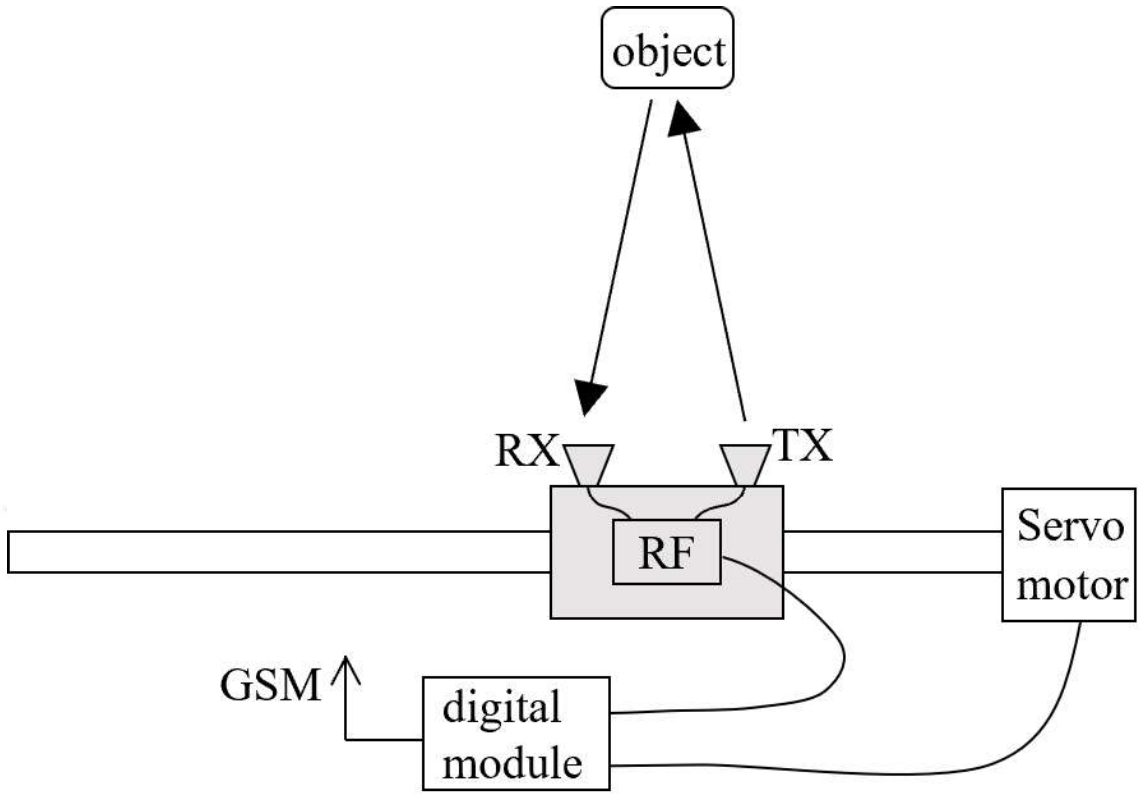


Figure 3.34. Top view of the simplified diagram illustrating the GB-SAR system.

After collecting the raw radar data, SAR images can be generated by refining the reflections from the target area. To create a radar image, the target region is divided into virtual pixels, as shown in Figure 3.35. This figure illustrates a top-view pixelization of the target area as detected by the ground-based SAR system, with x and y axes corresponding to the radar's azimuth and range directions, respectively. Each pixel is a square with edge length Δp, and each pixel's reflection in response to the radar signals is represented by σ_{mn}, where m and n index the X and Y coordinates. It is assumed that the reflections are concentrated at the pixel centers. The radar signal received at l_b for frequency f_a can be expressed as

$$S_r(l_b, f_a) = \sum_{m=1}^{M} \sum_{n=1}^{N} L_{sys} \sigma_{mn} e^{-j2\pi f_a \frac{d_1(l_b, p_{mn}) + d_2(l_b, p_{mn})}{c}}. \tag{3.12}$$

Here, M and N define the dimensions of the observed region illuminated by the radar. The term σ_{mn} represents the reflection values at each pixel (corresponding to $\sigma(x, y)$), l_b denotes the radar's position, and d_1 and d_2 are the distances from the

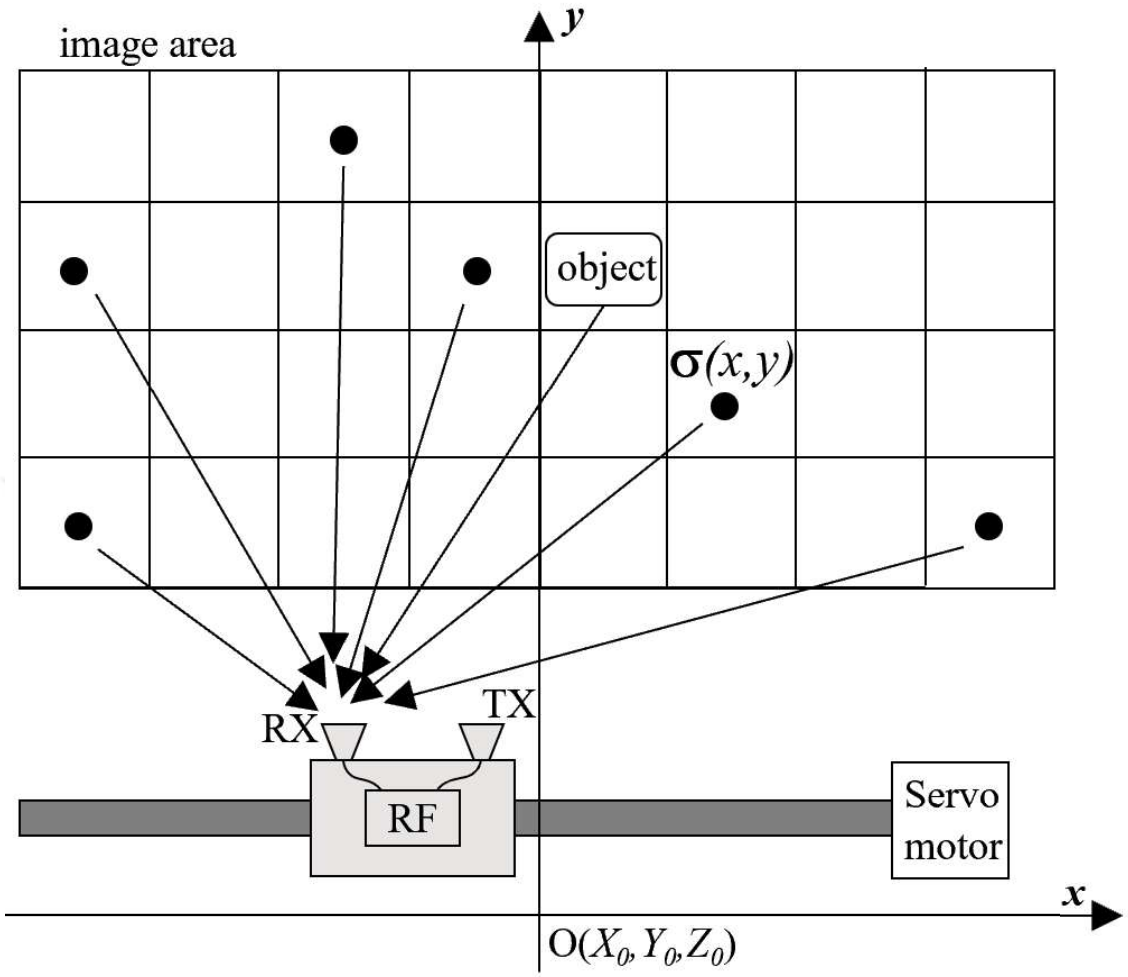


Figure 3.35. Top view of the virtually pixelized target area as detected by the ground-based SAR.

pixel to the transmitting and receiving antennas, respectively. L_{sys} indicates the total electromagnetic path loss of the system. The radar reflection coefficient σ_{mn} for each pixel is calculated as

$$\sigma_{mn} = \sum_{b=1}^{N_l} \sum_{a=1}^{N_f} \frac{K S_r(l_b, f_a)}{N_l N_f} e^{-j2\pi f_a \frac{d_1(l_b, p_{mn}) + d_2(l_b, p_{mn})}{c}}, \tag{3.13}$$

where N_l and N_f represent the dimensions of the raw radar data $S_r(l_b, f_a)$ collected by the receiver. The radar unit traverses the X-axis, with its position indicated by l_b, while operating at frequency f_a at each position. σ_{mn} is the radar reflection coefficient at the pixel corresponding to the $(m, n)^{th}$ index. K denotes the total amplitude of

propagating and reflected electromagnetic waves, and c is the speed of light in air. The SAR image is generated by computationally processing this equation.

Since the radar's range resolution exceeds the desired detection accuracy, a phase interferometry technique was developed to detect millimeter-level shifts in structural elements. Phase interferometry, represented as $\varphi(x, r)$, is induced by displacement $\Delta d(x, r)$ between two radar images, obtained from electromagnetic waves in the air. $\varphi(x, r)$ is given by

$$\varphi(x, r) = \frac{-4\pi}{\lambda} \Delta d(x, r). \tag{3.14}$$

In this equation, λ is the wavelength of the electromagnetic waves, and $\Delta d(x, r)$ denotes the displacement. Here, x is the azimuth (horizontal) and r is the range axis. The change in radar images can then be calculated as

$$\Delta d(x, r) = \frac{-\lambda}{4\pi} \varphi(x, r). \tag{3.15}$$

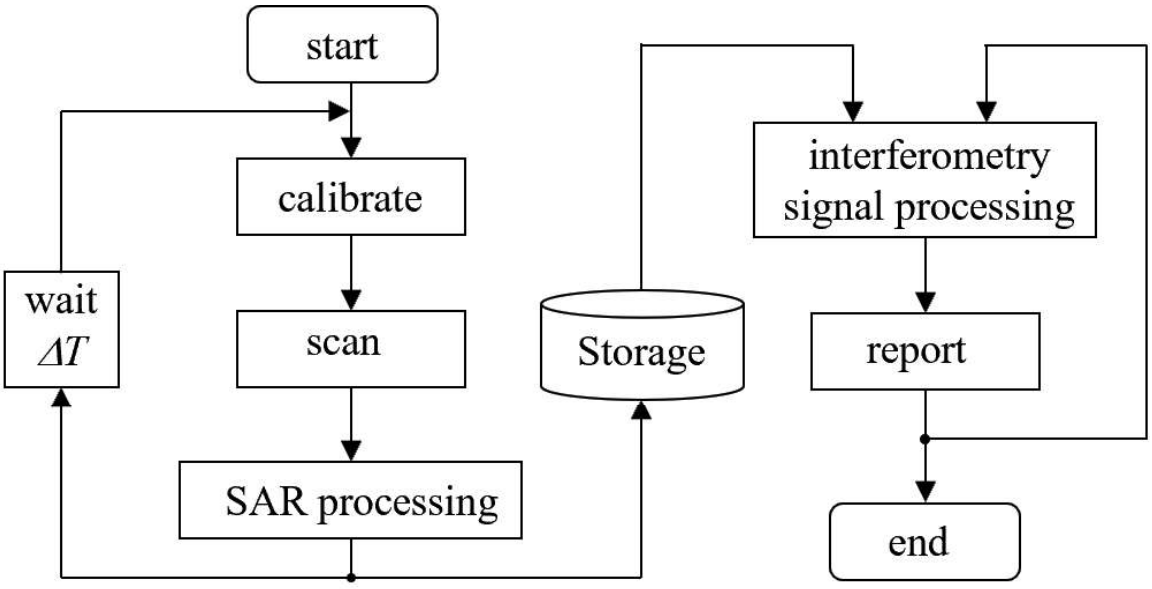


Figure 3.36. Flowchart of the proposed structural health monitoring and change detection algorithm.

Figure 3.36 illustrates the structural health monitoring and change detection algorithm. Following system initialization and calibration, the SAR system scans frequency and stroke length. The system formats the collected raw reflection data and sends it to a remote processor, where SAR imaging is achieved using Compute Unified Device Architecture (CUDA)-supported GPU parallel processing. After calibrating its initial position, the mechanical system resamples the environment after a wait time of Δt. With two SAR images acquired, the phase interferometry technique is applied based on previous images in the database. In this work, the detection interval between consecutive scans is set to 30 minutes, allowing the system to continuously report displacements and their coordinates in the monitored structure.

A series of experiments were conducted to validate the algorithm's ability to detect structural changes. The algorithm's performance was assessed based on these experimental results, focusing on the pixel-by-pixel interferometric phase changes between successive SAR images.



Figure 3.37. Side view of the GB-SAR system and concrete blocks.

The experiments were conducted in two settings. In the first, concrete blocks were examined to detect displacements remotely. In the second, the system monitored a building's surface over day and night to observe structural changes. Detailed experimental setups are provided below.

3.5.3. Concrete Block Test

This experiment involved observing concrete blocks. Figure 3.37 shows a side view of the experimental setup featuring the GB-SAR system and two columns of concrete blocks. Eight concrete blocks of 20x20x20 cm were stacked in each column, with a 1-meter gap between the columns, and the radar system was positioned 5 meters away.

To assess deformation detection, two measurements were taken. During the first measurement, radar data was collected from the area shown in Figure 3.38(a), producing the SAR image in Figure 3.38(c). Next, the top two blocks in the right column were shifted 5 mm toward the wall (Figure 3.38(b)), and another measurement was taken to produce the SAR image in Figure 3.38(d). While deformation is not directly visible in these SAR images, the proposed algorithm successfully identified the deformation.

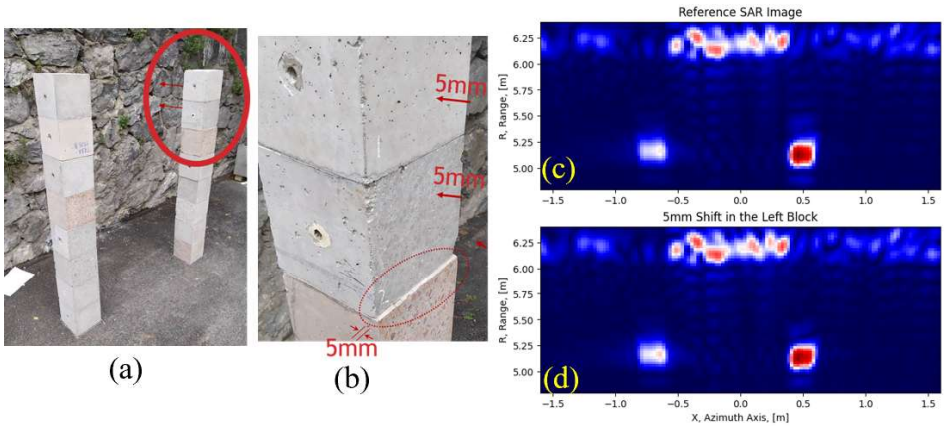


Figure 3.38. Images show (a) initial setup with marked blocks, (b) blocks shifted by 5 mm, and SAR images (c) before and (d) after the shift.

Two SAR datasets were processed by the algorithm to identify deformation dimensions and coordinates. As shown in Figure 3.39, the system detected a 4.33 mm displacement at coordinates 0.50 m and 5.03 m along the x and y axes, respectively. The measurement error was approximately 13.4%, demonstrating the system's suitability for applications requiring millimeter-scale deformation detection, such as infrastructure monitoring [53, 54].

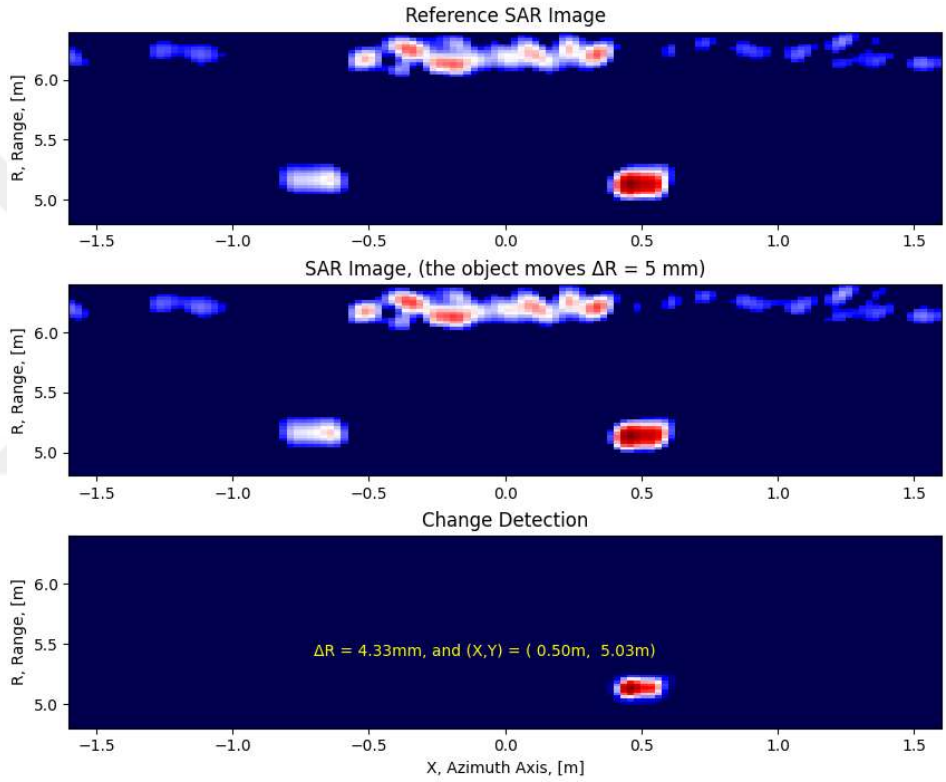


Figure 3.39. SAR images showing algorithm performance: initial (top), post-displacement (middle), and detected changes (bottom).

3.5.4. Building Monitoring

To monitor building exteriors, the radar system was positioned as shown in Figure 3.40, facing a building 13 meters away. A test object was placed within a window opening and initially kept stationary before small displacements were introduced. SAR images were collected to evaluate the SAR and change detection algorithms.



Figure 3.40. Photographs of the structural monitoring setup: (a) target view, (b) radar system view.

Operating in the 5–6 GHz frequency range with 1001 frequency steps, the radar generated a synthetic aperture. After an initial measurement, no change was detected. Subsequently, the object was shifted by 0.44 mm, 1 mm, 5 mm, 10 mm, and 10.44 mm. The change detection software successfully identified the displacements, as illustrated in Figure 3.41 for a 0.44 mm shift.

3.5.5. Conclusion

The development and validation of this ground-based SAR system represent a significant advancement in structural monitoring and change detection technology. Using an interferometric SAR algorithm with GPU-based parallel processing, the system successfully captures sub-centimeter structural changes, as evidenced by experimental results. Tested under controlled conditions with concrete blocks and in a more complex outdoor setting on building exteriors, the system accurately detected movements as small as 440 μm. The remote transmission of raw data to a server for processing and continuous monitoring enhances its practicality for real-time structural health assessment. By offering early detection capabilities that surpass conventional methods, this SAR-based approach presents a reliable solution for infrastructure monitoring

and extends the potential applications of radar data in change detection and object monitoring, setting the stage for future innovations in structural health management.

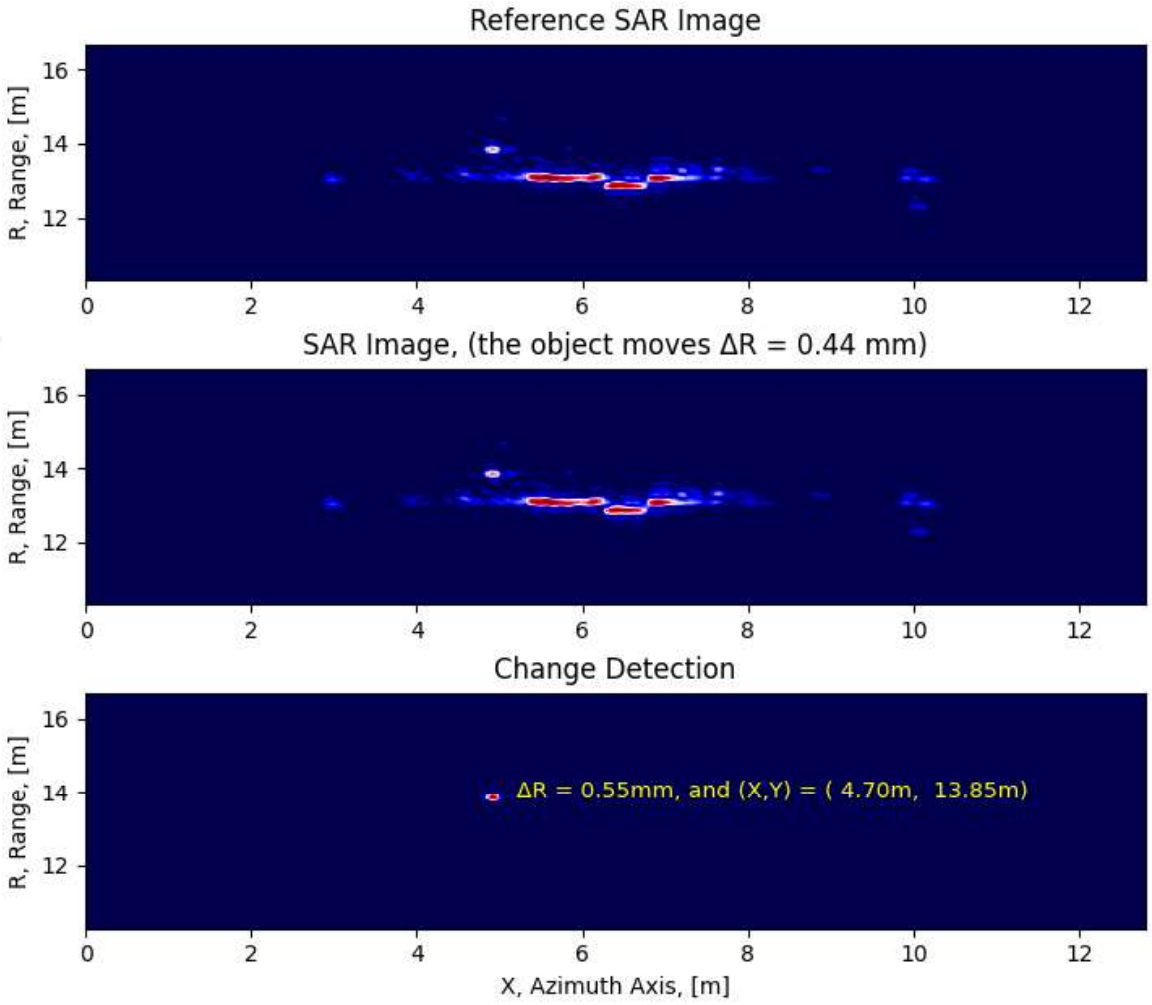


Figure 3.41. SAR images showing structural monitoring: initial (top), post-change (middle), and detected changes (bottom).

3.6. Conclusion

The development of the SFCW radar system has demonstrated its viability and adaptability for high-resolution applications, particularly those requiring precise spatial mapping and structural monitoring. This chapter has detailed the iterative design process undertaken to enhance each component, focusing on the frequency synthesizer, directional bridge coupler, and substrate modeling, which are all crucial to achieving optimal system performance.

Table 3.1. Measured radar displacement values

Object's Displacement (mm)	**Measured Radar Measurement (mm)**	**Difference (%)**
0.44	0.55	25.0
1	1.30	29.8
5	5.03	0.5
10	12.34	23.4
10.44	12.73	21.9

In the frequency synthesizer design, each iteration addressed specific challenges, such as unwanted spurs and frequency stability, ultimately resulting in a high-performing module capable of maintaining signal integrity across a broad frequency range. By the third variant, the integration of a TCXO and elimination of excess noise and spurs achieved an SFDR level of 55 dB, illustrating the significant refinement and stability achieved through targeted adjustments in the circuit design and reference frequency management.

The Directional Bridge Coupler also benefited from iterative improvements, leading to the implementation of a bi-directional bridge structure with enhanced coupling performance, reduced insertion loss, and stability up to 6 GHz. By studying foundational work and adapting the design to optimize coupling and weight, the project produced a compact, precise component essential for UAV applications. The high directivity and minimal interference from reflected signals underscore the achievement of measurement reliability and system compactness which are key parameters for any UAV-mounted radar system.

Substrate modeling was critical in refining signal propagation by accurately modeling the PCB laminate and compensating for dielectric property variations. Extensive calibration with the differential phase length method and custom calibration kit enabled reliable parameter extraction, essential for sustaining performance across GHz frequencies and varied environmental conditions. This groundwork has set a strong

foundation for ensuring high signal fidelity, even under demanding conditions, supporting future radar applications with complex requirements.

In summary, each component of the SFCW radar was enhanced through careful iterations to balance precision, power efficiency, and system compactness, which are characteristics essential for UAV-based applications. The thorough integration of transmitter hardware, coupler design, and substrate modeling has resulted in an adaptable, robust SFCW radar system suited to high-resolution structural monitoring and environmental sensing.

Looking forward, FMCW radar technology presents a compelling alternative for applications requiring real-time imaging and efficient frequency stepping. While SFCW radar has excelled in spatial precision, FMCW systems offer advantages in real-time processing and hardware simplicity, making them particularly suitable for dynamic UAV applications. The insights and technical accomplishments from this SFCW radar design, such as refined substrate modeling and frequency tuning techniques, will inform the design of FMCW systems, ensuring that signal fidelity and resolution remain high as the project transitions to this technology.

The transition to FMCW radar, detailed in the subsequent chapters, represents an opportunity to apply these advancements in a more streamlined configuration that balances high resolution, adaptability, and real-time operation, meeting the evolving demands of UAV-based radar applications.

4. DESIGN OF FMCW RADAR SYSTEM

4.1. Introduction

The development of FMCW radar systems has opened new possibilities for high-resolution imaging and real-time sensing across various applications. FMCW radar, distinguished by its continuous frequency modulation capability, has proven especially valuable in UAV-based remote sensing, weather monitoring, and environmental observation, where accuracy, adaptability, and resistance to environmental interference are essential. In contrast to pulsed or SFCW radars, FMCW radar's continuous frequency sweep enables precise range measurements while maintaining a lightweight, power-efficient design, qualities crucial for the constraints of UAV deployment.

This chapter explores the theory, hardware design, and signal processing of an FMCW radar system developed to meet demanding performance specifications. The content presented in this chapter is based on the author's prior work, published in [55], where significant aspects of the system's design, implementation, and performance evaluation were detailed. Operating in the C-band frequency range, the system balances range, resolution, and clutter rejection, making it suitable for applications requiring penetrative observation in adverse conditions, such as rain, fog, or light foliage. The FMCW system's design focuses on achieving high-range accuracy and stability, driven by the need to overcome noise, synchronization, and efficiency challenges inherent in compact UAV systems.

The chapter is structured as follows: it begins with the theoretical foundations of FMCW radar, examining the principles that govern range measurement and resolution to establish the context for the system's design. This is followed by a detailed breakdown of the hardware, including the transmitter, receiver, power circuitry, and antennas. Each component is carefully chosen and optimized to support synchronized and reliable performance while addressing the constraints of UAV applications. The

chapter then discusses backprojection-based signal processing algorithms, which enable high-resolution imaging through efficient data processing and real-time capabilities essential for UAV operations.

Through these sections, this chapter highlights the integration of precise hardware design with advanced signal processing to create a robust and efficient FMCW radar system. By addressing the practical challenges of noise minimization, range accuracy, and real-time processing, the system is designed to perform effectively in modern radar applications, meeting both performance and efficiency targets. This chapter not only describes the theoretical foundation but also showcases a highly optimized hardware-software integration, tailored to UAV-specific challenges.

4.2. Frequency Modulated Continuous Wave Radar Theory

Consider a FMCW radar. Let the position of the radar be denoted by $\mathbf{r} = [\mathbf{r_x}, \mathbf{r_y}, \mathbf{r_z}]^\mathbf{T}$ and its orientation is by $\mathbf{\Omega}$=[ϕ,θ,ψ]^T. Consider the signal $x_e(t)$ emitted by the transmitter with f_1 and f_2 representing the lowest and the highest frequencies respectively and τ being the signal period,

$$x_e(t) = \cos(2\pi(f_1 + \frac{f_2 - f_1}{\tau}t)t). \tag{4.1}$$

Suppose that there is an object at position $\mathbf{o} = [\mathbf{o_x}, \mathbf{o_y}, \mathbf{o_z}]^\mathbf{T}$. Here, we assume that the outgoing and incoming waves are in the same period. Note that while outgoing and incoming waves in different periods can be correlated with each other with more advanced algorithms, considering the pulse duration we can use, the theoretical range value is very high and this range value is limited due to other parameters. Therefore, the above-mentioned assumption can be made. The received signal $x_r(t)$ is

$$x_r(t) = \cos(2\pi(f_1 + \frac{f_2 - f_1}{\tau}(t - \delta t))t) \tag{4.2}$$

with a delay of δt. If $d = |r - o|$, then δt is equivalent to

$$\delta t = \frac{2d}{c}, \tag{4.3}$$

where c is the speed of light. The bandwidth of the system can be defined as $f_2 - f_1$. Through mixing the outgoing wave in Equation (4.1) and incoming wave in Equation (4.2) and then applying a low pass filter to eliminate high frequency components, the received signal is transformed as

$$x'(t) = \cos(2\pi(\frac{f_2 - f_1}{\tau} t_d)t). \tag{4.4}$$

Thus, a single tone sinusoidal is obtained with a frequency that is proportional to δt. Substituting Equation (4.3) into Equation (4.4), received signal becomes

$$x'(t) = \cos(2\pi(\frac{2(f_2 - f_1)}{\tau c} d)t). \tag{4.5}$$

From Equation (4.5), the frequency of x' exhibits a linear relationship with the range, which is expressed as

$$f'(d) = \frac{2(f_2 - f_1)}{\tau c} d. \tag{4.6}$$

The sensing of the radar is defined by three parameters: Maximum range R^*, range resolution ΔR^* and FFT resolution $\Delta\omega^*$. The maximum range R^* of FMCW radar depends on three factors. First, it depends on the maximum distance that can be traveled during one period of the FMCW signal - namely:

$$R_1^* = \frac{c\tau}{4}. \tag{4.7}$$

Secondly, the maximum range also depends on the sample rate of the receiver. The theoretical maximum frequency of the FMCW radar output is equal to the bandwidth of the system, which is generated by targets at the theoretical maximum range. Since the

sampling rate of the ADC should satisfy the Nyquist criteria, meeting this requirement might be impractical for high-bandwidth systems. However, given that the theoretical range is often very high, reflections beyond a certain distance become inseparable from noise. Thus, a reasonable maximum range can be achieved with a slower sampling rate, and this relationship is expressed as

$$R_2^* = \frac{c\frac{f_s}{2}\tau}{4(f_2 - f_1)}. \tag{4.8}$$

The maximum range of the radar can also be calculated based on parameters such as the frequency, the transmitted power, the antenna gains, and the minimum detectable power level. This calculation is expressed as

$$R_3^* = \sqrt[4]{\frac{P_s G^2 \lambda^2 \sigma}{P_{min}, (4\pi)^3}}, \tag{4.9}$$

where P_s is the transmitted power, G is the antenna gain, λ is the wavelength of the signal, σ is the RCS value of the object and P_{min} is the minimum power value that can be detected. The maximum range of the radar,R^*, is determined by the lowest value among the ranges defined by the signal period, the sampling rate, and the transmitted power. This relationship is given as

$$R^* = \min(R_1^*, R_2^*, R_3^*,). \tag{4.10}$$

Range resolution ΔR^* is a parameter that defines the minimum distance that must be between two objects that are close to each other to be able to distinguish them from each other. The theoretical and practical values of the range resolution are limited by different parameters. The theoretical range resolution is determined by the requirement that the waves reflected from two different objects do not overlap and is expressed as

$$\Delta R^* = \frac{c}{2(f_2 - f_1)}. \tag{4.11}$$

Reflected waves from different ranges must fall into different FFT bins in the output spectrum to be able to reach the theoretical range resolution. Otherwise, it is practically impossible to distinguish between two objects falling into the same FFT bin in the spectrum. Parameters such as the number of samples taken per pulse and the sampling frequency help achieve the theoretical value. FFT range resolution $\Delta\omega^*$ is also important because it determines how sharply the distance of the object can be determined and is given by

$$\Delta\omega^* = \frac{c}{4(f_2 - f_1)}. \tag{4.12}$$

Equation (4.12) reveals that a single pulse period FFT with FFT length matching the number of samples is sufficient to provide range resolution, since a lower range resolution value indicates a better system.

With these theoretical principles established, the hardware design aims to realize these capabilities in a compact, high-performance system. Building on these principles, the hardware design presented here leverages advanced components and configurations to ensure accurate and reliable range measurements within compact, UAV-compatible architecture.

4.3. FMCW SIMO Radar Hardware Design

4.3.1. Introduction

The hardware design methodology emphasizes efficient integration of components and optimized power management to meet UAV constraints, ensuring high-resolution and real-time sensing capabilities. It is tailored for reliable performance in challenging environments, with a single transmitter and two receiver channels enhancing range accuracy and spatial resolution.

This design is implemented in a radar transceiver module operating in the C-band frequency range, supporting a SIMO radar system. The C-band offers access to a wide bandwidth and propagation characteristics that enable penetrative observation through challenging environmental conditions, such as heavy rain and foliage. These characteristics provide a balance between range, resolution, and clutter rejection, making it ideal for applications like remote sensing and weather observation.

Key considerations for the hardware design include signal integrity, noise reduction, and effective power distribution. Careful selection and optimization of the transmitter, receiver, power systems, and antennas ensure that the implemented hardware remains lightweight and power-efficient, addressing the unique requirements of UAV applications.

The transmitter circuit consists of a PLL-based chirp generator followed by a power amplifier, with its output fed to the transmitter antenna. PLL-based chirp generation offers reduced phase noise and increased frequency ramp linearity compared to directly driving a voltage-controlled oscillator [56]. The output is then divided into two using a resistive delta divider to provide feedback for the loop. The power level of the chirp generator is adjusted using a chip attenuator to prevent signal distortion due to the limited dynamic range of the power amplifier. A portion of this output power is coupled using a directional coupler to provide a reference signal for the receiver. The overall system diagram for the FMCW radar system is shown in Figure 4.1.

Additionally, the selection of antennas plays a vital role in determining overall system performance, impacting bandwidth, gain, and weight. By using PCB log-periodic antennas, the design addresses bandwidth requirements and adheres to the strict weight limitations of UAV platforms.

The transceiver board features two identical receiver channels to provide receive diversity. It is crucial to ensure that the amplifiers remain below their saturation level for the strongest signals received, which are mostly from close-range high reflectivity

targets, on-board crosstalk, and antenna coupling. On-board crosstalk and antenna coupling can cause false targets at very close range, but these can be neglected, which is one of the main advantages of FMCW radar systems. The received signals are amplified using a low noise amplifier chain and then converted to balanced signals using a commercially available balun. These two channels are then mixed with the transmitted signal using a dual-channel double-balanced mixer. The mixer output is biased and converted to a single-ended signal using another balun. Range compensation and additional gain blocks are then applied to the baseband signal, which is subsequently sampled using a 14-bit ADC.

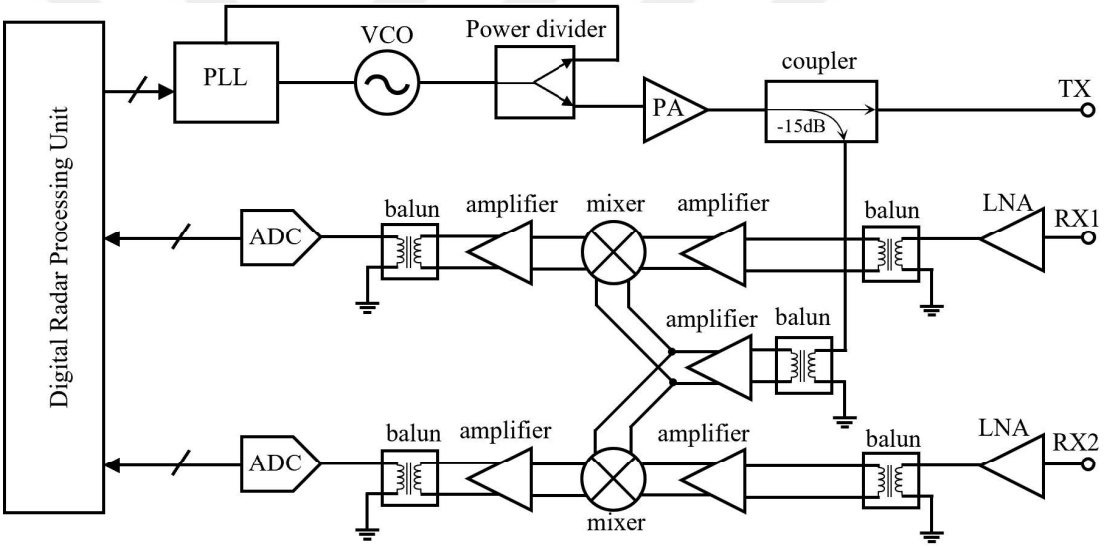


Figure 4.1. FMCW Radar Board Diagram.

The top-level board consists of three main subcircuits: power, transmitter, and receiver circuits which can be seen in Figure 4.2. Additionally, the design includes the RedPitaya extension header 2, which is used to synchronize the RedPitaya with the transmitter. The RedPitaya will also be responsible for reading the power detector output and handling SPI communication with the chirp generator.

The RedPitaya extension connector #2 is connected using an Insulation Displacement Connection (IDC) 2x13 cable, which is robust and sturdy to prevent possible connectivity issues during flight, which can be seen in Figure 4.3. The ADC clock, a 125 MHz LVDS output, will be used as the reference clock in the transmitter. SPI pins

will be used to program the ADF4158, and the analog input pin will be used to read the power detector output.

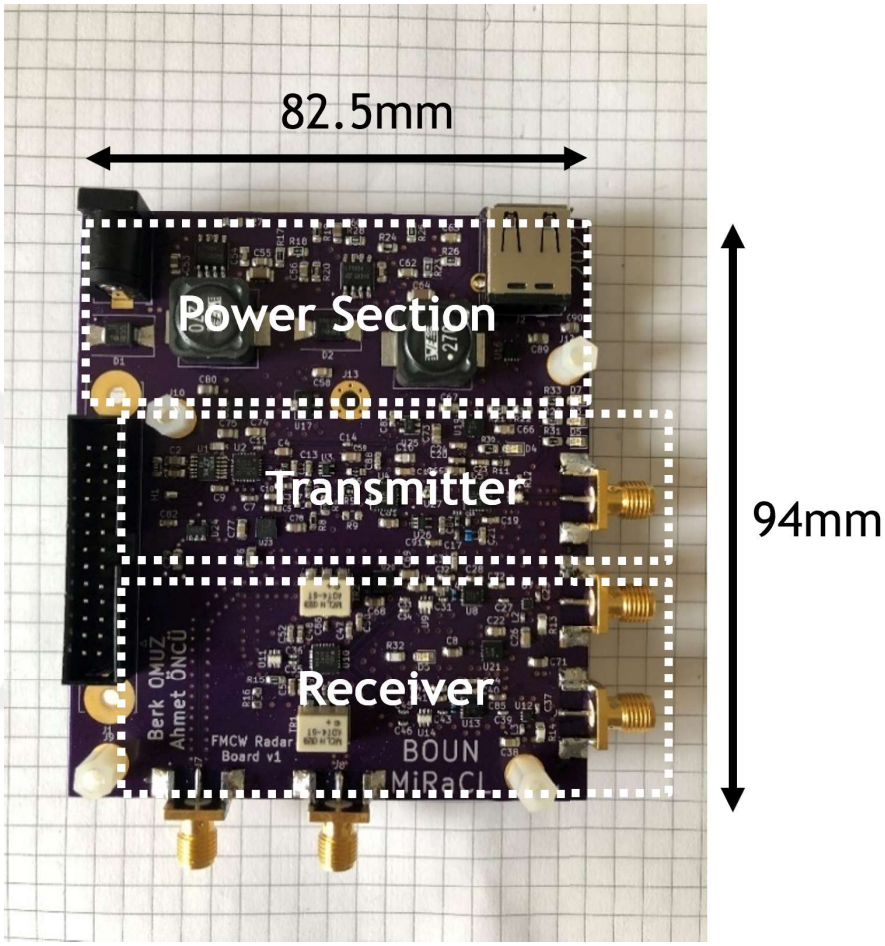


Figure 4.2. Designed board.

4.3.2. Power Design

The power board is a crucial component of the radar system, ensuring stable and efficient power delivery to various subcircuits. To provide a stable, noise-reduced power supply across diverse circuits, the power design incorporates switching regulators followed by linear regulators. It consists of two L7980A step-down switching regulators, which are employed to generate 5.5V DC outputs from a 4S battery input (14.8V nominal). The L7980A is a high-efficiency, high-current switching regulator capable of delivering up to 3A, making it suitable for powering demanding circuits in the radar system [57].

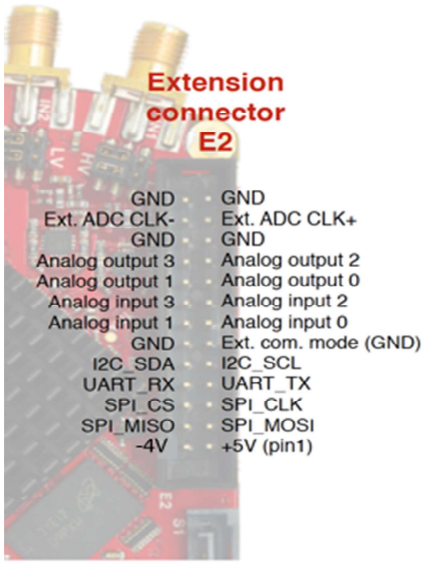


Figure 4.3. RedPitaya Extension connector #2.

The use of switching regulators like the L7980A is essential in such systems due to their high efficiency, especially when there is a significant difference between the input and output voltages. Switching regulators can efficiently step down the voltage with minimal power loss, which is critical for battery-powered applications where maximizing energy efficiency is important.

While switching regulators are efficient, they can introduce noise and ripple into the power supply, which can be detrimental to the performance of sensitive RF and analog circuits. To mitigate this, the 5.5V DC outputs from the L7980A regulators are further converted to the necessary voltages using low-dropout regulators (LDO), specifically the TC1017 series and ADM7170/1 series.

The TC1017 LDOs are used for digital circuitry, the power amplifier's reference voltage input, and the VCO's supply voltage. These LDOs are chosen for their low dropout voltage, low quiescent current, and ability to provide a stable output voltage, which is essential for sensitive digital components [58].

On the other hand, ADM7170 and ADM7171 LDOs are used for all RF device power supplies due to their superior performance in terms of noise and power supply rejection ratio (PSRR). The ADM7170 series can deliver up to 500 mA, while the

ADM7171 series can provide up to 2A, making them ideal for high-current applications such as RF amplifiers and mixers [59]. By using separate ADM7171 regulators for the Tx and Rx 5V supplies, crosstalk and interference between these critical circuits are minimized, enhancing the overall performance and reliability of the radar system.

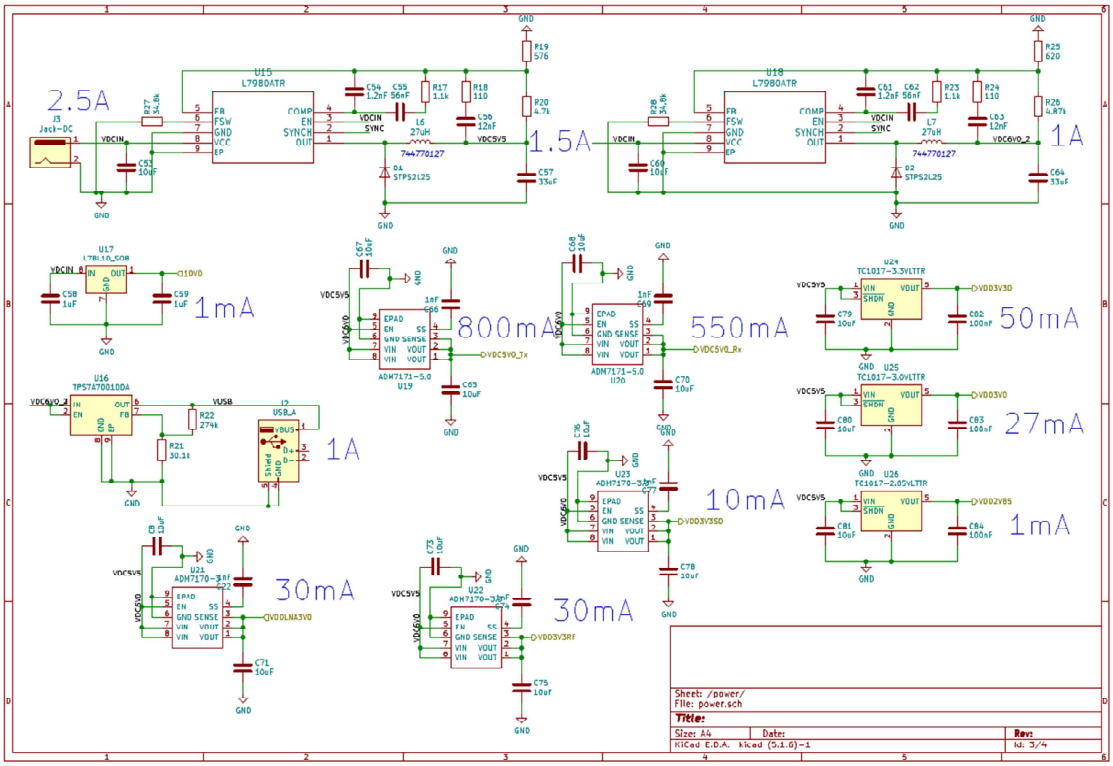


Figure 4.4. Power Section Schematic.

This combination of switching regulators followed by linear regulators allows the system to benefit from both high efficiency and low noise. The switching regulators handle the initial step-down efficiently, while the LDOs ensure a clean, stable power supply for sensitive components, thereby optimizing the overall power management strategy.

In summary, the power design of the FMCW radar system supports the low-noise and stable operation required for UAV deployment by combining efficient switching regulators with low-dropout regulators to balance energy efficiency and noise minimization.

4.3.3. Transmitter Design

The transmitter circuit is a vital part of the radar system, generating the chirp signals necessary for operation. It consists of several key components: the reference clock buffer, the chirp generator, and the power amplifier.

The LVDS CLK input is converted to a CMOS output using the LTC6957-3, which is then used as the reference signal for the PLL. The LTC6957-3 is a very low phase noise, dual-output AC signal buffer/driver/logic level translator. It provides CMOS logic in-phase outputs and is essential for converting the LVDS reference input to a CMOS output suitable for the PLL circuitry [60].

The chirp generator is based on the ADF4158 PLL, which generates the VCO tuning voltage. The ADF4158 is selected for its ability to offer precise frequency control and reduced phase noise, which are critical for achieving high-resolution radar performance [61]. The VCO used is the HMC431, which operates in the 5.5-6.1 GHz range and includes an output buffer. This setup allows for increased frequency ramp linearity and improved performance compared to directly driving a voltage-controlled oscillator.

The SE5004L, a 5 GHz Wi-Fi power amplifier, is used to amplify the chirp signal generated by the VCO. The SE5004L is a highly integrated power amplifier designed for wireless LAN applications. It operates in the 4.9 GHz to 5.9 GHz frequency range and is designed to meet the stringent linearity requirements of IEEE 802.11ac Wi-Fi standards. It features an integrated power detector for closed-loop monitoring of the output power, ensuring stable operation across various conditions. Proper amplification ensures that the generated chirp signal is sufficiently strong before being transmitted through the antenna. The SE5004L also includes on-chip bias circuitry and a power enable pin, which simplifies the design and integration process [62].

The output from the power amplifier is then divided into two using a 15 dB directional coupler. This directional coupler splits the amplified signal to provide a reference signal for the receiver, ensuring synchronized operation between the transmitter and receiver channels.

PLL-based chirp generation offers reduced phase noise and increased frequency ramp linearity, which are essential for achieving high-resolution radar performance. By dividing the output into two using a resistive delta divider, feedback is provided for the loop, ensuring accurate and stable frequency modulation. The power level of the chirp generator is adjusted using a chip attenuator to prevent signal distortion due to the limited dynamic range of the power amplifier.

In addition to the phase noise reduction and frequency ramp linearity, the PLL-based chirp generator allows for precise control over the frequency sweep parameters. This adaptability is crucial for the radar system's flexibility in different operational scenarios, particularly in UAV applications where reliable performance under various environmental conditions and mission requirements is essential.

The overall system diagram for the FMCW radar system, including the transmitter circuit, is shown in Figure 4.5. By integrating these components into the transmitter circuit, the radar system achieves high performance with low phase noise, excellent frequency control, and robust signal amplification. This makes the system well-suited for the demanding requirements of UAV-based radar applications.

To summarize, the transmitter design ensures precise, stable chirp generation and signal amplification, which are essential for achieving high-resolution radar performance under varying UAV operational conditions.

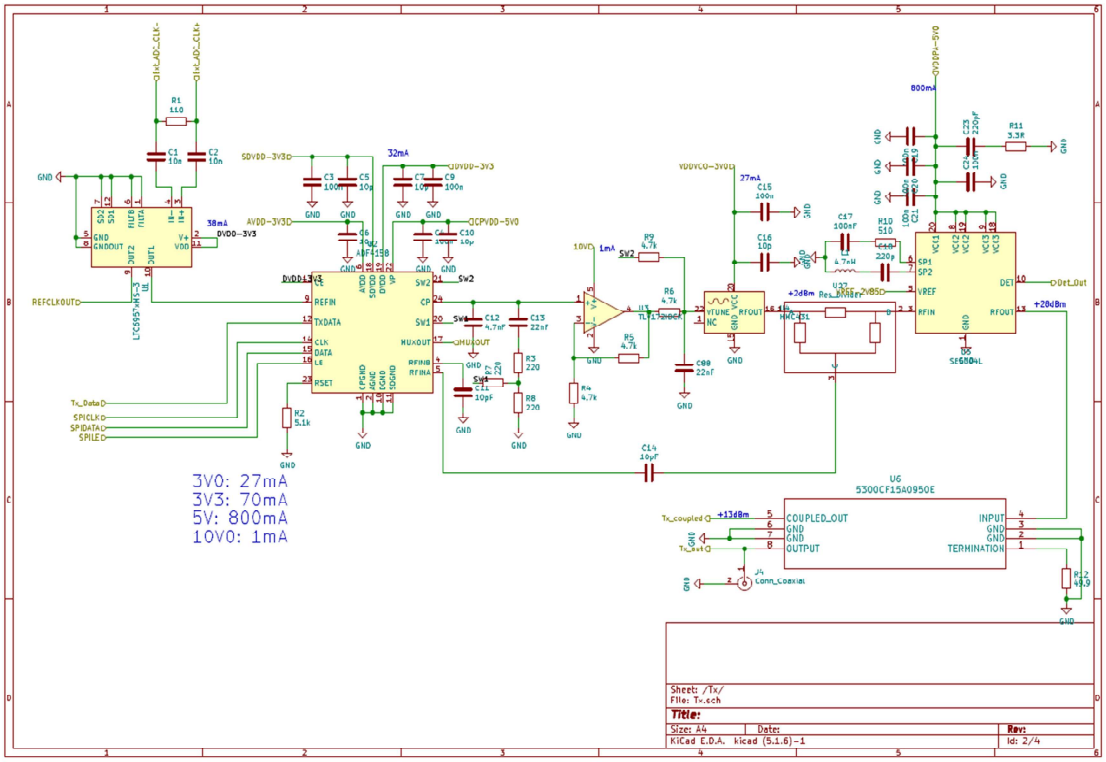


Figure 4.5. Transmitter Schematic.

4.3.4. Receiver Design

The receiver inputs are amplified using an amplifier chain consisting of the SKY65404 and ADL5542. The SKY65404 is a low-noise amplifier designed for wireless applications, providing high gain and a low noise figure, while the ADL5542 is a broadband RF gain block with high linearity. Together, these amplifiers achieve a total gain of 33 dB and a noise figure (NF) of 1.45 dB, ensuring the weak received signals are amplified with minimal noise addition [63, 64].

The unbalanced signals from the amplifiers are converted to balanced signals using a balun, which is critical for differential signal processing to reduce noise and interference. The two receiver channels are then mixed with the transmitted signal to obtain the intermediate frequency (IF) signal using the ADL5802, a high-performance active mixer known for its high linearity and low noise figure [65].

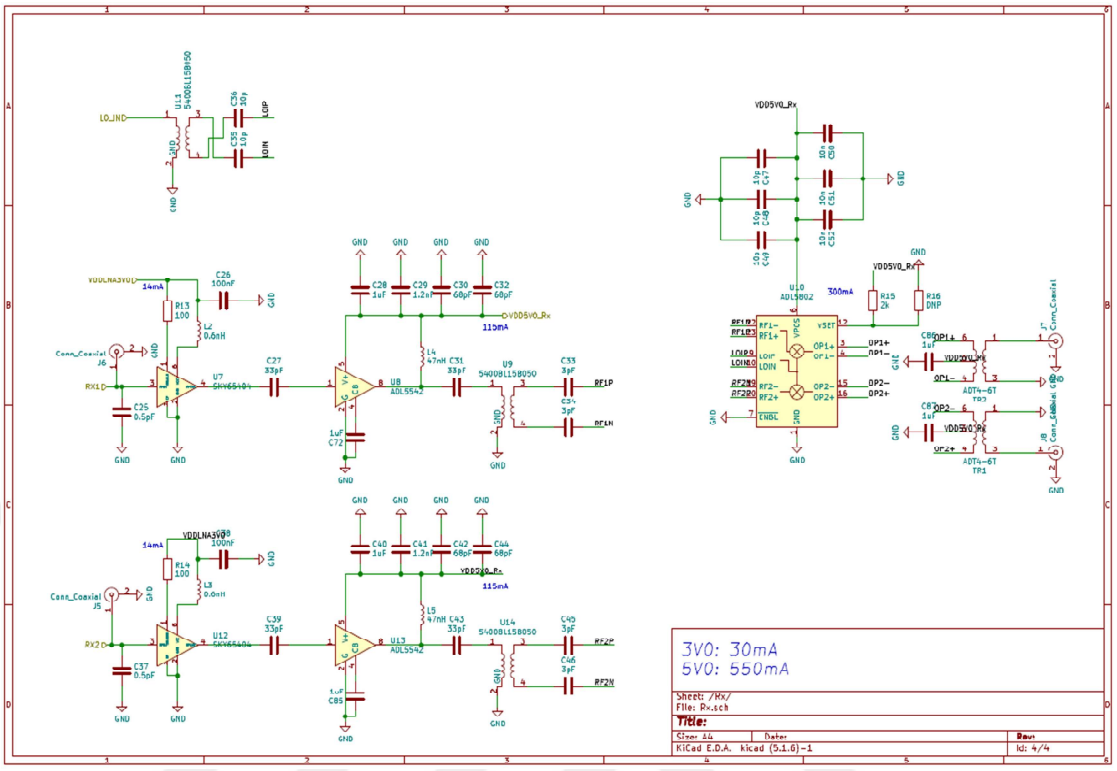


Figure 4.6. Receiver Schematic.

The ADT4-6T balun serves a dual purpose: it biases the mixer output and converts the balanced signal back to an unbalanced signal. Covering a broad frequency range from 0.4 MHz to 6000 MHz, the ADT4-6T provides excellent amplitude and phase balance, essential for precise signal conversion in radar applications [66].

However, a limitation of the ADT4-6T balun is its low cut-off frequency of 60 kHz, which results in a blind range immediately in front of the radar where objects cannot be detected. This limitation is accounted for in the system's operational design and deployment.

The minimum frequency at the output of the receiver will be 60 kHz due to the cut-off frequency of the balun. Given a Pulse Repetition Frequency (PRF) of 10 kHz and a bandwidth of 300 MHz, a target located 1 meter away from the radar will cause an 80 kHz frequency shift at the radar output. This results in a minimum detectable range of approximately 0.75 meters.

The maximum detectable range of the radar is determined by the sampling frequency and the Nyquist rate. At a sampling rate of 5.2 MHz, the maximum detectable range at the Nyquist rate is 65 meters. Increasing the sampling rate to 10.4 MHz extends the maximum detectable range to 130 meters at the Nyquist rate. However, considering practical constraints such as signal processing overhead and system design, the effective maximum detectable range is typically around 100 meters. This balance ensures accurate detection and reliable performance within the specified range.

In summary, the receiver design efficiently amplifies and processes received signals with minimal noise, supporting accurate and reliable detection within the radar's specified range limits, even with blind-range considerations.

4.3.5. Antenna Design and Selection

The radar system utilizes off-the-shelf PCB-based log-periodic antennas for transmission and reception. These antennas, selected to expedite the development process by eliminating the need for custom antenna design, were specified to operate within a bandwidth of 600 MHz to 6 GHz and provide a typical gain of approximately 6 to 7 dBi. With a weight of only 50 grams per unit, they are well-suited for integration into UAV platforms where weight is a critical factor. However, return loss measurements revealed that the antennas maintain a return loss below -10dB across a broader frequency range of 900 MHz to 8.2 GHz, as shown in Figure 4.7. Despite this deviation from the specified range, the antennas effectively cover the operational bandwidth of 5.5 GHz to 5.8 GHz, ensuring reliable performance for the radar system.

Alternative options, such as narrowband antennas, could improve the system's efficiency within the specified frequency range. Patch antennas, for instance, offer focused performance for narrow bandwidths with a typical gain of 7 to 9 dBi while remaining lightweight and compact. Another potential alternative is the planar Yagi–Uda antenna, which provides high gain and directivity. Designing Yagi–Uda antennas involves

complex trade-offs among parameters such as element length, spacing, and diameter, which directly impact gain and input impedance.

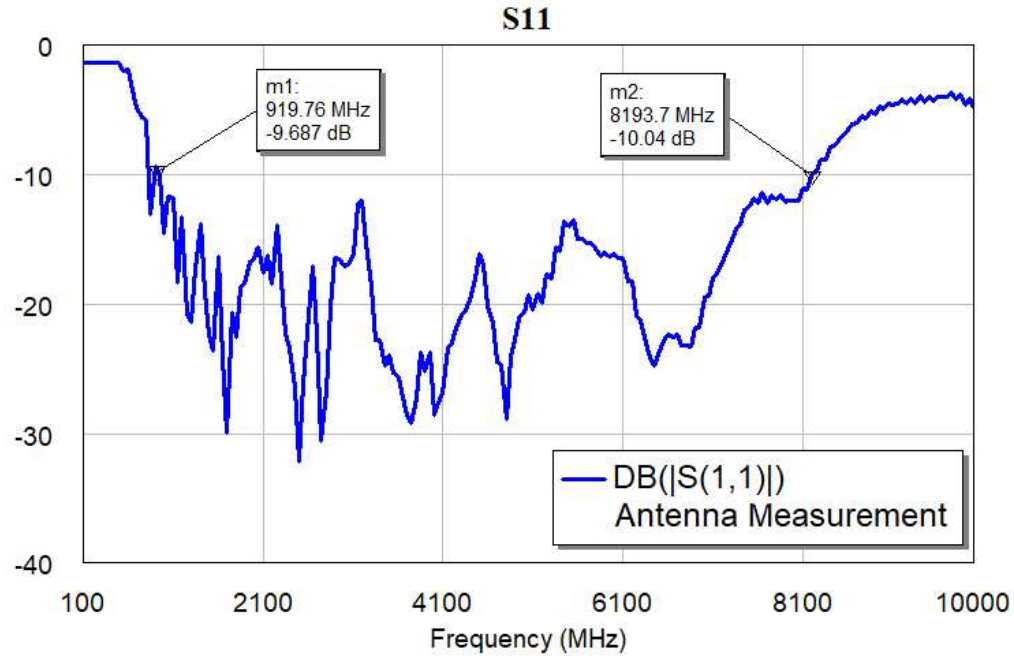


Figure 4.7. Input Matching.

Horn antennas were also evaluated due to their superior gain and directivity. A horn antenna available in the lab, model LB-187-10-C-SFSPO, was reviewed as a candidate. According to its datasheet, this antenna operates between 3.95 GHz and 5.85 GHz, providing a gain of 10 dBi and a Voltage Standing Wave Ratio (VSWR) of less than 1.5:1 across its operational range [67]. Despite its favorable RF performance, its weight of 550 grams exceeds the radar system's payload budget. This example illustrates a broader challenge where commercially available horn antennas, while effective in terms of performance, are generally too heavy for lightweight UAV platforms. Although advanced manufacturing techniques such as 3D printing can be employed to create lightweight horn antennas, these methods are often costly and require specialized fabrication facilities.

4.3.6. Conclusion

The hardware configuration for the FMCW SIMO radar system achieves a balance between range, resolution, and reliability. Optimized components, including low-noise amplifiers, precise PLL-based chirp generation, and efficient power management circuits, address the challenges of compact and high-performance radar systems. The use of PCB log-periodic antennas ensures compliance with bandwidth and gain requirements while meeting UAV payload constraints. Exploring alternative antenna designs, such as narrowband patch antennas or planar Yagi–Uda antennas, provides opportunities for further optimization and demonstrates the design's adaptability.

This robust hardware foundation supports synchronized transmitter and receiver operation, enhancing signal integrity and stability. The integration of antennas highlights their critical role in system-level performance, bridging the gap between electronic design and practical deployment. This hardware design enables the FMCW radar system to deliver accurate, real-time sensing capabilities and supports advanced signal processing and high-resolution imaging applications.

4.4. FMCW Signal Processing Algorithms

The proposed radar system utilizes the backprojection algorithm for high-resolution imaging, which is well-suited for the system's need for parallel processing and fast computation times, as supported by various studies [68–70]. To ensure efficient performance on a lightweight and low-power airborne system, a simplified version of the backprojection algorithm is employed.

The system first performs a Fast Fourier Transform (FFT) on the collected radar data at each observation point to convert the time-domain signals into the frequency domain. Before applying the FFT, the radar data is segmented into individual sweeps, each corresponding to the duration of a single chirp. A Hamming window is applied to each sweep to minimize spectral leakage, preserving the accuracy of the frequency-

domain representation. The FFT size is determined by the sweep length, which is calculated as the product of the sweep duration, equal to $100\,\mu s$, and the sampling rate after decimation, equal to 5.21 MHz. This results in an FFT size of approximately 521 samples per sweep.

This transformation allows for easier analysis and processing of the radar data. Next, the system compensates for residual video phase errors to accurately determine the range profile of the targets. This phase error compensation is crucial for maintaining high image resolution and accurate target detection. This choice of algorithm aligns well with the system's need for real-time or near-real-time processing, which is essential for generating high-resolution SAR images.

The range profiles obtained from the FFT and phase error compensation steps are then used to calculate the reflectivity of each cell within the surveillance area. Reflectivity indicates how much of the radar signal is reflected back from each cell, which is essential for constructing the radar image. However, cells that are beyond the maximum range of the FMCW radar or located outside the antenna beamwidth are not considered in the calculations to optimize processing efficiency and focus on the relevant surveillance area.

The decision-making process for updating the pixel values in the radar image is depicted in Fig 4.8. This flowchart outlines the steps involved in the backprojection algorithm, from data collection and processing to image formation, ensuring a clear understanding of the algorithm's workflow.

The FFT operation in the backprojection algorithm results in a discrete range profile, as it converts the collected radar output into discrete frequencies. This transformation allows the system to analyze the frequency components of the radar signals, which correspond to different ranges. To estimate the range of each point in the observation space more accurately, interpolation is performed based on the two closest

range profile values. This interpolation step enhances the resolution and accuracy of the radar image by refining the discrete data obtained from the FFT.

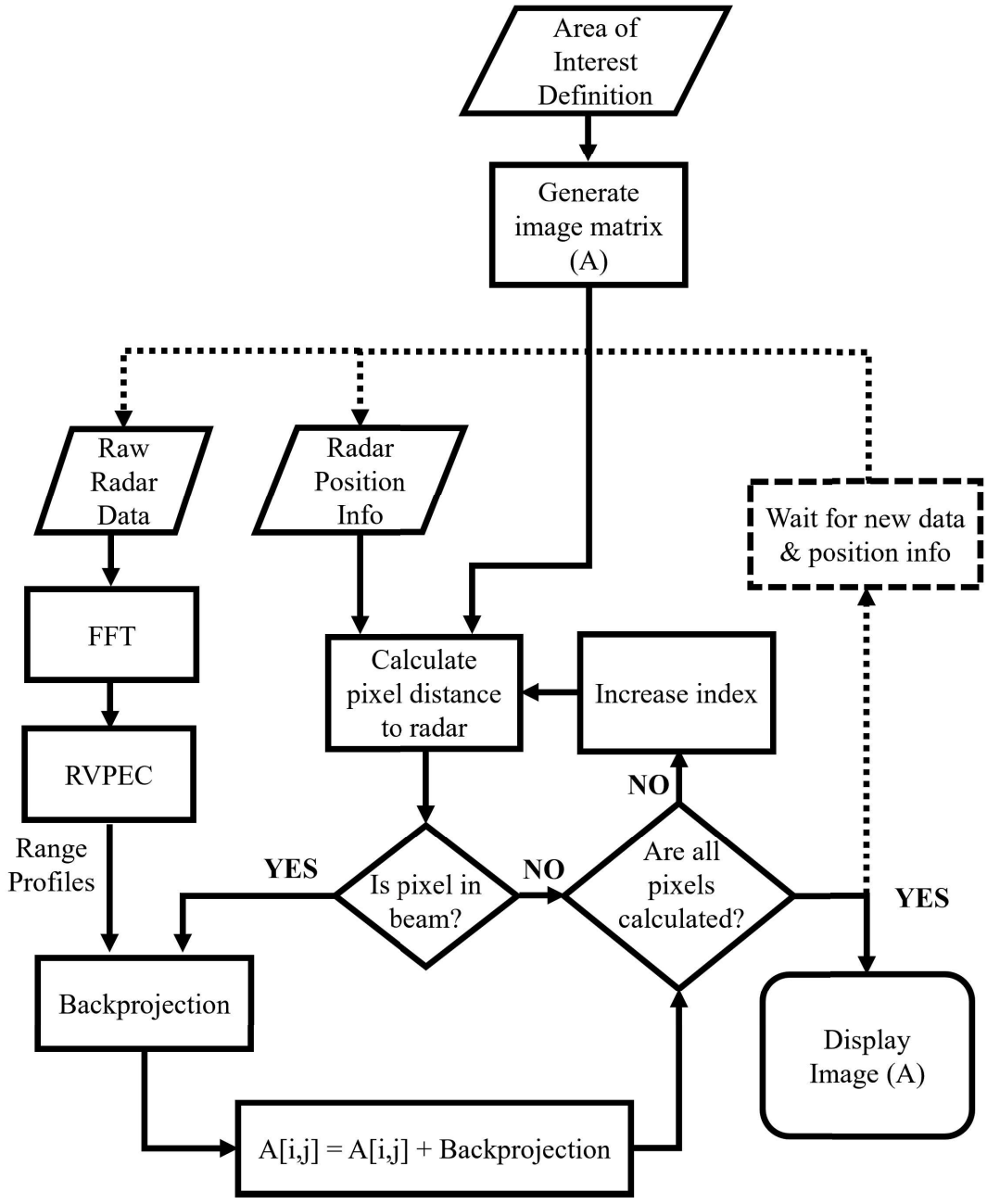


Figure 4.8. Backprojection flowchart.

To calculate the reflectivity of each cell in the observation space, the range profile is multiplied by a phasor $2\pi j(2d/\lambda)$, where d is the distance to the cell and λ is the wavelength of the radar signal. This multiplication compensates for the phase

shift associated with the propagation distance, ensuring that the phase information is correctly accounted for in the reflectivity calculation.

The computation for each cell can be done independently, enabling parallelization for faster processing. This parallel nature of the backprojection algorithm is particularly advantageous for real-time or near-real-time applications, as it allows the system to process large amounts of data efficiently. By collecting multiple snapshots over time, a SAR image can be generated. This SAR image, represented as the A matrix in Fig 4.8, provides detailed and high-resolution imaging capability, crucial for various surveillance and observation applications.

To further improve imaging accuracy and computational efficiency, the algorithm employs advanced interpolation techniques that refine discrete range profiles into continuous estimates. This step, combined with precise phase correction methodologies, ensures the radar's ability to detect subtle variations in reflectivity across the observation space. Moreover, the parallel processing capabilities of the GPU are leveraged to accelerate these computations, enabling near-real-time generation of high-resolution SAR images. This integration of optimized computational methods not only enhances resolution but also ensures the system's adaptability to the constraints of lightweight UAV platforms.

The combination of FFT, interpolation, and phase compensation, along with the parallel processing capability, ensures that the radar system can produce accurate and detailed images quickly. This makes it well-suited for applications requiring rapid and reliable imaging, such as in UAV-based radar systems.

4.5. Conclusion

The proposed radar system integrates a sophisticated hardware design with an efficient backprojection algorithm to achieve high-resolution imaging capabilities. The transmitter circuit, featuring the ADF4158 PLL and the HMC431 VCO, ensures pre-

cise frequency control and robust signal generation. Additionally, the careful selection of components, such as the SE5004L power amplifier and directional coupler, enhances the system's ability to maintain signal integrity and synchronization between the transmitter and receiver channels. This alignment of transmitter and receiver circuitry underscores the system's robust performance capabilities.

The receiver chain, utilizing the SKY65404 and ADL5542 amplifiers, effectively amplifies the received signals while minimizing noise. The use of the ADL5802 mixer and ADT4-6T balun ensures accurate signal conversion and processing. Despite the limitation of a 60 kHz cut-off frequency in the balun, the system achieves a minimum detectable range of 0.75 meters and a practical maximum range of approximately 100 meters, balancing performance and design constraints. These decisions reflect a commitment to achieving a lightweight and power-efficient system, tailored to the payload and operational constraints of consumer UAVs.

The use of PCB log-periodic antennas further supports the system's adaptability, providing a wide operational bandwidth and sufficient gain for UAV applications, while adhering to strict payload constraints. Although alternative antenna designs, such as narrowband patch antennas or planar Yagi–Uda antennas, could enhance efficiency for specific operational frequencies, the current choice balances performance and practical constraints effectively. This integration of antennas highlights their critical role in ensuring system-level functionality and optimizing overall performance.

The implementation of the backprojection algorithm, with FFT processing and phase error compensation, allows for efficient and accurate range profile calculations. The interpolation and parallel processing capabilities enable the generation of SAR images in near-real-time, providing valuable imaging data for surveillance and observation applications. This combination of efficient algorithmic techniques ensures that the system maintains high imaging accuracy while meeting real-time processing demands.

This chapter builds on the author's published work in [55], where the design and performance of this radar system were first detailed. By leveraging advanced hardware design and effective signal processing techniques, the radar system addresses the specific challenges posed by UAV applications. It achieves a lightweight, power-efficient design capable of high-resolution imaging, fast processing times, and reliable performance. This novel combination of compact design and operational efficiency makes it a powerful and practical solution for modern UAV-based radar applications.

5. RESULTS AND DISCUSSION

5.1. Introduction

This section presents a detailed examination of the results and discussion surrounding the development and implementation of an FMCW radar system optimized for UAV-based applications. The primary focus is to provide a thorough analysis of the system's performance, highlighting key aspects such as bandwidth, range resolution, SNR, and power consumption. The realization phase details the assembly of the transceiver board on a 4-layer substrate, emphasizing the benefits of IDC technology for stable connections during flight operations.

The designed system, which includes a radar transceiver, antennas, data acquisition module, and an NVIDIA Jetson Xavier, is subjected to extensive testing both in laboratory settings and real-world scenarios. These tests are designed to assess the radar's capabilities in detecting obstacles, mapping terrain, and generating SAR images. The system's optimization for near-real-time processing is also discussed, showcasing the effectiveness of GPU computing in handling complex radar algorithms. Furthermore, a comparative performance study is conducted to benchmark our system against other state-of-the-art radar technologies used in similar UAV applications. This comparison is based on crucial parameters such as frequency range, power consumption, payload weight, and output power, providing a comprehensive evaluation of the proposed system's efficiency and effectiveness.

5.2. Realization

The transceiver board is assembled on a 4-layer substrate with a total size of 94 mm by 83 mm, as shown in Figure 5.1. IDC technology is used for stable connections, ensuring a secure and durable link that reduces risks of disconnections and signal loss during flight. This simple and efficient connection design also minimizes the likelihood

of damage during assembly and usage, making IDC headers an optimal choice for durability, vibration resistance, and long-term reliability. On-board IDC headers serve multiple purposes, including programming the chirp generator, synchronizing the LVDS clock, and reading power detector values.

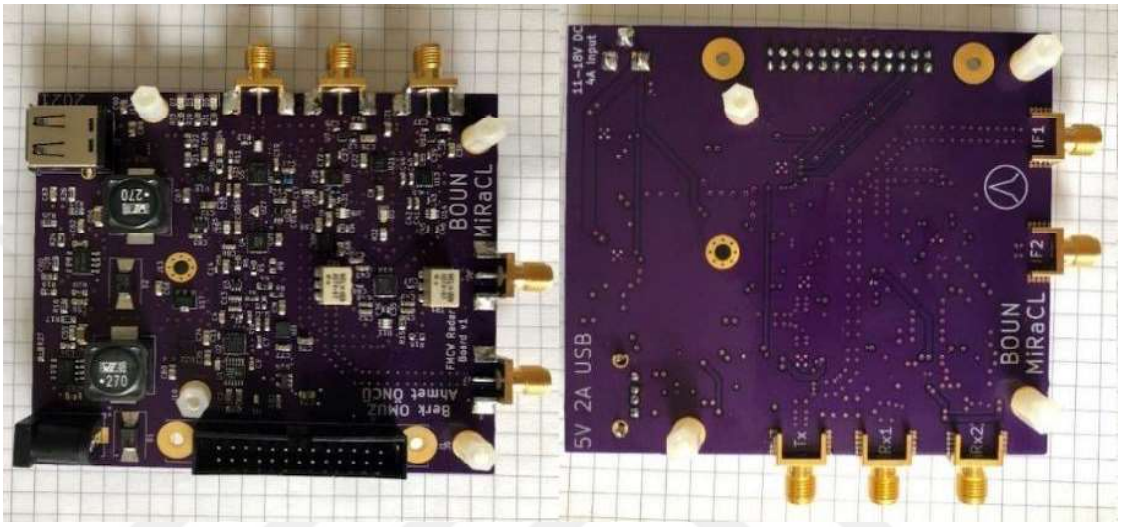


Figure 5.1. FMCW radar board.

The proposed FMCW radar system achieves a bandwidth of 300 MHz, resulting in a range resolution of 50 cm according to Equation (4.11). The maximum range of the radar is primarily constrained by two factors: the sampling frequency and the SNR of the received signal. To optimize data processing and storage requirements, the on-board crystal oscillator generates a 125 MHz clock signal, which can be decimated by 48 in the ADC block, yielding a reduced sampling frequency of 2.6 MSPS. To avoid range limitations, the pulse repetition frequency (PRF) is set to 2 kHz, resulting in a maximum range of 162 meters using Equation (4.8). Assuming a 10 dB SNR at the receiver input, an object with a radar cross-section (RCS) of 1 m^2, and antennas with a 15 dB gain, the maximum range is calculated as 83 meters using Equation (4.9). All design parameters are summarized in Table 5.1. These capabilities make the proposed FMCW radar system suitable for short-range applications such as UAV-based obstacle detection and terrain mapping.

The board's top side features switch-mode voltage regulators, followed by linear regulators that generate the required DC voltages from a 4S to 6S LiPo battery input range. This configuration allows the board to be used on a wide range of UAVs and provides power to other USB-powered devices on the drone. However, high voltage inputs may reduce the efficiency of switch-mode power supplies, potentially increasing the board's overall power consumption. While powered by a 4S battery with a nominal voltage of 14.8 V, the board consumes 9 W, most of which is used by the power amplifier to achieve high output power.

Table 5.1. Board parameters

Parameter	**Value**
Frequency Range	5.5GHz - 5.8GHz
Radar Bandwidth	300MHz
Output Power	+26dBm
PRF	500Hz - 5kHz
Power Consumption of Radar	9W
FMCW Radar Board Size	94mm x 83mm
Total Radar Board Weight	100gr
ADC Sampling Rate	up to 100MHz
ADC # of bits	14

To ensure that the circuitry functions as intended, an FMCW signal with a center frequency of 5.65 GHz and a 300 MHz bandwidth was generated. Power detector readings from the power amplifier were consistent with the expected value, falling within the range of +25 dBm to +26 dBm. The on-board ADC can also monitor the power detector's output DC value, enabling detection of any malfunctions during flight. The transmitter's output spectrum is shown in Figure 5.2.

The complete radar system includes a radar transceiver, antennas, data acquisition module, and an NVIDIA Jetson Xavier. The backprojection algorithm, optimized for NVIDIA Jetson Xavier, was implemented with kernel-level coding to utilize GPU

computing. This optimization allows the system to process radar images in near-real-time, meeting the requirements of a two-channel FMCW SIMO radar system. The algorithm accounts for the individual locations of the transmitter and receiver antennas, providing a more accurate representation of object distances. Although this modification slightly increases computation time, the algorithm still generates up to 100 radar snapshots per second.

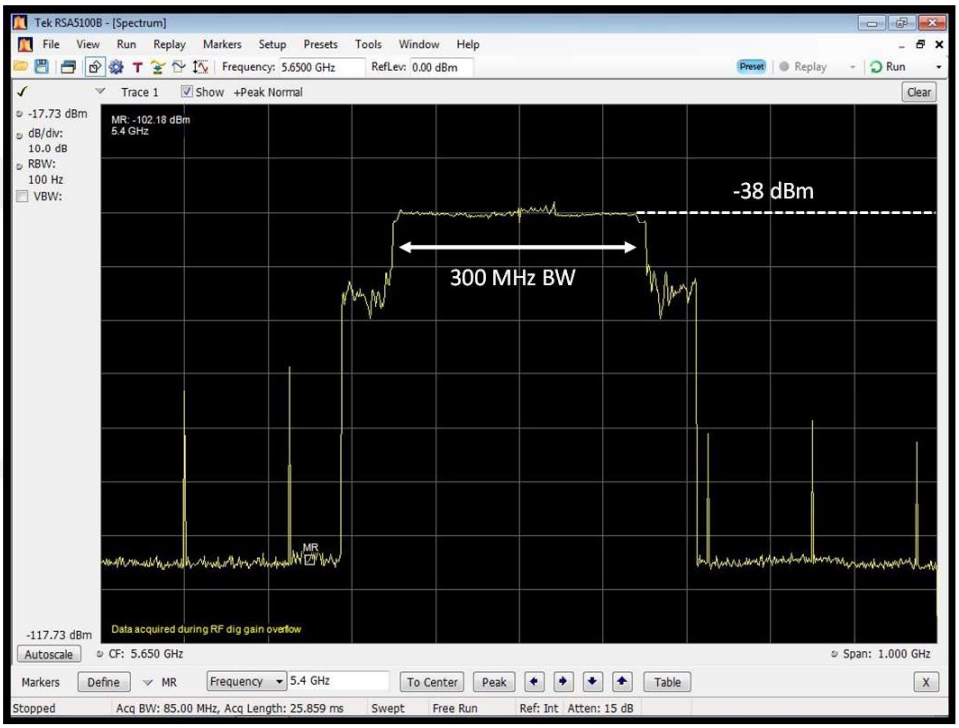


Figure 5.2. Transmitter output spectrum.

Extensive testing was conducted indoors and outdoors over two years across the university campus. These experiments involved diverse conditions, including varying room and ambient temperatures, to gather environmental data. This collected data was crucial for analyzing the system's circuitry performance and served as a foundation for developing signal processing algorithms tailored for near-real-time applications. These comprehensive tests helped refine the radar system and validate its ability to function reliably across different scenarios.

5.3. System Integration

The designed drone system incorporates a mounting space of 25 cm x 25 cm x 20 cm to securely house the radar sensor components. To minimize the overall system weight and facilitate straightforward mounting, log-periodic PCB antennas are used. A two-tier foam structure was carefully cut to support and stabilize the antennas while providing space for the FMCW radar system on the upper tier. The NVIDIA Jetson Xavier is mounted on the top level of the drone to maximize space efficiency and ensure accessibility. To mitigate the effects of vibrations during flight, the drone chassis includes vibration-dampening materials, and the radar system itself is encased in foam to reduce vibrations affecting the antennas.

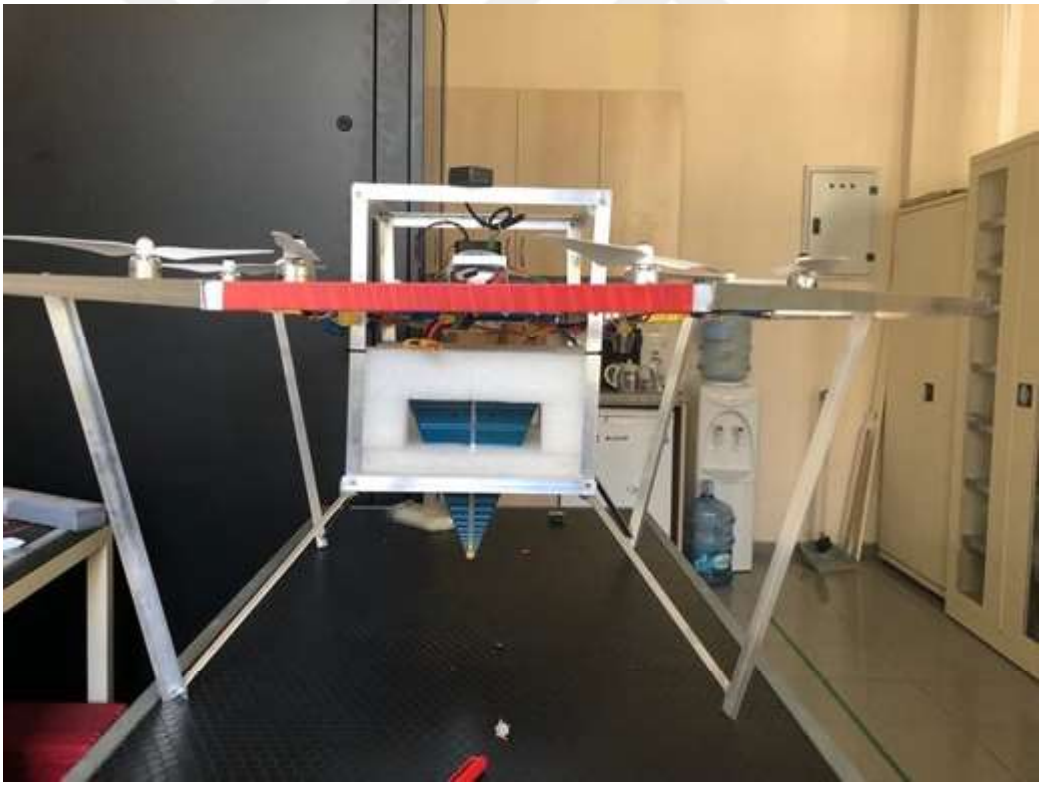


Figure 5.3. The system mounted on a drone.

The entire radar assembly, including the antennas and foam supports, weighs 550 grams and fits snugly into the allocated mounting space, reducing movement and vibration during flight. The radar system's total power consumption is approximately

14 Watts, while the Jetson Xavier weighs 670 grams and has a maximum power draw of 30 Watts.

The system is powered by two separate batteries: one dedicated to the propellers and the other to the sensor systems. This configuration helps balance power loads and maximizes the system's operational efficiency. The estimated flight time with this setup is around four minutes, which is adequate for covering a significant area in a single flight.

5.4. Experiments

A series of experiments were conducted within the university campus to validate the system's detection capabilities at its maximum range and assess its SAR imaging performance in real-world conditions. During these tests, data storage was handled by the NVIDIA Jetson platform, allowing for the collection of raw data to be processed and analyzed afterward.

In one of the range detection experiments, a vehicle was driven toward and then away from the radar system across a distance of approximately 120 meters. The resulting range profile, illustrated in Figure 5.4, captured the radar's capability to detect high-reflectivity objects at significant distances. Objects such as building exteriors were clearly identified at 32 and 49 meters, while pedestrians appeared intermittently between 30 and 70 seconds before moving behind a building. Though the system's calculated maximum range is approximately 83 meters, this experiment demonstrated the radar's capacity to detect objects up to 100 meters, validating its functionality for UAV-based radar imaging.

The range profile analysis confirmed the system's precision in detecting and estimating distances to objects, a crucial feature for UAV applications involving obstacle avoidance and terrain mapping. Accurate range profiling allows for precise spatial awareness, enabling the UAV to navigate complex environments more effectively. This

experiment also highlighted certain limitations, such as difficulties in detecting low-reflectivity objects or objects partially obstructed by other structures. Addressing these challenges may involve adjustments to system parameters or employing advanced signal processing techniques to enhance sensitivity and resolution.

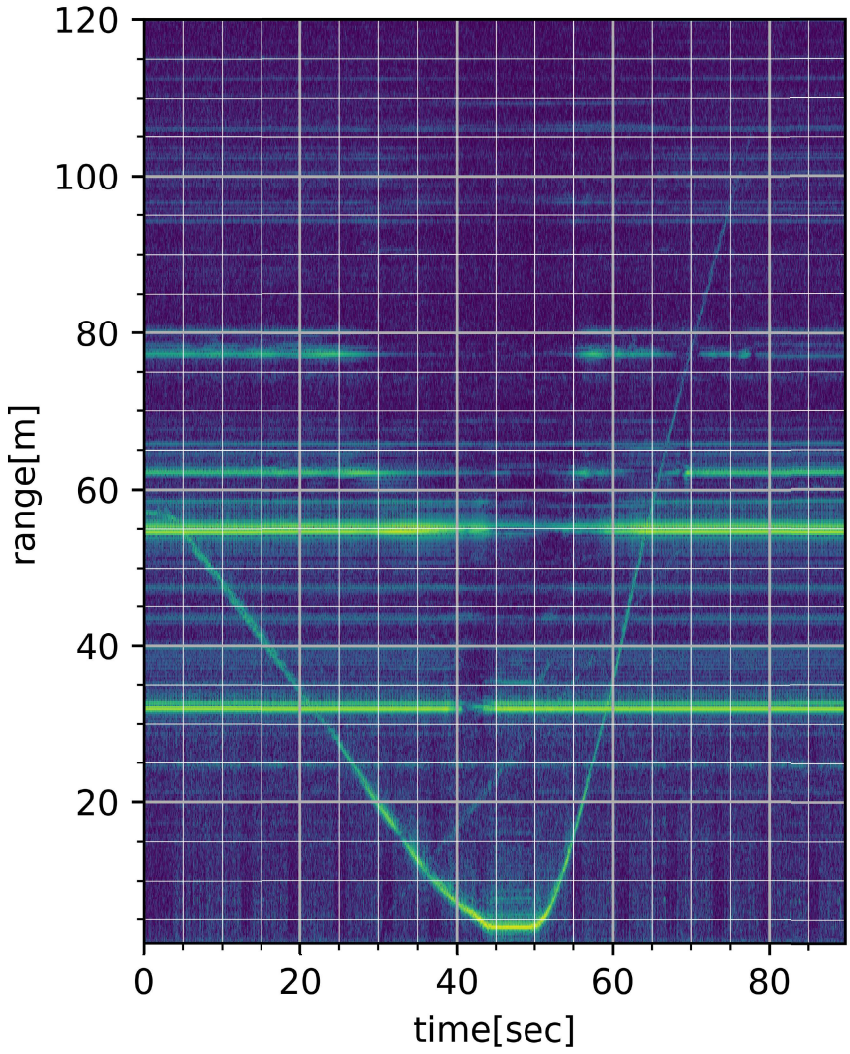


Figure 5.4. Range detection.

Further experiments focused on evaluating the system's SAR imaging capability. During these tests, the radar's transmitter emitted 300 MHz modulated FMCW signals into the target environment, while the receiver collected the reflected signals, converting them into baseband radar data. The radar's baseband processor subsequently processed this data along with the system's positional information to generate SAR images.

To create a synthetic aperture, the system was moved along the y-axis for 31 meters, with data from both receiver channels utilized to enhance image quality. In this configuration, the radar was mounted as a side-looking sensor on the UAV at an elevation angle of zero degrees. The radar was positioned approximately 1.5 meters above ground level, maintaining an average deviation of around 10 centimeters. With a system bandwidth of 300 MHz, the radar achieved a range resolution of 50 cm, allowing for detailed imaging of the environment.

The processed SAR images successfully detected various features within the target area, such as the corners of building exteriors, a security booth, and other high-reflectivity objects. For visualization purposes, the SAR image was overlaid on a Google Earth image, as shown in Figure 5.5. This overlay provided a reference for alignment and scaling, allowing for an intuitive interpretation of the radar's detections within a real-world context. The SAR image achieved an azimuth resolution of 5 cm, with a range pixel separation of 12.5 cm. Additionally, bins corresponding to the radar's blind range of approximately 75 cm were removed from the final image to reduce ambiguity.

To further validate the system's performance, selected distances in the SAR image were measured and compared with actual values. Table 5.2 presents these results, showing good agreement between the measured and actual distances, thereby affirming the system's accuracy in range estimation.

Table 5.2. Prediction error

	Real Value [m]	Measured Value [m]	Percent Error
d1	7.50	7.625	1.66%
d2	4.26	4.00	6.10%
d3	7.10	7.25	2.11%

These experiments demonstrated the radar system's capability to generate high-resolution SAR images, providing valuable data for UAV-based applications in navigation, mapping, and obstacle avoidance. The SAR imaging tests underscored the

radar's potential to deliver reliable environmental awareness data, which is essential for UAV operations in dynamic and challenging settings.

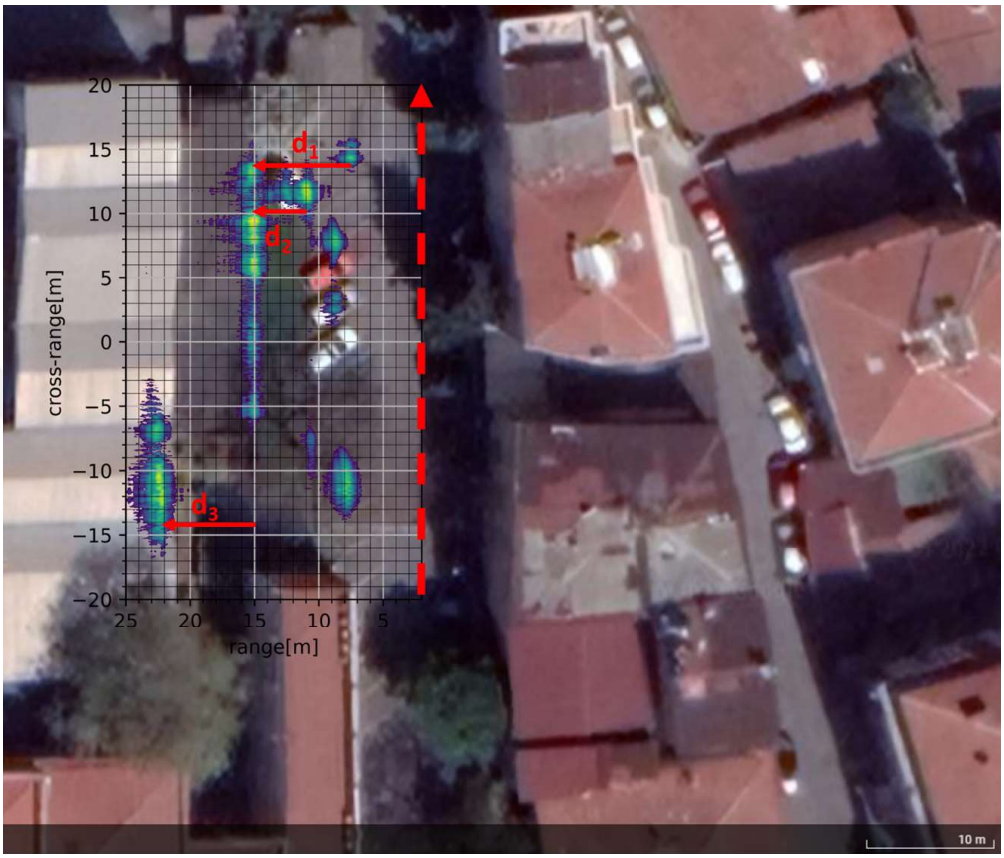


Figure 5.5. KB parking lot measurements compared on top of Google Earth pictures.

5.5. Comparative Performance Study

To comprehensively assess the developed radar system, a comparative analysis was conducted against other state-of-the-art radar systems designed for UAV platforms. Given the variety of methodologies and configurations used in these systems, this comparison focuses on parameters that are especially relevant for UAV-based applications, including frequency range, power consumption, total payload weight, output power, and the number of Tx and Rx channels. Table 5.3 presents these key parameters, along with calculated power efficiency (η) values for each system. Here, power efficiency is defined as the ratio of total RF transmit power to total DC power con-

sumption of the radar, expressed as a percentage. In UAV applications, optimizing power efficiency is critical due to battery limitations.

To further contextualize the comparison, a Figure of Merit (FoM) was introduced to evaluate radar systems for UAV deployment. The FoM, defined as

$$FoM = \frac{\eta}{\text{Total Payload Weight}}, \tag{5.1}$$

considers both power efficiency and payload weight. Minimizing payload weight is critical for improving UAV maneuverability and extending flight duration. By combining these factors, the FoM serves as an effective metric for comparing the suitability of different radar systems.

Table 5.3 highlights the relative performance of each radar system based on key UAV application metrics. Where certain parameters were unavailable, these fields were left blank to maintain accuracy in comparison. Additionally, to contextualize the test environments, a brief overview of the experimental setups and conditions is included for each system.

The radar system in [27] was tested over inhomogeneous soil containing smaller stones and grass, with simulated landmines buried down to 20 cm. [71] conducted tests focusing on GPR abilities, including AT and AP landmines positioned above the ground outdoors. [72] evaluated radar performance across three real-world settings by moving the system over various targets. The radar system in [73] was tested for detecting tripwires of antipersonnel mines through multiple flights, successfully identifying these targets despite random orientations and vegetation cover. [74] employed a fully polarimetric SAR system on a UAV platform, showcasing the system's capabilities across various campaigns at RACBSA airfield and discussing constraints unique to SAR data acquisition on UAVs. Finally, [75] introduced a W-Band 3-D integrated mini-SAR system designed for UAVs, emphasizing high-resolution imaging achieved

through techniques such as LFM wave generation with PLL, W-band motion compensation, and data fusion for signal enhancement.

Table 5.3. Comparative Analysis of UAV-Based Radar Systems

Parameter	Radar Technology	Frequency Range	Power Consumption	Total payload weight (kg)	Output Power (dBm)	# of Tx / Rx	$\eta(\%)$	FoM
This Work	**FMCW**	**5.5GHz - 5.8GHz**	**9W**	**0.5**	**26**	**1/2**	**4.42**	**8.846**
[27]	SFCW	550MHz - 2.7GHz	4.2W	0.78	-4	1/1	0.01	0.012
[71]	FMCW	500MHz - 3GHz	3.5A*	4	24	1/1	0.97	0.242**
[72]	Pulsed Pulson P410	3.2GHz - 5.4GHz	4.2W	0.3	0	1/1	0.0	0.079
[73]	FMCW	1GHz - 4GHz	4.8W	0.2	15	1/1	0.66	3.294
[74]	FMCW	9.6GHz - 9.7GHz	29.3W	2	30	2/2	3.41	1.706
[75]	FMCW	92GHz - 96GHz	25W	0.4	-	1/1	-	-

(*) Power consumption estimated based on current draw.

(**) Assumed 2S battery voltage for FoM calculation.

In comparison, the radar system presented in this work demonstrates a favorable balance between power consumption, weight, and output power, resulting in a high Figure of Merit (FoM) that underscores its suitability for UAV applications. The system's design includes two receiver channels, which enhances spatial resolution over single-input, single-output (SISO) configurations. The dual receiver setup improves

detection robustness by mitigating noise, interference, and multipath effects, while the high output power extends the detection range and provides reliable environmental awareness.

Overall, the comparative analysis validates the developed radar system's strong performance for UAV deployment, with the FoM indicating its competitive efficiency relative to other systems. The combination of high power efficiency, minimal weight, and dual-receiver configuration establishes this radar system as a versatile and robust solution for UAV-based imaging, terrain mapping, and obstacle detection.

5.6. Conclusion

In conclusion, the developed FMCW radar system demonstrates a balanced and effective design that meets the performance requirements for UAV-based applications, such as obstacle detection, terrain mapping, and SAR imaging. With a bandwidth of 300 MHz and an achieved range resolution of 50 cm, the system is optimized for short- to medium-range tasks, making it particularly suitable for UAV environments where both high resolution and rapid data processing are critical. The radar's maximum detection range, calculated under ideal conditions to be approximately 83 meters, further underscores its utility for applications requiring close-proximity monitoring and navigation support.

The integration of the radar system with the NVIDIA Jetson Xavier platform has proven essential for near-real-time image processing, leveraging GPU acceleration to meet the computational demands of SAR imaging and backprojection-based signal processing. This compatibility is especially advantageous in UAV operations where processing speed is crucial for effective real-time decision-making. Experimental results validate the radar's accuracy in identifying high-reflectivity objects and generating detailed SAR images, thereby confirming its applicability in dynamic, obstacle-rich environments that UAVs typically navigate. The system's ability to generate high-

resolution images also supports UAV-based applications in environmental monitoring, providing a robust solution for capturing real-time data.

The comparative analysis with other UAV radar systems further emphasizes the advantages of the proposed design. The radar system's power efficiency, optimized payload weight, and dual-receiver configuration collectively position it as a strong contender in UAV radar applications, as evidenced by its competitive Figure of Merit (FoM). This configuration not only improves spatial resolution but also enhances detection robustness by reducing the impact of noise, interference, and multipath effects, which are common challenges in airborne radar applications. The high output power further extends the radar's detection range, offering a comprehensive solution for UAV-based navigation and mapping.

Looking ahead, future work will focus on further enhancing the radar system's sensitivity and resolution, particularly for low-reflectivity or partially obstructed objects. This could involve refining the signal processing algorithms to increase detection accuracy and efficiency, as well as adjusting system parameters to better accommodate varied environmental conditions. In addition, exploring advanced processing techniques, such as adaptive filtering or machine learning-based feature extraction, may enhance the radar's ability to handle complex scenes and improve target discrimination.

Overall, the proposed FMCW radar system, with its combination of precise hardware design and efficient signal processing, provides a robust and reliable solution for UAV-based applications. The system's adaptability, combined with its efficient power consumption and optimized payload weight, ensures that it can meet the demands of diverse UAV missions, from close-range obstacle detection to high-resolution SAR imaging. As UAV applications continue to expand across sectors, the developed radar system stands as a versatile and powerful tool, ready to support the evolving needs of modern airborne operations.

6. CONCLUSION AND FUTURE WORKS

The development of a low-power, lightweight SIMO SAR radar system specifically designed for UAV platforms represents a significant advancement in UAV radar technology. This research has demonstrated a successful integration of an efficient radar system on small, versatile drones, capable of high-resolution imaging and target detection in diverse environments. The system achieves an optimal balance between power consumption, payload weight, and output power, making it well-suited for applications that require both mobility and operational efficiency.

The research began with an exploration of SFCW radar systems, which offered high SNR and detailed range profiling capabilities. These characteristics make SFCW radar a strong choice for applications requiring fine-grained depth perception, such as GPR. However, the limitations of SFCW radar in achieving real-time data acquisition, especially in dynamic UAV scenarios, highlighted the need for an alternative approach. This challenge informed the transition to FMCW radar, which provided significant advantages in terms of continuous range measurement and mobility, along with faster real-time processing.

A key achievement of this work lies in the effective implementation of an FMCW-based radar system with multiple receiver channels. This configuration enhances spatial resolution, supporting accurate target detection and reducing noise and interference, even in challenging environments. The radar's operational frequency of 5.5 to 5.8 GHz, combined with a bandwidth of 300 MHz, yields a range resolution of 50 cm, making it particularly suitable for detailed obstacle detection and terrain mapping. Moreover, the system's power-efficient design allows for extended UAV flight time, a critical factor for sustained data collection.

A novel contribution of this work is the integration of GPU-based computation for the backprojection algorithm, enabling near-real-time generation of SAR images.

This capability is vital for UAV missions where rapid data processing and feedback are essential. Extensive experimental testing, conducted in both controlled indoor settings and outdoor field conditions, validated the radar system's ability to reliably detect objects at ranges up to 100 meters, reinforcing its potential for practical applications such as UAV navigation and environmental monitoring.

Despite these achievements, several practical challenges and limitations were identified, highlighting areas for potential improvement in future iterations of this system. First, while the radar system performs effectively within its maximum range of 100 meters, detecting objects with low reflectivity or those partially obscured by other surfaces remains challenging. Overcoming this limitation could involve refining the system's signal processing algorithms or increasing the system's sensitivity without compromising power efficiency. Additionally, while the multi-channel receiver setup improves spatial resolution and reduces interference, the complexity of processing data from multiple channels in real time presents a significant challenge, especially for smaller, power-constrained UAV platforms.

The radar system's reliance on a high-power GPU for processing SAR images in real time is another limitation. Although the current setup is feasible for medium-duration UAV missions, future enhancements in power efficiency and computational requirements could further extend operational duration, allowing for longer, more extensive data-gathering missions.

Several opportunities for further research have emerged from this work. Improving the radar system's sensitivity and resolution remains a primary area for enhancement. Techniques such as adaptive filtering could increase its ability to detect low-reflectivity objects or those obscured by environmental clutter. Another avenue involves exploring advanced miniaturization techniques and highly efficient components, which could reduce the radar system's weight and power consumption, supporting longer UAV flight times and more flexible deployment on smaller UAVs.

Additionally, expanding the system's capability to integrate seamlessly with other UAV-based sensor systems, such as LIDAR, hyperspectral cameras, or thermal imaging devices, could unlock new applications in precision agriculture, environmental monitoring, and search-and-rescue operations. Sensor fusion techniques would allow for comprehensive multi-modal data analysis, enhancing the UAV's ability to interpret and respond to complex environments in real time.

In summary, this research presents a practical and effective radar system for UAV-based applications, achieving a robust balance between high-resolution imaging, real-time processing, and power efficiency. By addressing specific design challenges, including lightweight and power-efficient architecture, and implementing innovative processing techniques, this system offers a promising solution for a wide range of UAV applications. Future work will focus on enhancing the system's sensitivity, expanding its multi-sensor capabilities, and conducting extensive real-world field testing to ensure reliability across diverse operational environments. These continued improvements will solidify this radar system's role as a valuable tool for modern UAV platforms, offering improved performance and adaptability for mission-critical applications in various fields.

REFERENCES

1. González-Jorge, H., J. Martínez-Sánchez, M. Bueno and P. Arias, "Unmanned Aerial Systems for Civil Applications: A Review", *Drones*, Vol. 1, No. 1, p. 2, 2017.

2. Chakrabarty, A., R. Morris, X. Bouyssounouse and R. Hunt, "Autonomous Indoor Object Tracking with the Parrot AR. Drone", *International Conference on Unmanned Aircraft Systems (ICUAS)*, pp. 25–30, Arlington, VA, USA, 2016.

3. Stehr, N. J., "Drones: The Newest Technology for Precision Agriculture", *Natural Sciences Education*, Vol. 44, No. 1, pp. 89–91, 2015.

4. Theodorakopoulos, P. and S. Lacroix, "A Strategy for Tracking a Ground Target with a UAV", *IEEE/RSJ International Conference on Intelligent Robots and Systems*, pp. 1254–1259, Nice, France, 2008.

5. Ma'Sum, M. A., M. K. Arrofi, G. Jati, F. Arifin, M. N. Kurniawan, P. Mursanto and W. Jatmiko, "Simulation of Intelligent Unmanned Aerial Vehicle (UAV) for Military Surveillance", *International Conference on Advanced Computer Science and Information Systems (ICACSIS)*, pp. 161–166, Sanur Bali, Indonesia, 2013.

6. Salvo, G., L. Caruso and A. Scordo, "Urban Traffic Analysis through an UAV", *Procedia-Social and Behavioral Sciences*, Vol. 111, pp. 1083–1091, 2014.

7. Ham, Y., K. K. Han, J. J. Lin and M. Golparvar-Fard, "Visual Monitoring of Civil Infrastructure Systems via Camera-Equipped Unmanned Aerial Vehicles (UAVs): A Review of Related Works", *Visualization in Engineering*, Vol. 4, No. 1, pp. 1–8, 2016.

8. Bhardwaj, A., L. Sam, F. J. Martín-Torres and R. Kumar, "UAVs as Remote Sensing Platform in Glaciology: Present Applications and Future Prospects",

Remote Sensing of Environment, Vol. 175, pp. 196–204, 2016.

9. Everaerts, J., "The Use of Unmanned Aerial Vehicles (UAVs) for Remote Sensing and Mapping", *The International Archives of the Photogrammetry, Remote Sensing and Spatial Information Sciences*, Vol. 37, No. 2008, pp. 1187–1192, 2008.

10. Virone, G., A. M. Lingua, M. Piras, A. Cina, F. Perini, J. Monari, F. Paonessa, O. A. Peverini, G. Addamo and R. Tascone, "Antenna Pattern Verification System Based on a Micro Unmanned Aerial Vehicle (UAV)", *IEEE Antennas and Wireless Propagation Letters*, Vol. 13, pp. 169–172, 2014.

11. García-Fernández, M., Y. Á. López, A. Arboleya, B. González-Valdés, Y. Rodríguez-Vaqueiro, M. E. D. C. Gómez and F. L.-H. Andrés, "Antenna Diagnostics and Characterization Using Unmanned Aerial Vehicles", *IEEE Access*, Vol. 5, pp. 23563–23575, 2017.

12. Garcia-Fernandez, M., Y. Alvarez-Lopez and F. Las Heras, "Autonomous Airborne 3D SAR Imaging System for Subsurface Sensing: UWB-GPR On Board a UAV for Landmine and IED Detection", *Remote Sensing*, Vol. 11, No. 20, p. 2357, 2019.

13. Fernández, M. G., Y. Á. López, A. A. Arboleya, B. G. Valdés, Y. R. Vaqueiro, F. L.-H. Andrés and A. P. García, "Synthetic Aperture Radar Imaging System for Landmine Detection Using a Ground Penetrating Radar On Board a Unmanned Aerial Vehicle", *IEEE Access*, Vol. 6, pp. 45100–45112, 2018.

14. García-Fernández, M., Y. Á. López and F. L.-H. Andrés, "Airborne Multi-Channel Ground Penetrating Radar for Improvised Explosive Devices and Landmine Detection", *IEEE Access*, Vol. 8, pp. 165927–165943, 2020.

15. Peng, Z., J. M. Muñoz-Ferreras, Y. Tang, C. Liu, R. Gómez-García, L. Ran and C. Li, "A Portable FMCW Interferometry Radar with Programmable Low-IF

Architecture for Localization, ISAR Imaging, and Vital Sign Tracking", *IEEE Transactions on Microwave Theory and Techniques*, Vol. 65, No. 4, pp. 1334–1344, 2016.

16. Modava, M., G. Akbarizadeh and M. Soroosh, "Hierarchical Coastline Detection in SAR Images Based on Spectral-Textural Features and Global-Local Information", *IET Radar, Sonar & Navigation*, Vol. 13, No. 12, pp. 2183–2195, 2019.

17. Modava, M., G. Akbarizadeh and M. Soroosh, "Integration of Spectral Histogram and Level Set for Coastline Detection in SAR Images", *IEEE Transactions on Aerospace and Electronic Systems*, Vol. 55, No. 2, pp. 810–819, 2019.

18. Mahmoudi Ghara, F., S. B. Shokouhi and G. Akbarizadeh, "A New Technique for Segmentation of the Oil Spills From Synthetic-Aperture Radar Images Using Convolutional Neural Network", *IEEE Journal of Selected Topics in Applied Earth Observations and Remote Sensing*, Vol. 15, pp. 8834–8844, 2022.

19. Wu, X., Z. Zhang, S. Xiong, W. Zhang, J. Tang, Z. Li, B. An and R. Li, "A Near-Real-Time Flood Detection Method Based on Deep Learning and SAR Images", *Remote Sensing*, Vol. 15, No. 8, 2023.

20. an Liu, C., Z. xin Chen, Y. Shao, J. song Chen, T. Hasi and H. zhu Pan, "Research advances of SAR remote sensing for agriculture applications: A review", *Journal of Integrative Agriculture*, Vol. 18, No. 3, pp. 506–525, 2019.

21. Brenner, A. R. and L. Roessing, "Radar Imaging of Urban Areas by Means of Very High-Resolution SAR and Interferometric SAR", *IEEE Transactions on Geoscience and Remote Sensing*, Vol. 46, No. 10, pp. 2971–2982, 2008.

22. Meta, A., P. Hoogeboom and L. P. Ligthart, "Signal Processing for FMCW SAR", *IEEE Transactions on Geoscience and Remote Sensing*, Vol. 45, No. 11, pp. 3519–3532, 2007.

23. Gonzalez-Diaz, M., M. Garcia-Fernandez, Y. Alvarez-Lopez and F. Las-Heras, "Improvement of GPR SAR-based Techniques for Accurate Detection and Imaging of Buried Objects", *IEEE Transactions on Instrumentation and Measurement*, Vol. 69, No. 6, pp. 3126–3138, 2019.

24. Wang, F.-K., T.-S. Horng, K.-C. Peng, J.-K. Jau, J.-Y. Li and C.-C. Chen, "Seeing Through Walls with a Self-Injection-Locked Radar to Detect Hidden People", *IEEE/MTT-S International Microwave Symposium Digest*, pp. 1–3, Montreal, QC, Canada, 2012.

25. Wang, F.-K., T.-S. Horng, K.-C. Peng, J.-K. Jau, J.-Y. Li and C.-C. Chen, "Detection of Concealed Individuals Based on Their Vital Signs by Using a See-Through-Wall Imaging System with a Self-Injection-Locked Radar", *IEEE Transactions on Microwave Theory and Techniques*, Vol. 61, No. 1, pp. 696–704, 2012.

26. Miccinesi, L. and N. Rojhani, "A Doppler Range Compensation for Step-Frequency Continuous-Wave Radar for Detecting Small UAV", *Sensors*, Vol. 19, No. 6, p. 1331, 2019.

27. Sipos, D. and D. Gleich, "A Lightweight and Low-Power UAV-Borne Ground Penetrating Radar Design for Landmine Detection", *Sensors*, Vol. 20, No. 8, 2020.

28. Zhang, Y., D. Orfeo, D. Huston and T. Xia, "Compressive Sensing based Software Defined GPR for Subsurface Imaging", *2021 IEEE Radar Conference (RadarConf21)*, pp. 1–6, Atlanta, Georgia, USA, 2021.

29. Ardzemi, N. H., F. N. M. Isa, N. F. A. Malek, S. Y. Mohamad and R. Nordin, "SFCW Software-Defined Radar using LabVIEW and USRP for Subsurface Sensing", *2022 IEEE International Symposium on Antennas and Propagation and USNC-URSI Radio Science Meeting (AP-S/URSI)*, pp. 1566–1567, Denver, Colorado, USA, 2022.

30. Pham, M. N. and A. F. Jacob, "High-resolution Long Range SFCW-Radar with Multiplicative Array", *2015 German Microwave Conference*, pp. 194–197, Nuremberg, Germany, 2015.

31. Yang, T., A. De Maio, J. Zheng, T. Su, V. Carotenuto and A. Aubry, "An Adaptive Radar Signal Processor for UAVs Detection With Super-Resolution Capabilities", *IEEE Sensors Journal*, Vol. 21, No. 18, pp. 20778–20787, 2021.

32. Zhang, Y., D. Orfeo, D. Huston and T. Xia, "Compressive Sensing based Software Defined GPR for Subsurface Imaging", *2021 IEEE Radar Conference (RadarConf21)*, pp. 1–6, Atlanta, Georgia, USA, 2021.

33. Baspinar, O. O., B. Omuz and A. Oncu, "Detection of the Altitude and On-the-Ground Objects Using 77-GHz FMCW Radar Onboard Small Drones", *Drones*, Vol. 7, No. 2, p. 86, 2023.

34. Science, H. N. and T. C. Ltd., "White paper on NRA24 millimeter wave radar", , 2017, wP002(v2.0)2017-02-28, 2017 [Online]. Available: http://en.nanoradar.cn/File/view/id/435.html.

35. Patole, S. M., M. Torlak, D. Wang and M. Ali, "Automotive Radars: A Review of Signal Processing Techniques", *IEEE Signal Processing Magazine*, Vol. 34, No. 2, pp. 22–35, 2017.

36. Li, H., C. Li, S. Wu, S. Zheng and G. Fang, "Adaptive 3D Imaging for Moving Targets Based on a SIMO InISAR Imaging System in 0.2 THz Band", *Remote Sensing*, Vol. 13, No. 4, 2021.

37. Oshima, A., H. Yamada, Y. Yamaguchi and S. Muramathu, "Fundamental Study on Ambiguity Suppression of Automotive Squint-Mode MW-SAR by Using SIMO Radar", *2018 IEEE International Workshop on Electromagnetics:Applications and Student Innovation Competition (iWEM)*, pp. 1–2, Nagoya, Aichi, Japan,

2018.

38. Feng, F., S. Li, W. Yu and S. Wang, "Study on the Processing Scheme for Space–Time Waveform Encoding SAR System Based on Two-Dimensional Digital Beamforming", *IEEE Transactions on Geoscience and Remote Sensing*, Vol. 50, No. 3, pp. 910–932, 2012.

39. Ji, P., S. Xing, D. Dai, B. Pang and D. Feng, "The Imaging Characteristics of Doppler-Modulation Jamming Against HRWS-SIMO-SAR", *IEEE Geoscience and Remote Sensing Letters*, Vol. 19, pp. 1–5, 2022.

40. Drobotun, N. and P. Mikheev, "A 300khz-13.5ghz Directional Bridge", *2015 European Microwave Conference (EuMC)*, pp. 287–290, Paris, France, 2015.

41. Pozar, D. M., *Microwave engineering; 3rd ed.*, Wiley, Hoboken, NJ, 2005.

42. Hunt, A. R., "Use of a Frequency-Hopping Radar for Imaging and Motion Detection Through Walls", *IEEE Transactions on Geoscience and Remote Sensing*, Vol. 47, No. 5, pp. 1402–1408, 2009.

43. Yigit, E., S. Demirci, C. Ozdemir and A. Kavak, "A Synthetic Aperture Radar-based Focusing Algorithm for B-scan Ground Penetrating Radar Imagery", *Microwave and Optical Technology Letters*, Vol. 49, No. 10, pp. 2534–2540, 2007.

44. Caner Ozdemir, E. Y., Sevket Demirci, "Practical Algorithms to Focus B-Scan GPR Images: Theory and Application to Real Data", *Progress In Electromagnetics Research B*, Vol. 6, pp. 109–122, 2008.

45. Ahmad, F., Y. Zhang and M. G. Amin, "Three-Dimensional Wideband Beamforming for Imaging Through a Single Wall", *IEEE Geoscience and Remote Sensing Letters*, Vol. 5, No. 2, pp. 176–179, 2008.

46. Verma, P. K., A. N. Gaikwad, D. Singh and M. J. Nigam, "Analysis of Clutter

Reduction Techniques for Through-Wall Imaging in UWB Range", *Progress In Electromagnetics Research B*, Vol. 17, pp. 29–48, 2009.

47. Technology, P., *PicoVNA® 100 Series*, 2024, `https://www.picotech.com/download/datasheets/picovna-vector-network-analyzer-data-sheet.pdf`, accessed on October 21, 2023.

48. Omuz, B., F. Oz, O. Ozdemir and A. Oncü, "Experimental Verification of In-door Ground Based SAR Using Beam Space MUSIC Algorithm", *2018 International Conference on Electromagnetics in Advanced Applications (ICEAA)*, pp. 213–216, Cartagena des Indias, Colombia, 2018.

49. Yoon, Y.-S. and M. G. Amin, "High-Resolution Through-the-Wall Radar Imaging Using Beamspace MUSIC", *IEEE Transactions on Antennas and Propagation*, Vol. 56, No. 6, pp. 1763–1774, 2008.

50. Bektas, H. O., O. Ozdemir, M. Orhan and A. S. Turk, "An Experimental Investigation of F-K Migration and SAR Algorithm Using Beam Space MUSIC for UWB Through-the-Wall Imaging", *2016 IEEE Radar Methods and Systems Workshop (RMSW)*, pp. 70–75, Kyiv, Ukraine, 2016.

51. Yoon, Y.-S. and M. G. Amin, "High-Resolution Through-the-Wall Radar Image Based on Beamspace Eigenstructure Subspace Methods", K. I. Ranney and A. W. Doerry (Editors), *Radar Sensor Technology XII*, Vol. 6947, p. 69470C, International Society for Optics and Photonics, SPIE, Orlando, Florida, United States, 2008.

52. Öncü, A., A. Akdoğan and M. Y. Polat, "Remote Sensor Measurement System for Sub-Centimeter Structural Change Detection", *Measurement*, Vol. 228, p. 114350, 2024.

53. Girard, J. M., "Assessing and Monitoring Open Pit Mine Highwalls", *Proceedings*

of the 32nd Annual Institute on Mining Health, Safety and Research, pp. 159–171, Salt Lake City, 2001.

54. Kaartinen, E., K. Dunphy and A. Sadhu, "LiDAR-Based Structural Health Monitoring: Applications in Civil Infrastructure Systems", *Sensors*, Vol. 22, No. 12, 2022.

55. Berk Omuz, H. I. B., Ömer Oğuzhan Baspinar and A. Öncü, "Lightweight High-Output Power C-Band FMCW SIMO Radar System for Small Drones", *International Journal of Remote Sensing*, Vol. 45, No. 13, pp. 4219–4235, 2024.

56. Thurn, K., D. Shmakov, G. Li, S. Max, M.-M. Meinecke and M. Vossiek, "Concept and Implementation of a PLL-Controlled Interlaced Chirp Sequence Radar for Optimized Range–Doppler Measurements", *IEEE Transactions on Microwave Theory and Techniques*, Vol. 64, No. 10, pp. 3280–3289, 2016.

57. STMicroelectronics, *L7980A: Step-Down Switching Regulator*, 2021, `https://www.st.com/resource/en/datasheet/l7980a.pdf`, accessed on January 5, 2022.

58. Microchip Technology, *TC1017: Low Dropout Regulator*, 2021, `https://www.microchip.com/wwwproducts/en/TC1017`, accessed on January 10, 2022.

59. Analog Devices, *ADM7170/ADM7171: Ultralow Noise, High PSRR, RF Linear Regulator*, 2021, `https://www.analog.com/en/products/adm7170.html`, accessed on January 10, 2022.

60. Analog Devices, *LTC6957: Ultralow Phase Noise, Dual Output Buffer/Driver/Logic Level Translator*, 2021, `https://www.analog.com/en/products/ltc6957.html`, accessed on March 11, 2021.

61. Ergintav, A., F. Herzel, G. Fischer and D. Kissinger, "A Study of Phase Noise and Frequency Error of a Fractional-N PLL in the Course of FMCW Chirp Generation", *IEEE Transactions on Circuits and Systems I: Regular Papers*, Vol. 66,

No. 5, pp. 1670–1680, 2019.

62. Skyworks Solutions, Inc., *SE5004L: 5 GHz Wireless LAN Power Amplifier*, 2021, https://www.skyworksinc.com/en/Products/Amplifiers/SE5004L, accessed on January 20, 2022.

63. Skyworks Solutions, Inc., *SKY65404: Low-Noise Amplifier*, 2021, https://www.skyworksinc.com/en/Products/Amplifiers/SKY65404, accessed on February 2, 2022.

64. Analog Devices, *ADL5542: Broadband RF/IF Gain Block*, 2021, https://www.analog.com/en/products/adl5542.html, accessed on February 2, 2022.

65. Analog Devices, *ADL5802: High-Performance Active Mixer*, 2021, https://www.analog.com/en/products/adl5802.html, accessed on February 5, 2022.

66. Mini-Circuits, *ADT4-6T: Broadband RF Transformer*, 2021, https://www.minicircuits.com/WebStore/dashboard.html?model=ADT4-6T, accessed on February 10, 2022.

67. A-Info, *LB-187-10-C-SFSPO Datasheet*, 2024, https://www.ainfoinc.com/techview/product/download/id/1128/sku/LB-187-10-C-SFSPO/, accessed on May 21, 2023.

68. Zaugg, E. C. and D. G. Long, "Generalized Frequency Scaling and Backprojection for LFM-CW SAR Processing", *IEEE Transactions on Geoscience and Remote Sensing*, Vol. 53, No. 7, pp. 3600–3614, 2015.

69. Chang, W., H. Tian and C. Gu, "FMCW SAR: From Design to Realization", *2016 IEEE International Geoscience and Remote Sensing Symposium (IGARSS)*, pp. 1122–1125, Beijing,China, 2016.

70. Desai, M. and W. Jenkins, "Convolution Backprojection Image Reconstruction

for Spotlight Mode Synthetic Aperture Radar", *IEEE Transactions on Image Processing*, Vol. 1, No. 4, pp. 505–517, 1992.

71. Schreiber, E., A. Heinzel, M. Peichl, M. Engel and W. Wiesbeck, "Advanced Buried Object Detection by Multichannel, UAV/Drone Carried Synthetic Aperture Radar", *13th European Conference on Antennas and Propagation (EuCAP)*, pp. 1–5, Krakow, Poland, 2019.

72. Li, C. J. and H. Ling, "High-Resolution, Downward-Looking Radar Imaging Using a Small Consumer Drone", *IEEE International Symposium on Antennas and Propagation (APSURSI)*, pp. 2037–2038, Fajardo, PR, USA, 2016.

73. Schartel, M., R. Burr, W. Mayer and C. Waldschmidt, "Airborne Tripwire Detection Using a Synthetic Aperture Radar", *IEEE Geoscience and Remote Sensing Letters*, Vol. 17, No. 2, pp. 262–266, 2020.

74. Lort, M., A. Aguasca, C. Lopez-Martinez and T. M. Marín, "Initial Evaluation of SAR Capabilities in UAV Multicopter Platforms", *IEEE Journal of Selected Topics in Applied Earth Observations and Remote Sensing*, Vol. 11, No. 1, pp. 127–140, 2017.

75. Ding, M.-L., C.-B. Ding, L. Tang, X.-M. Wang, J.-M. Qu and R. Wu, "A W-band 3-D Integrated Mini-SAR System with High Imaging Resolution on UAV Platform", *IEEE Access*, Vol. 8, pp. 113601–113609, 2020.

76. Gunn, G. E., C. R. Duguay, D. K. Atwood, J. King and P. Toose, "Observing Scattering Mechanisms of Bubbled Freshwater Lake Ice Using Polarimetric RADARSAT-2 (C-Band) and UW-Scat (X-and Ku-Bands)", *IEEE Transactions on Geoscience and Remote Sensing*, Vol. 56, No. 5, pp. 2887–2903, 2018.

77. Wang, H., M. Jiang and S. Zheng, "Airborne Ka FMCW MiSAR System and Real Data Processing", *17th International Radar Symposium (IRS)*, pp. 1–5, Krakow,

Poland, 2016.

78. Ding, M., X. Liang, L. Tang, Z. Wen, X. Wang and Y. Wang, "Micro FMCW SAR with High Resolution for Mini UAV", *International Conference on Microwave and Millimeter Wave Technology (ICMMT)*, pp. 1–3, Chengdu, China, 2018.

79. Yarlequé, M., S. Alvarez and H. Martinez, "FMCW GPR Radar Mounted in a Mini-UAV for Archaeological Applications: First Analytical and Measurement Results", *International Conference on Electromagnetics in Advanced Applications (ICEAA)*, pp. 1646–1648, Verona, Italy, 2017.

80. Patole, S. M., M. Torlak, D. Wang and M. Ali, "Automotive Radars: A Review of Signal Processing Techniques", *IEEE Signal Processing Magazine*, Vol. 34, No. 2, pp. 22–35, 2017.

81. Rao, S., A. Ahmad, J. C. Roh and S. Bharadwaj, "77GHz Single Chip Radar Sensor Enables Automotive Body and Chassis Applications", Texas Instruments, Dallas, TX, 2017.

82. Science, H. N. and T. C. Ltd., "White Paper on CAR28F Millimeter Wave Radar", , 2018, wP021(v1.0)2018-11-12, 2018 [Online]. Available: http://en.nanoradar.cn/File/view/id/442.html.

83. Colorado, J., M. Perez, I. Mondragon, D. Mendez, C. Parra, C. Devia, J. Martinez-Moritz and L. Neira, "An Integrated Aerial System for Landmine Detection: SDR-based Ground Penetrating Radar Onboard an Autonomous Drone", *Advanced Robotics*, Vol. 31, No. 15, pp. 791–808, 2017.

84. Kaniewski, P., C. Leśnik, W. Susek and P. Serafin, "Airborne Radar Terrain Imaging System", *16th International Radar Symposium (IRS)*, pp. 248–253, Dresden, Germany, 2015.

85. Ye, E., G. Shaker and W. Melek, "Lightweight Low-Cost UAV Radar Terrain

Mapping", *13th European Conference on Antennas and Propagation (EuCAP)*, pp. 1–5, Krakow, Poland, 2019.

86. Burr, R., M. Schartel, P. Schmidt, W. Mayer, T. Walter and C. Waldschmidt, "Design and Implementation of a FMCW GPR for UAV-based Mine Detection", *IEEE MTT-S International Conference on Microwaves for Intelligent Mobility (ICMIM)*, pp. 1–4, Munich, Germany, 2018.

87. Svedin, J., A. Bernland, A. Gustafsson, E. Claar and J. Luong, "Small UAV-based SAR System Using Low-Cost Radar, Position, and Attitude Sensors with Onboard Imaging Capability", *International Journal of Microwave and Wireless Technologies*, Vol. 13, No. 6, pp. 602–613, 2021.

88. Suherman, S., R. A. Putra and M. Pinem, "Ultrasonic Sensor Assessment for Obstacle Avoidance in Quadcopter-based Drone System", *3rd International Conference on Mechanical, Electronics, Computer, and Industrial Technology (MECnIT)*, pp. 50–53, Medan, Indonesia, 2020.

89. Li, C. J. and H. Ling, "Synthetic Aperture Radar Imaging Using a Small Consumer Drone", *IEEE International Symposium on Antennas and Propagation & USNC/URSI National Radio Science Meeting*, pp. 685–686, Vancouver, BC, Canada, 2015.

90. Lampersberger, T., R. Feger, A. Haderer, C. Egger, M. Friedl and A. Stelzer, "A 24-GHz Radar with 3D-Printed and Metallized Lightweight Antennas for UAV Applications", *15th European Radar Conference (EuRAD)*, pp. 393–396, Madrid, Spain, 2018.

91. Yan, J., Z. Peng, H. Hong, X. Zhu, Q. Lu, B. Ren and C. Li, "Indoor Range-Direction-Movement SAR for Drone-based Radar Systems", *IEEE Asia Pacific Microwave Conference (APMC)*, pp. 1290–1293, Kuala Lumpar, Malaysia, 2017.

92. Burr, R., M. Schartel, W. Mayer, T. Walter and C. Waldschmidt, "UAV-based Polarimetric Synthetic Aperture Radar for Mine Detection", *IGARSS IEEE International Geoscience and Remote Sensing Symposium*, pp. 9208–9211, Yokohama, Japan, 2019.

93. Dong, J., K. Ota and M. Dong, "UAV-based Real-Time Survivor Detection System in Post-Disaster Search and Rescue Operations", *IEEE Journal on Miniaturization for Air and Space Systems*, Vol. 2, No. 4, pp. 209–219, 2021.

94. Georgiev, G. D., G. Hristov, P. Zahariev and D. Kinaneva, "Forest Monitoring System for Early Fire Detection Based on Convolutional Neural Network and UAV imagery", *28th National Conference with International Participation (TELECOM)*, pp. 57–60, Sofia, Bulgaria, 2020.

95. "IWR1843 Single-Chip 76- to 81-GHz FMCW mmWave Sensor Datasheet (Rev. A)", Texas Instruments, Dallas, TX, 2022.

96. "AWR1843BOOST and IWR1843BOOST Single-Chip mmWave Sensing Solution User's Guide (Rev. B)", Texas Instruments, Dallas, TX, 2020.

97. Ramasubramanian, K., "Using a Complex-Baseband Architecture in FMCW Radar Systems", Texas Instruments, Dallas, TX, 2017.

98. Xiong, J., H. Hong, L. Xiao, E. Wang and X. Zhu, "Vital Signs Detection With Difference Beamforming and Orthogonal Projection Filter Based on SIMO-FMCW Radar", *IEEE Transactions on Microwave Theory and Techniques*, Vol. 71, No. 1, pp. 83–92, 2023.

99. Hilario Re, P. D., D. Comite, S. K. Podilchak, C. A. Alistarh, G. Goussetis, M. Sellathurai, J. Thompson and J. Lee, "FMCW Radar With Enhanced Resolution and Processing Time by Beam Switching", *IEEE Open Journal of Antennas and Propagation*, Vol. 2, pp. 882–896, 2021.

100. Analog Devices, *ADF4158: 6.1 GHz, Fractional-N Frequency Synthesizer with Direct Modulation and Waveform Generation Capability*, 2021, `https://www.analog.com/en/products/adf4158.html`, accessed on January 5, 2022.

101. Analog Devices, *HMC431: Voltage Controlled Oscillator*, 2021, `https://www.analog.com/en/products/hmc431.html`, accessed on January 5, 2022.

102. Skyworks Solutions, Inc., *SE5004L Evaluation Board Datasheet*, 2010, `https://www.cdiweb.com/datasheets/skyworks/se5004l-ek1_202643a.pdf`, accessed on February 15, 2022.

103. Akhilendra Pratap Singh, P. K. J., Smrity Dwivedi, "Analysis of the Imaging Algorithms for Shape Detection and Shape Identification of a Target Using Through-the-Wall Imaging System", *Progress In Electromagnetics Research B*, Vol. 85, pp. 181–199, 2019.

104. Marandi, S. M., K. Rahmani and M. Tajdari, "Foreign Object Damage on the Leading Edge of Gas Turbine Blades", *Aerospace Science and Technology*, Vol. 33, pp. 65–75, 2014.

105. Wang, X., Z. Lan, Z. Li, Y. Lin and Q. Xiao, "A Practical Application of Runway Foreign Object Debris Detection System at the Airport", *2018 International Conference on Microwave and Millimeter Wave Technology (ICMMT)*, pp. 1–3, Chengdu, China, 2018.

106. Chauhan, T., C. Goyal, D. Kumari and A. K. Thakur, "A Review on Foreign Object Debris/Damage (FOD) and Its Effects on the Aviation Industry", *Materials Today: Proceedings*, Vol. 33, pp. 4336–4339, 2020.

107. Zhang, L., C. Long, J. Tong and P. Yang, "Research on FOD Monitoring Radar Imaging Based on Arc Synthetic Aperture System", *2020 IEEE 2nd International Conference on Civil Aviation Safety and Information Technology (ICCASIT)*, pp.

1072–1076, Weihai, China, 2020.

108. Feil, P., W. Menzel, T. Nguyen, C. Pichot and C. Migliaccio, "Foreign Objects Debris Detection (FOD) on Airport Runways Using a Broadband 78 GHz Sensor", *2008 38th European Microwave Conference*, pp. 1608–1611, Amsterdam, The Netherlands, 2008.

109. Dabbiru, L., P. Wei, A. Harsh, J. White, J. E. Ball, J. Aanstoos, P. Donohoe, J. Doyle, S. Jackson and J. Newman, "Runway Sssessment via Remote Sensing", *2015 IEEE Applied Imagery Pattern Recognition Workshop (AIPR)*, pp. 1–4, Washington, DC, USA, 2015.

110. Elrayes, A., M. Ali, A. Zakaria and M. Ismail, "Smart Airport Foreign Object Debris Detection Rover using LiDAR Technology", *Internet of Things*, Vol. 5, pp. 1–11, 2018.

111. Anders, N. S., A. C. Seijmonsbergen and W. Bouten, "Geomorphological Change Detection Using Object-Based Feature Extraction From Multi-Temporal LiDAR Data", *IEEE Geoscience and Remote Sensing Letters*, Vol. 10, No. 6, pp. 1587–1591, 2013.

112. Minh Mai, N. A., P. Duthon, P. H. Salmane, L. Khoudour, A. Crouzil and S. A. Velastin, "Camera and LiDAR Analysis for 3D Object Detection in Foggy Weather Conditions", *2022 12th International Conference on Pattern Recognition Systems (ICPRS)*, pp. 1–7, Saint-Etienne, France, 2022.

113. Kutila, M., P. Pyykönen, H. Holzhüter, M. Colomb and P. Duthon, "Automotive LiDAR Performance Verification in Fog and Rain", *2018 21st International Conference on Intelligent Transportation Systems (ITSC)*, pp. 1695–1701, Maui, Hawaii, USA, 2018.

114. Sun, W., Y. Hu, D. G. MacDonnell, C. Weimer and R. R. Baize, "Technique to

Separate Lidar Signal and Sunlight", *Opt. Express*, Vol. 24, No. 12, pp. 12949–12954, 2016.

115. Moreira, A., P. Prats-Iraola, M. Younis, G. Krieger, I. Hajnsek and K. P. Papathanassiou, "A Tutorial on Synthetic Aperture Radar", *IEEE Geoscience and Remote Sensing Magazine*, Vol. 1, No. 1, pp. 6–43, 2013.

116. Motohka, T., Y. Kankaku and S. Suzuki, "Advanced Land Observing Satellite-2 (ALOS-2) and Its Follow-On L-Band SAR Mission", *2017 IEEE Radar Conference (RadarConf)*, pp. 0953–0956, Seattle, WA, USA, 2017.

117. Liu, D., Y. Shao, Z. Liu, B. Riedel, A. Sowter, W. Niemeier and Z. Bian, "Evaluation of InSAR and TomoSAR for Monitoring Deformations Caused by Mining in a Mountainous Area with High Resolution Satellite-Based SAR", *Remote Sensing*, Vol. 6, No. 2, pp. 1476–1495, 2014.

118. Fujiwara, S., H. Yarai, T. Kobayashi, Y. Morishita, T. Nakano, B. Miyahara, H. Nakai, Y. Miura, H. Ueshiba, Y. Kakiage and H. Une, "Small-Displacement Linear Surface Ruptures of the 2016 Kumamoto Earthquake Sequence Detected by ALOS-2 SAR Interferometry", *Earth, Planets and Space*, Vol. 68, No. 1, p. 160, 2016.

119. Heinzel, A., M. Schartel, R. Burr, R. Bähnemann, E. Schreiber, M. Peichl and C. Waldschmidt, "A Comparison of Ground-Based and Airborne SAR Systems for the Detection of Landmines, UXO, and IEDs", K. I. Ranney and A. Doerry (Editors), *Radar Sensor Technology XXIII*, Vol. 11003, p. 1100304, International Society for Optics and Photonics, SPIE, Baltimore, Maryland, USA, 2019.

120. Leva, D., G. Nico, D. Tarchi, J. Fortuny-Guasch and A. Sieber, "Temporal Analysis of a Landslide by Means of a Ground-Based SAR Interferometer", *IEEE Transactions on Geoscience and Remote Sensing*, Vol. 41, No. 4, pp. 745–752, 2003.

121. Luzi, G., L. Noferini, D. Mecatti, G. Macaluso, M. Pieraccini, C. Atzeni, A. Schaffhauser, R. Fromm and T. Nagler, "Using a Ground-Based SAR Interferometer and a Terrestrial Laser Scanner to Monitor a Snow-Covered Slope: Results From an Experimental Data Collection in Tyrol (Austria)", *IEEE Transactions on Geoscience and Remote Sensing*, Vol. 47, No. 2, pp. 382–393, 2009.

122. Serrano-Juan, A., E. Vázquez-Suñè, O. Monserrat, M. Crosetto, C. Hoffmann, A. Ledesma, R. Criollo, E. Pujades, V. Velasco, A. Garcia-Gil and M. Alcaraz, "GB-SAR Interferometry Displacement Measurements During Dewatering in Construction Works: Case of La Sagrera Railway Station in Barcelona, Spain", *Engineering Geology*, Vol. 205, pp. 104–115, 2016.

123. Bamler, R. and P. Hartl, "Synthetic Aperture Radar Interferometry", *Inverse Problems*, Vol. 14, No. 4, p. R1, 1998.

124. Pieraccini, M. and L. Miccinesi, "Ground-Based Radar Interferometry: A Bibliographic Review", *Remote Sensing*, Vol. 11, No. 9, 2019.

125. Wang, P., C. Xing, X. Pan, X. Zhou and B. Shi, "Microdeformation Monitoring by Permanent Scatterer GB-SAR Interferometry Based on Image Subset Series with Short Temporal Baselines: The Geheyan Dam Case Study", *Measurement*, Vol. 184, p. 109944, 2021.

126. Wang, R., T. Zhang, X. Liu, Z. Lu and T. Guo, "Distance-Restrained Atmospheric Parameters Correction (DR-APC) Model for GB-SAR Transmission Power Attenuation Compensation in Bridge Dynamic Deflection Measurement", *Measurement*, Vol. 205, p. 112192, 2022.

127. He, Z., W. Li, H. Salehi, H. Zhang, H. Zhou and P. Jiao, "Integrated Structural Health Monitoring in Bridge Engineering", *Automation in Construction*, Vol. 136, p. 104168, 2022.

128. Brownjohn, J. M. W., "Structural Health Monitoring of Civil Infrastructure", *Philosophical Transactions of the Royal Society A: Mathematical, Physical and Engineering Sciences*, Vol. 365, No. 1851, pp. 589–622, 2007.